



**UNIVERSITY OF LEEDS**

# Control of Magnetic Continuum Robots for Endoscopy

Giovanni Pittiglio

Submitted in accordance with the requirements for the  
degree of Doctorate of Philosophy in Robotics

The University of Leeds  
Faculty of Engineering  
School of Electronic and Electrical Engineering

February 2022

# Abstract

---

The present thesis discusses the problem of magnetic actuation and control applied to millimetre-scale robots for endoluminal procedures. Magnetic actuation, given its remote manipulation capabilities, has the potential to overcome several limitations of current endoluminal procedures, such as the relatively large size, high stiffness and limited dexterity of existing tools. The application of functional forces remotely facilitates the development of softer and more dexterous endoscopes, which can navigate with reduced discomfort for the patient. However, the solutions presented in literature are not always able to guarantee smooth navigation in complex and convoluted anatomical structures. This thesis aims at improving the navigational capabilities of magnetic endoluminal robots, towards achieving full autonomy. This is realized by introducing novel design, sensing and control approaches for magnetically actuated soft endoscopes and catheters.

First, the application of accurate closed-loop control to a 1 Internal Permanent Magnet (IPM) endoscope was analysed. The proposed approach can guarantee better navigation capabilities, thanks to the manipulation of every mechanical Degree of Freedom (DOF) - 5 DOFs. Specifically, it was demonstrated that gravity can be balanced with sufficient accuracy to guarantee tip levitation. In this way contact is minimized and obstacle avoidance improved. Consequently, the overall navigation capabilities of the endoscope were enhanced for given application.

To improve exploration of convoluted anatomical pathways, the design of magnetic endoscopes with multiple magnetic elements along their length was introduced. This approach to endoluminal device design can ideally allow manipulation along the full length; facilitating full shape manipulation, as compared to tip-only control. To facilitate the control of multiple magneto-mechanical DOFs along the catheters' length, a magnetic actuation method was developed based on the collaborative robotic manipulation of 2 External Permanent Magnets (EPMs). This method, compared to the state-of-the-art, facilitates large workspace and applied field, while guaranteeing dexterous actuation. Using this approach, it was demonstrated that it is possible to actuate up to 8 independent magnetic DOFs.

---

In the present thesis, two different applications are discussed and evaluated, namely: colonoscopy and navigational bronchoscopy. In the former, a single-IPM endoscopic approach is utilized. In this case, the anatomy is large enough to permit equipping the endoscope with a camera; allowing navigation by direct vision. Navigational bronchoscopy, on-the-other-hand, is performed in very narrow peripheral lumina, and navigation is informed via pre-operative imaging. The presented work demonstrates how the design of the magnetic catheters, informed by a pre-operative Computed Tomography (CT) scan, can mitigate the need for intra-operative imaging and, consequently, reduce radiation exposure for patients and healthcare workers. Specifically, an optimization routine to design the catheters is presented, with the aim of achieving follow-the-leader navigation without supervision.

In both scenarios, analysis of how magnetic endoluminal devices can improve the current practice and revolutionize the future of medical diagnostics and treatment is presented and discussed.



# Acknowledgments

---

I would like to thank Pietro Valdastri for his guidance during my PhD years. His example of dedication has had the greatest impact on my achievements. He has been a devoted mentor and taught me to be a better researcher.

To Simone Calò goes my greatest gratitude for being a supportive friend for all these years.

My thank goes to James Chandler. He has been an example of strength and a supportive mentor.

To my parents for always believing in me and supporting my life and career choices. To my sister for being present unconditionally. To my all family a big thanks.

To Zaneta Koszowska for believing in me also when I was too tired to believe in myself. I wish everyone to have so much care in the moment of need.

To Tomas Da Veiga for being a great colleague and friend.

To Michael Brockdorff for his ability of making me smile in the worst possible moments.

To Pete Lloyd for all we accomplished together and the great time I had working with him.

To Lavinia Barducci for being there listening to my complaints and somehow making me smile about it.

To Claire Alcock for being the best friend one can wish for.

To James Martin for welcoming me to the lab and teaching me more than I can thank him for.

To Nils Marahrens for all the great moments we had playing jazz together.

To the students I had the honour to advice in their master projects, David Biegger, Michiel Richter and Margherita Rustia.

To every member of the STORM Lab for all I learned from each of them, inside and outside the lab.

# Contents

<b>1</b>	<b>Introduction and Contributions</b>	<b>1</b>
1.1	Single IPM Actuation . . . . .	4
1.2	Multi-IPM Devices for Navigational Dexterity . . . . .	7
1.3	Dexterous Magnetic Actuation . . . . .	9
<b>2</b>	<b>Single Magnet Control</b>	<b>19</b>
2.1	Introduction . . . . .	21
2.2	Method . . . . .	23
2.3	Dynamic Control . . . . .	24
2.3.1	Pose Control . . . . .	27
2.3.2	Force Control . . . . .	28
2.3.3	Overall Control . . . . .	29
2.4	Experimental Analysis: Free Space Levitation . . . . .	30
2.5	Experimental Analysis: Colon Phantom . . . . .	32
2.6	Conclusions . . . . .	34
	<b>Appendices</b>	<b>35</b>
<b>3</b>	<b>Collaborative Magnetic Manipulation</b>	<b>45</b>
3.1	Introduction . . . . .	46
3.2	Problem Definition . . . . .	49
3.3	Definition of Magnetic Manipulability . . . . .	51
3.4	Degrees of Freedom Analysis . . . . .	54

3.5	Experimental Analysis . . . . .	56
3.6	Conclusions . . . . .	60
<b>4</b>	<b>Optimal Design for Magnetic Continuum Robots</b>	<b>65</b>
4.1	Introduction . . . . .	67
4.2	Materials and Methods . . . . .	70
4.2.1	Rigid-link Modelling and Design Optimization . . . . .	70
4.2.2	Catheter Fabrication . . . . .	72
4.2.3	Dual Arm Magnetic Manipulation . . . . .	73
4.2.4	2D Experiments . . . . .	77
4.2.5	Anatomical Phantom Experiments . . . . .	79
4.3	Results . . . . .	80
4.3.1	2D Obstacle Avoidance . . . . .	80
4.3.2	2D Navigation . . . . .	82
4.3.3	Anatomical Phantom Experiments . . . . .	87
4.4	Discussions . . . . .	88
4.5	Conclusions . . . . .	89
<b>5</b>	<b>Attitude Sensing within Strong Magnetic Field</b>	<b>95</b>
5.1	Introduction . . . . .	96
5.2	Preliminaries . . . . .	98
5.2.1	Problem Formulation . . . . .	99
5.2.2	Riemannian Geometry . . . . .	100
5.3	Observability Analysis . . . . .	103
5.3.1	First-order Observability Analysis . . . . .	105
5.3.2	Second-order Observability Analysis . . . . .	106
5.4	Observer Design . . . . .	108
5.5	Discrete EKF on $SO(3)$ . . . . .	109
5.6	Numerical Results . . . . .	111
5.7	Experimental Analysis . . . . .	114

---

5.8 Conclusions . . . . .	117
<b>6 Conclusions</b>	<b>121</b>



# List of Figures

1.1	Schematic representation of the Magnetic Flexible Endoscope (MFE). . .	4
1.2	Schematic representation of and endoluminal lung procedure performed with magnetic tentacle. . . . .	8
1.3	Schematic representation of the dual External Permanent Magnet (dEPM) platform. . . . .	10
2.1	Schematic representation of the platform. . . . .	21
2.2	Control scheme. . . . .	26
2.3	3D tracking. The IPM (solid line) and EPM (dashed line) trajectories for all trials performed. . . . .	30
2.5	Experimental setup: colon simulator. . . . .	33
2.6	Trials on the colon simulator. . . . .	33
3.1	Example of application of multi-DOFs magnetic manipulation in endoscopy: bronchoscopy. . . . .	47
3.2	EPMs poses for independent DOFs control; cases are shown with EPM-IPM center to center distance of 0.25 m. . . . .	51
3.3	Example of orthogonal IPMs and directions of the wrench applied for each of the cases of Fig. 3.2. . . . .	52
3.4	Experimental Setup. . . . .	57
3.5	Normalized response for magnetic field and differentials. Title colors are referred to the component activated for each case. . . . .	58

3.6	Comparison of the ideal (dipole) $U$ field generated by the poses in Fig. 3.2, as per Table 3.1, and measured field, normalized to their maximum over the cases. . . . .	59
4.1	Magnetic signature optimization for follow-the-leader navigation. A. Target lumen to navigate; B. Path planning on pre-operative image; C. Signature optimization based on desired path; D. Navigation through the anatomy under applied field. . . . .	69
4.2	Building the optimization routine. A. The desired path extracted from a pre-operative image. B. The catheter as a serial chain of magnetized segments at each time-step of insertion. C. The rigid-link representation for the purpose of optimization and, inset, the three orthogonal virtual joints. D. Formulate an equilibrium at each time-step. E. Sum of the normal of each time-step gives the input to the genetic algorithm function. . . . .	71
4.3	Fabrication process to produce SCMRs with specific magnetic signatures. Independent magnetic segments with indexing features are cast from silicone doped with magnetic microparticles (NdFeB), see A. Each segment is subsequently fixed with a specific rotational alignment angle (" $\theta_m$ ") using guide pins and bespoke printed trays, and a high strength uniform magnetic field applied, see B. Magnetic segments are transferred to a second mold and arranged using their indexing features while un-doped silicone is injected into the mold, see C. Subsequent curing and demolding results in SCMRs with specific magnetic signatures, see D. . . . .	74

4.4	A. Experimental setup for comparison between tip-, axially-, and optimally-magnetized catheters. Markers were placed on the 4 magnetic segments of the catheters, on the obstacles and the target. Infrared cameras were used to track these markers. The angle $\theta$ is referred to as heading error and measures the accuracy of the tentacle to reach the target. B. Dual-arm magnetic manipulation platform for navigational bronchoscopy. A 3D printed anatomically-accurate phantom, extracted from CT imaging, is used for demonstration purposes. . . . .	76
4.5	From a pre-operative CT image to an optimized magnetic catheter. A. The slicer dataset from the CT scan. B. Datapoints are extracted and aggregated into a connectivity matrix, paths from proximal to distal nodes are extracted for three different targets. C. Optimized magnetizations will follow-the-leader shape form along their respective desired navigations. . . . .	80
4.6	Results of obstacle avoidance experiments. Comparison of tip-magnetized (A), axially-magnetized (B) and optimally-magnetized (C) catheters. The angle $\alpha$ refers to the amount of deflection, compared to the vertical axis. . . . .	81
4.7	Scenario A of comparison between the tip-magnetized (A), axially-magnetized (B) and optimally-magnetized (C) catheters. . . . .	83
4.8	Scenario B of comparison between the tip-magnetized (A), axially-magnetized (B) and optimally-magnetized (C) catheters. . . . .	84
4.9	Scenario C of comparison between the tip-magnetized (A), axially-magnetized (B) and optimally-magnetized (C) catheters. . . . .	85
4.10	Demonstration of Navigation in 3D. Highlighted in red, the shape of the catheter. On the bottom right corner of each image, the position of the EPMs (grid size $200 \times 100$ mm). On the top right corner of each last step the desired pathway for which the catheter is designed. . . . .	87
5.1	Analysis of the minimum singular value of $\nabla_R \mathcal{O}^2(\sigma_m)$ . . . . .	107
5.2	Proposed method numerical results. . . . .	111
5.3	EKF numerical results [18]. . . . .	112

---

5.4	Nonlinear Complementary Filter (NCF) numerical results [14]. . . . .	112
5.5	Error comparison over different input velocities. . . . .	113
5.6	Experimental tracking comparison ( <i>real state</i> in solid line, <i>estimated state</i> in dashed line). . . . .	115
5.7	Experimental error comparison. . . . .	115
5.8	Experimental error comparison over different input velocities. . . . .	116

# List of Tables

3.1	Field and Differential components in the 8 cases, normalized to their maximum value. . . . .	55
4.1	Summary of the results of the 2D experiments. Heading Error, Contact Time and Tracking Error through each navigation. . . . .	86
5.1	Extended Kalman Filters (EKFs) covariance matrices (simulations). . . .	113
5.2	EKFs covariance matrices (experiments). . . . .	114



# Acronyms

**CT** Computed Tomography. iii, 8, 124

**dEPM** dual External Permanent Magnet. xi, 10, 122, 123, 124, 126

**DK** Direct Kinematics. 26

**DOF** Degree of Freedom. ii, xi, 3, 4, 5, 7, 8, 9, 10, 11, 22, 46, 47, 48, 49, 50, 51, 52, 53, 54, 55, 56, 58, 59, 60, 90, 122, 123, 124, 127

**EE** End Effector. 31, 37

**EKF** Extended Kalman Filter. xv, 97, 98, 100, 109, 110, 111, 113, 114, 116, 117

**ENT** Ear Nose Throat. 2

**EPM** External Permanent Magnet. ii, xi, 3, 5, 6, 10, 11, 22, 23, 24, 25, 30, 31, 37, 48, 49, 50, 51, 52, 54, 55, 56, 57, 58, 59, 60, 122, 123

**IMU** Inertial Measurement Unit. 96, 97, 99, 107, 114

**IPM** Internal Permanent Magnet. ii, iii, vii, xi, 3, 4, 5, 6, 7, 8, 23, 24, 25, 26, 27, 30, 31, 32, 37, 48, 49, 50, 51, 52, 53, 54, 55, 56, 57, 58, 59, 60, 122, 123, 127

**MAC** Magnetic Air Capsule. 4

**MFE** Magnetic Flexible Endoscope. xi, 4, 5, 6, 22

**MRI** Magnetic Resonance Imaging. 8, 10

**NCF** Nonlinear Complementary Filter. xiv, 98, 111, 112, 113, 114, 116, 117

**ORC** Observability Rank Condition. 97, 103

**SCR** Soft Continuum Robot. 7, 11, 122, 127

**UKF** Unscented Kalman Filter. 117

# Chapter 1

## Introduction and Contributions

Endoluminal procedures have proven effective in reducing the invasiveness of both diagnosis and treatment of diseases. Limiting open surgery is proven to mitigate risk of infection, reduce post-operative pain and recovery time. For these reasons large effort has been made in converting open approaches into minimally invasive endoluminal solutions. These procedures have been successfully introduced in the gastro-intestinal tract (gastroscopy and colonoscopy), bronchi (bronchoscopy), Ear Nose Throat (ENT) surgery, intravascular and cardiac operations, to mention a few. When the target cannot be reached with a direct linear path from the insertion point (rigid endoscopy), flexible endoscopy (e.g. gastroscopy, colonoscopy) or catheterization (e.g. intravascular catheterization and navigational bronchoscopy) is required.

However, several technological limitations prevent these solutions from reaching deeper anatomical structures while guaranteeing effectiveness. In the present thesis the contributions made to the state-of-the-art of flexible endoscopy and catheterization procedures (referred to as endoluminal procedures) is presented, through the introduction of advanced design, actuation, sensing and control techniques for remote robotic actuation.

In the last two decades, the interest in remote contact-free actuation of (sub-)millimetre scale robots has soared, given the vast potential in delivering robotic solutions in areas with limited physical access [1]. This is particularly important in, but not limited to, medical diagnosis and intervention. In these cases, the complexity and limited reachability of specific anatomical structures prevents easy manual access. Robotics, intended in its computational and dexterous intelligence, has the potential of bridging the cognitive and physical gap between surgeons and the partially inaccessible anatomy.

Magnetics has been largely investigated as a solution for delivering remote actuation in the medical context [1]. The technological outcome has led to numerous breakthroughs in its clinical applications and transformed the way we may think of endoluminal procedures. Magnetic technologies have a vast span nowadays and comprise of micro-scale agents [2; 3; 4; 5] as well as millimetre-scale robots [6; 7; 8; 9]. Many of these robots have the potential or have already proven effective in revolutionizing medicine by performing

diagnostic procedures, delivering drugs or other medical aid. The work in the present thesis, focuses on millimetre scale magnetic robots, while still being influenced by the literature in the larger spectrum.

The idea behind the usage of magnetics is to apply functional forces and torques (also referred here as “wrench”) by generating an *external magnetic field*, i.e. external to the patient’s body. This field and its gradient generate torques and forces, respectively, on magnetized agents within the human anatomy. Depending on the agents’ magnetization and the applied field, the desired locomotion can be generated inside the anatomy, without direct contact between actuators and robot.

For this reason, magnetics has the advantage of miniaturization. In fact, actuation of multiple mechanical Degree of Freedom (DOF) can be achieved without the need for several on-boards actuators or transmission elements (e.g. cables, pressure lines, etc.) [10; 11]. This favours the minimization of the robots’ size and guarantees better reach when applied to endoluminal diagnosis.

The present thesis has the overall aim of improving the navigational capabilities of magnetic endoluminal devices. In the two examples discussed, colonoscopy and bronchoscopy, limited manipulation capabilities (or magneto-mechanical DOFs) may result in navigational failure. In colonoscopy, continuous Internal Permanent Magnet (IPM)-External Permanent Magnet (EPM) attraction results in reduced locomotion; in bronchoscopy limited shaping prevents navigation of the, generally, convoluted anatomy. The goal of the presented work is to investigate how design, actuation and control can be applied to guarantee successful locomotion of magnetically-actuated endoluminal devices consistently.

In the following, the concept of DOF is recurrently used. In general, the aim is to improve mechanical navigation, thus introducing more controllable mechanical DOFs. This, in the case under analysis, is strictly related to the actuated magnetic DOFs; i.e. the independent directions of the field and gradients that can be actuated by a magnetic actuation method. Overall, the combination of magnetics and mechanics generates the

DOFs we refer to as magneto-mechanical, i.e. the mechanical DOFs which are actuated magnetically.

## 1.1 Single IPM Actuation

Magnetic actuation has been investigated for several endoluminal procedures, owing its *minimal invasiveness*. Examples are cardiovascular catheterization [12; 13; 14; 9; 5], *gastroscopy* [15; 16] and *colonoscopy* [17; 18; 19; 6; 7]. These systems can be mainly subdivided in tethered [12; 13; 14; 9; 5; 17; 18; 19; 6; 7] and tetherless [15; 16].

The main focus, in most of these cases, has been navigating a single-IPM powered (wired or wireless) agent to a target region for visual (camera) diagnosis, and/or biopsy or other diagnostic procedures (e.g. ultrasound imaging [20]). In these cases, the focus was the effect of the field's functional wrench on the agent and its locomotion through the body.

The work presented in this thesis started with the Magnetic Flexible Endoscope (MFE) (also referred as Magnetic Air Capsule (MAC)), a soft-tethered magnetically tip-driven colonoscope designed to eliminate pain during the procedure (see Fig. 1.1). The front-driving approach, compared to standard rear-push, prevents the stretching of the surrounding anatomy. This can be, generally, equated to a reduction of pain and discomfort for the patient. The robotic components, comprised of highly accurate real-time localization [21] and control [6; 7], facilitates the procedure by introducing several levels of teleoperation and autonomy [22].

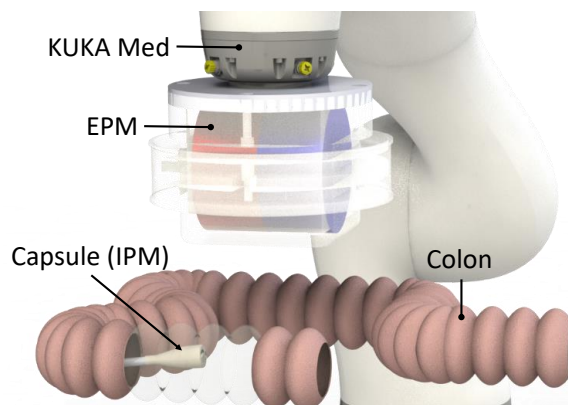


Figure 1.1: Schematic representation of the MFE.

The MFE is composed of a single IPM, at the tip of the endoscope, actuated with one EPM (see Fig. 1.1). This technology has been largely demonstrated to perform in navigation, both supervised [6; 7] and autonomous [23; 22] and ultra-sound scanning [20]. In the present work, the MFE is framed in the literature within tether and tetherless endoluminal devices. These have been largely referred to as capsule robots; thus, the name “capsule” is sometimes adopted in the present thesis.

Despite the advantages of tether-less capsules, such as wider range of motion, these constitute a complication in performing procedures such as biopsy, insufflation (needed in colonoscopy) and typically do not have enough DOFs for both locomotion and useful interaction with the anatomy. Son *et al.* [16] present a magnetic solution for biopsy, but with the loss of a possible navigational DOF. Salmanipour *et al.* [24] presented an actuation method for compensating loss of motion, by controlling up to 8 magneto-mechanical DOFs and demonstrated drug delivery capabilities. However, there are difficulties in scaling multi-DOF magnetic actuation, which constitutes a limitation in clinical procedures. For this reason, many medical technologies opted for cabled systems where sensing and functionality is not lost.

In some cases, it is convenient to adopt a tethered approach. For example: laser delivery, need for irrigation or insufflation (colonoscopy); this becomes also an advantage in localization and sensing, since wireless sensing may require on-board power supply, which may impede miniaturization. Imaging may solve this issue [25], but harmless imaging (e.g. ultrasound) may not be applicable to every area of the human body.

It became clear, in more recent years, that wired magnetic robots could deliver the necessary medical aid, when applied to millimetre scale intervention [25; 26; 5; 12; 27; 8]. In this case, however, they would not behave as an “agent” (i.e. magnetized element with free locomotion) but as a *continuum robot* [28] whose behaviour had to be analysed, described and accounted for.

Describing the full behaviour of the robot is important to predict its shaping and apply closed-loop control techniques. The interest in this topic has lead most of the related work

to focus on *Cosserat-rod modelling* [11; 26; 8]. These techniques can describe the statics of the continuum robot when wrenches are applied along its structure. It is particularly important when functional wrench is not only applied on a specific point, as in [8; 11].

However, the interaction between the robot and the surroundings is hardly accounted for and not always obvious. Anatomy may largely vary in its mechanical properties, between patients and even within the same lumen. An example is bronchoscopy, where the lumen becomes more and more elastic with depth. Another disadvantage is the computational intensity of these models, making real-time control difficult. An example is [11] where the model can run at a frequency of 1 Hz.

An initial contributions on this topic aimed at simplifying the problem, while accounting for tether-anatomy interaction is presented in [6; 7]. In this case, instead of attempting to model the full robot's behaviour, the interaction was considered as an unknown disturbance and a dynamic controller was developed to robustly reject it, both theoretically and experimentally. The work in [6] is reported in Chapter 2.

In this first work [6; 7], the following question was considered: “can we actuate the elevation of the tip, lost in continuous IPM-EPM attraction?” At the start of this investigation into the topic of magnetic actuation with one EPM, the control paradigm applied to the MFE was based on continuous attraction, i.e. the tip of the endoscope was always in contact with the top of the colon. It was clear that this would not only cause more pain than necessary, but also limit the navigational capabilities of the endoscope. In fact, the colon is anatomically comprised of folds which would commonly impede the progression of the colonoscope.

Inspired by the work of Mahoney *et al.* [15], levitation of the tip of the endoscope in air was achieved. This is a particularly challenging issue, due to the instability of the elevation dynamics and more prone, than constant IPM-anatomy interaction, to unmodelled disturbances. For this reason, the problem was also approached with consideration of its robustness to external disturbances and provision of a stable solution. It was demonstrated that the controller can readily cope with both unmodelled tether-anatomy

interaction and unknown external impulse.

**Challenges** accurate and robust control of single IPM endoscope, with mitigation of tip-anatomy interaction.

**Contributions** novel dynamic control approach to single IPM endoscopes, able to cope with anatomical interaction and stable to external disturbances.

## 1.2 Multi-IPM Devices for Navigational Dexterity

The work of Edelmann *et al.* [8] and Jeon *et al.* [5] inspired a novel concept: embedding multiple magnetic elements (permanent magnets [8; 5] or magnetized particles [12]) in a Soft Continuum Robot (SCR) to increase bending [5] or introduce more mechanical DOFs [8]. These works have motivated the interest in magnetic manipulation of SCRs which are not only actuated at the tip, as in previous works [6; 7; 26], and lead to interesting results as the ones reported by Richter *et al.* [11].

Edelmann *et al.* [8] introduced a novel concept of full-shape manipulation by modelling a SCR with multiple magnetic elements. However, they present the results in the case of single IPM in three dimensions. Based on similar results, Richter *et al.* [11] analysed the problem of manipulating two IPMs and demonstrated independent actuation in two dimensions.

These works inspired the investigation of a novel concept which combines multi-element magnetic SCRs with the idea of shape-programmable magnetic soft matter, presented by Lum *et al.* [29]: *magnetic tentacles* (see Fig. 1.2). Magnetic tentacles are the proposed solution towards optimal endoluminal access of anatomical structures which require: small size, soft tools and high dexterity. These elements have to combine with a large scale magnetic actuation system able to operate on large anatomical targets, e.g. chest.

The target of magnetic tentacles are endoluminal procedures, that generally use pre-

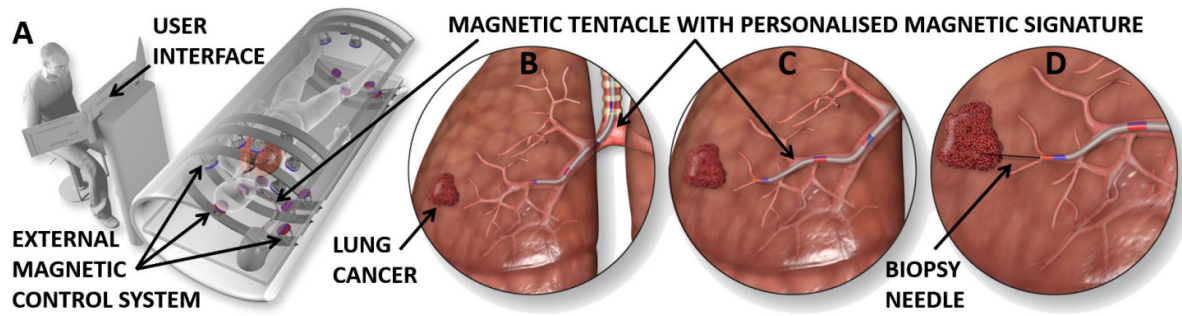


Figure 1.2: Schematic representation of an endoluminal lung procedure performed with magnetic tentacle.

operative imaging as source of navigation. An example, presented in Chapter 4, is navigational bronchoscopy. However, the general idea is to use preoperative imaging when the anatomy is too small to be navigated with on-board visualization (camera) as in colonoscopy or gastroscopy. Also, the usage of intra-operative imaging such as Computed Tomography (CT), may induce high radiation exposure on both patients and healthcare providers. The proposed approach is to take advantage of the pre-operative imaging, already necessary in the operating theatre, to inform design and fabrication of the magnetic tentacles. This, compared to the standard (pre-bent) tools or other robotic actuation methods, can lead to very small scale robots which can autonomously navigate the anatomy with minimal radiation exposure.

The idea behind *patient-specific magnetic tentacles* is to localize, in a preoperative image (e.g. CT or Magnetic Resonance Imaging (MRI)), a target and an insertion point. The former can be an anomaly or a tumor recognised by the clinician in the pre-operative phase, i.e. when analysing the image. As an insertion point, natural orifices would primarily be considered, when possible, thus minimizing pain, risk of infection and recovery time for the patient. An optimization routine, based on magneto-mechanical modelling between the tentacle and applied field, finds the magnetic signature (or profile) of the tentacle and the applied field (as dependent on time) which guarantees *follow-the-leader locomotion*, [30] under magnetic actuation. The advantage of this approach is that actuation of limited magneto-mechanical DOFs can achieve dexterous navigation when optimally distributed. This concept and the fabrication of the catheters is described in Chapter 4, alongside extensive experimental analysis of their application to bronchoscopy.

**Challenges** design and fabrication of millimetre-scale endoluminal devices which can navigate tortuous anatomical structures.

**Contributions** optimal design and fabrication of the magnetic catheters for full-dexterity in patient-specific navigation.

### 1.3 Dexterous Magnetic Actuation

Despite the possibility of optimally employing the actuated magneto-mechanical DOFs for full follow-the-leader locomotion, complete DOF independence is difficult to achieve. A seminal work, which inspired the presented investigation, is the solution to the full control of 8 DOFs presented by Salmanipour and Diller [10] and its application to capsule actuation [24]. This approach to magnetic multi-DOF actuation has the potential to revolutionize the actuation of magnetic robots, from locomotion, shaping, drug delivery and general combinations of these modalities. However, the proposed system of coils can actuate a more limited workspace, compared to permanent magnets solutions [6; 15]. Permanent magnets, despite the limitations in high-frequency actuation, can generate relatively large magnetic fields in a larger workspace, compared to coil-based approaches.

While successful actuation of multiple magneto-mechanical DOFs has been demonstrated at small scale [31; 32; 33; 34; 10; 24], by using systems of *coils*, large-scale (milli- to centimeter) manipulation is yet to be fully proven. This might require several independently-controlled coils [35; 36; 37] to be effective along any possible direction of motion. Despite their ability to generate both homogeneous fields [38] and gradients [10; 35; 39], systems of coils are less scalable, compared to permanent magnet-based magnetic actuators [40; 38; 6]. In fact, due to lower field density, higher energy-consumption and need for high-performance cooling systems, they are generally characterized by limited workspace [41; 42]. Systems of rotating permanent magnets have been proposed to mitigate these problems [43], but large scale actuation is yet to be demonstrated.

Large scale actuation systems include the coil actuation systems presented in [44; 8; 45; 46]

as well as the use of MRI for both actuation and intraoperative imaging. Both the gradient coils within an MRI [47; 48] and the fringe field created by the MRI bore magnet [49] have been shown to be suitable magnetic actuators. Successful manipulation of a tip-magnetized catheter was demonstrated in [8]. However, the high field induced by MRI systems may overwrite the magnetic signature, fundamental for the proposed follow-the-leader actuation.

To address the limitations of coils and single EPM approaches, the presented work introduces the dual External Permanent Magnet (dEPM) platform [40]. This platform, presented in Chapter 3, is a novel solution which combines the actuation of multiple magnetic DOF [10; 24] with the strong fields applicable with the usage of permanent magnets [6]. Specifically, a collaborative manipulation paradigm based of the robotic actuation of two EPMS (see Fig. 1.3) was developed. In Chapter 3, the initial results in actuating 3 independent magnetic fields and 5 gradients components are presented; this is the maximum number of magnetic DOFs that can be actuated in a point.

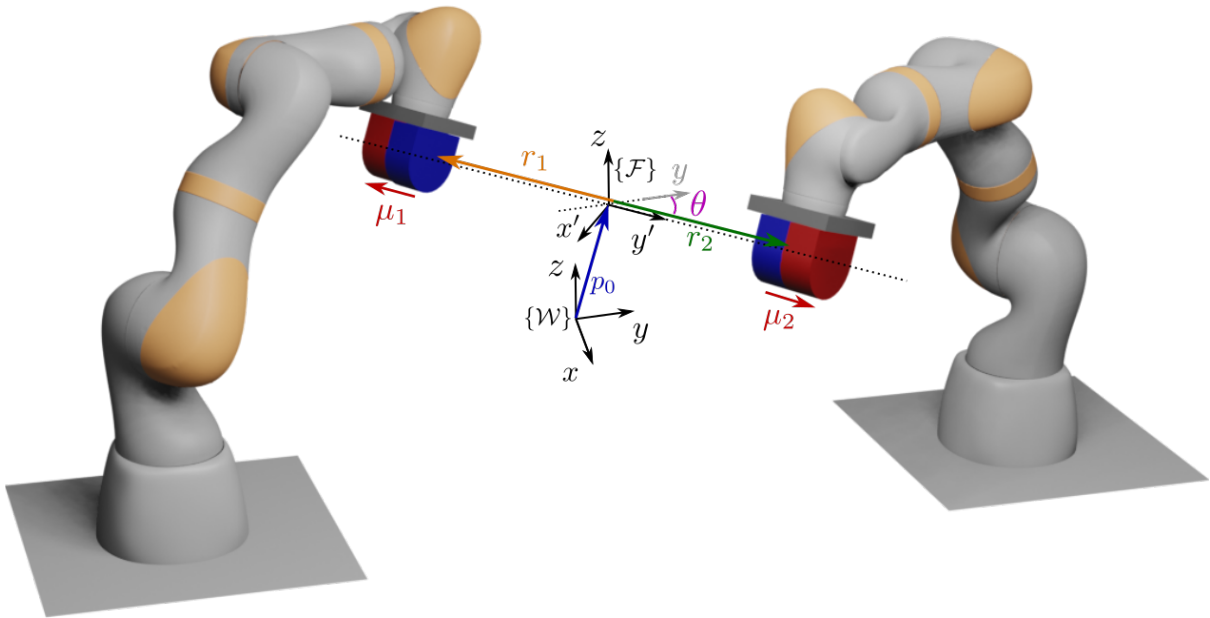


Figure 1.3: Schematic representation of the dEPM platform.

**Challenges** design of a multi-DOF magnetic actuation system which can apply strong magnetic fields in a large workspace.

**Contributions** novel actuation approach based on the collaborative manipulation of two EPMS, for the actuation of up to 8 magneto-mechanical DOFs.

In the present thesis, both single- and dual-EPM magnetic manipulation approaches are described, along with their application to endoluminal procedures. The presented work concludes with a novel localization method which has the potential of full attitude estimation within strong magnetic fields. These findings form the basis required for bringing magnetic tentacles into the medical context and introduce a novel concept in painless diagnosis and treatment.

**Summary of Contributions** The contributions of the presented thesis are: design and fabrication of patient-specific magnetic SCRs; multi-DOF magnetic actuation in a large workspace; localization of magnetic SCRs; and advanced closed-loop control of single-magnet SCRs.

The integration of these findings can overcome several limitations in the navigation of dexterous (sub-)millimetre-scale magnetic SCRs. Potentially, this can achieve full autonomous exploration of deep anatomical structures, so far unexplored.

**List of Publications** The present thesis contains material from the following publications:

- **G. Pittiglio**, L. Barducci, J. W. Martin, J. C. Norton, C. A. Avizzano, K. L. Obstein, P. Valdastri, "Magnetic Levitation for Soft-Tethered Capsule Colonoscopy Actuated With a Single Permanent Magnet: A Dynamic Control Approach," in *IEEE Robotics and Automation Letters*, vol. 4, no. 2, pp. 1224-1231, April 2019, doi: 10.1109/LRA.2019.2894907.
- **G. Pittiglio**, J. H. Chandler, M. Richter, V. K. Venkiteswaran, S. Misra and P. Valdastri, "Dual-Arm Control for Enhanced Magnetic Manipulation," 2020 *IEEE/RSJ International Conference on Intelligent Robots and Systems (IROS)*, 2020, pp. 7211-7218, doi: 10.1109/IROS45743.2020.9341250.

- **G. Pittiglio**, P. Lloyd, T. da Veiga, O. Onaizah, C. Pompili, J. H. Chandler, and P. Valdastrì, "Patient-specific Magnetic Catheters for Atraumatic Autonomous Endoscopy," *Soft Robotics* 0 0:0, doi:10.1089/soro.2021.0090.
- **G. Pittiglio**, S. Calò and P. Valdastrì, "On the Observability and Observer Design on the Special Orthogonal Group Based on Partial Inertial Sensing," in *IEEE Transactions on Automatic Control*, vol. 66, no. 10, pp. 4998-5005, Oct. 2021, doi: 10.1109/TAC.2020.3047553.

The following papers have also contributed to the work discussed in the present thesis:

- L. Barducci, **G. Pittiglio**, J. C. Norton, K. L. Obstein and P. Valdastrì, "Adaptive Dynamic Control for Magnetically Actuated Medical Robots," in *IEEE Robotics and Automation Letters*, vol. 4, no. 4, pp. 3633-3640, Oct. 2019, doi: 10.1109/LRA.2019.2928761.
- P. Lloyd, **G. Pittiglio**, J. H. Chandler and P. Valdastrì, "Optimal Design of Soft Continuum Magnetic Robots under Follow-the-leader Shape Forming Actuation," 2020 International Symposium on Medical Robotics (ISMR), 2020, pp. 111-117, doi: 10.1109/ISMR48331.2020.9312943.
- T. Da Veiga, J. H. Chandler, **G. Pittiglio**, P. Lloyd, M. Holdar, O. Onaizah, A. Alazmani, P. Valdastrì, "Material Characterization for Magnetic Soft Robots", in 2021 IEEE 4th International Conference on Soft Robotics (RoboSoft), pp. 335-342, doi: 10.1109/RoboSoft51838.2021.9479189.
- T. da Veiga, J. H. Chandler, P. Lloyd, **G. Pittiglio**, N. J. Wilkinson, A. K. Hoshier, R. A. Harris and P. Valdastrì, "Challenges of continuum robots in clinical context: a review", in *Progress in Biomedical Engineering*, vol. 2, no. 3, pp. 032003, Aug. 2020, doi: 10.1088/2516-1091/ab9f41.

## Bibliography

- [1] J. J. Abbott, E. Diller, and A. J. Petruska, “Magnetic methods in robotics,” *Annual Review of Control, Robotics, and Autonomous Systems*, vol. 3, no. 1, pp. 57–90, 2020.
- [2] A. D’Argent re, S. Perry, Y. Iwata, H. Iwasaki, E. Iwase, A. Fabozzo, I. Will, D. Rus, D. D. Damian, and S. Miyashita, “Programmable Medicine: Autonomous, Ingestible, Deployable Hydrogel Patch and Plug for Stomach Ulcer Therapy,” in *2018 IEEE International Conference on Robotics and Automation (ICRA)*, pp. 1511–1518, 2018.
- [3] X. Hu, A. Chen, Y. Luo, C. Zhang, and E. Zhang, “Steerable catheters for minimally invasive surgery: a review and future directions,” *Computer Assisted Surgery*, vol. 23, no. 1, pp. 21–41, 2018.
- [4] S. Yim, K. Goyal, and M. Sitti, “Magnetically actuated soft capsule with the multi-modal drug release function,” *IEEE/ASME Transactions on Mechatronics*, vol. 18, no. 4, pp. 1413–1418, 2013.
- [5] S. Jeon, A. K. Hoshidar, K. Kim, S. Lee, E. Kim, S. Lee, J.-y. Kim, B. J. Nelson, H.-J. Cha, B.-J. Yi, and H. Choi, “A Magnetically Controlled Soft Microrobot Steering a Guidewire in a Three-Dimensional Phantom Vascular Network,” *Soft Robotics*, vol. 6, no. 1, pp. 54–68, 2018.
- [6] G. Pittiglio, L. Barducci, J. W. Martin, J. C. Norton, C. A. Avizzano, K. L. Obstein, and P. Valdastri, “Magnetic Levitation for Soft-Tethered Capsule Colonoscopy Actuated With a Single Permanent Magnet: A Dynamic Control Approach,” *IEEE Robotics and Automation Letters*, vol. 4, no. 2, pp. 1224–1231, 2019.
- [7] L. Barducci, G. Pittiglio, J. C. Norton, K. L. Obstein, and P. Valdastri, “Adaptive Dynamic Control for Magnetically Actuated Medical Robots,” *IEEE Robotics and Automation Letters*, vol. 4, no. 4, pp. 3633–3640, 2019.
- [8] J. Edelmann, A. J. Petruska, and B. J. Nelson, “Magnetic control of continuum devices,” *International Journal of Robotics Research*, vol. 36, no. 1, pp. 68–85, 2017.

- [9] C. Chautems, A. Tonazzini, D. Floreano, and B. J. Nelson, “A variable stiffness catheter controlled with an external magnetic field,” in *2017 IEEE/RSJ International Conference on Intelligent Robots and Systems (IROS)*, pp. 181–186, 2017.
- [10] S. Salmanipour and E. Diller, “Eight-Degrees-of-Freedom Remote Actuation of Small Magnetic Mechanisms,” in *2018 IEEE International Conference on Robotics and Automation (ICRA)*, pp. 3608–3613, 2018.
- [11] M. Richter, V. K. Venkiteswaran, and S. Misra, “Multi-point orientation control of discretely-magnetized continuum manipulators,” *IEEE Robotics and Automation Letters*, vol. 6, no. 2, pp. 3607–3614, 2021.
- [12] Y. Kim, G. A. Parada, S. Liu, and X. Zhao, “Ferromagnetic soft continuum robots,” *Science Robotics*, vol. 4, no. 33, p. eaax7329, 2019.
- [13] C. Heunis, J. Sikorski, and S. Misra, “Flexible Instruments for Endovascular Interventions: Improved Magnetic Steering, Actuation, and Image-Guided Surgical Instruments,” *IEEE robotics automation magazine*, vol. 25, no. 3, pp. 71–82, 2018.
- [14] S. Ernst, F. Ouyang, C. Linder, K. Hertting, F. Stahl, J. Chun, H. Hachiya, D. Bän-sch, M. Antz, and K.-H. Kuck, “Initial experience with remote catheter ablation using a novel magnetic navigation system,” *Circulation*, vol. 109, no. 12, pp. 1472–1475, 2004.
- [15] A. W. Mahoney and J. J. Abbott, “Five-degree-of-freedom manipulation of an un-tethered magnetic device in fluid using a single permanent magnet with application in stomach capsule endoscopy,” *The International Journal of Robotics Research*, vol. 35, no. 1-3, pp. 129–147, 2016.
- [16] D. Son, S. Yim, and M. Sitti, “A 5-D localization method for a magnetically ma-nipulated untethered robot using a 2-D array of Hall-effect sensors,” *IEEE/ASME Transactions on Mechatronics*, vol. 21, no. 2, pp. 708–716, 2015.
- [17] A. Arezzo, A. Menciassi, P. Valdastri, G. Ciuti, G. Lucarini, M. Salerno, C. Di Natali, M. Verra, P. Dario, and M. Morino, “Experimental assessment of a novel robotically-

- driven endoscopic capsule compared to traditional colonoscopy,” *Digestive and Liver Disease*, vol. 45, no. 8, pp. 657–662, 2013.
- [18] P. Valdastri, C. Quaglia, E. Susilo, A. Menciassi, P. Dario, C. N. Ho, G. Anhoeck, and M. O. Schurr, “Wireless therapeutic endoscopic capsule: in vivo experiment,” *Endoscopy*, vol. 40, no. 12, pp. 979–982, 2008.
- [19] P. Valdastri, G. Ciuti, A. Verbeni, A. Menciassi, P. Dario, A. Arezzo, and M. Morino, “Magnetic air capsule robotic system: proof of concept of a novel approach for painless colonoscopy,” *Surgical endoscopy*, vol. 26, no. 5, pp. 1238–1246, 2012.
- [20] J. C. Norton, P. R. Slawinski, H. S. Lay, J. W. Martin, B. F. Cox, G. Cummins, M. P. Y. Desmulliez, R. E. Clutton, K. L. Obstein, and S. Cochran, “Intelligent magnetic manipulation for gastrointestinal ultrasound,” *Science Robotics*, 2019.
- [21] A. Z. Taddese, P. R. Slawinski, M. Pirotta, E. De Momi, K. L. Obstein, and P. Valdastri, “Enhanced real-time pose estimation for closed-loop robotic manipulation of magnetically actuated capsule endoscopes,” *The International journal of robotics research*, vol. 37, no. 8, pp. 890–911, 2018.
- [22] J. W. Martin, B. Scaglioni, J. C. Norton, V. Subramanian, A. Arezzo, K. L. Obstein, and P. Valdastri, “Enabling the future of colonoscopy with intelligent and autonomous magnetic manipulation,” *Nature Machine Intelligence*, vol. 2, no. 10, pp. 595–606, 2020.
- [23] P. R. Slawinski, A. Z. Taddese, K. B. Musto, K. L. Obstein, and P. Valdastri, “Autonomous retroflexion of a magnetic flexible endoscope,” *IEEE Robotics and Automation Letters*, vol. 2, no. 3, pp. 1352–1359, 2017.
- [24] S. Salmanipour, O. Youssefi, and E. D. Diller, “Design of multi-degrees-of-freedom microrobots driven by homogeneous quasi-static magnetic fields,” *IEEE Transactions on Robotics*, vol. 37, no. 1, pp. 246–256, 2021.
- [25] J. Sikorski, C. M. Heunis, R. Obeid, V. K. Venkiteswaran, and S. Misra, “A flexible

- catheter system for ultrasound-guided magnetic projectile delivery,” *IEEE Transactions on Robotics*, pp. 1–14, 2021.
- [26] L. B. Kratchman, T. L. Bruns, J. J. Abbott, and R. J. Webster, “Guiding Elastic Rods with a Robot-Manipulated Magnet for Medical Applications,” *IEEE Transactions on Robotics*, vol. 33, no. 1, pp. 227–233, 2017.
- [27] T. L. Bruns, K. E. Riojas, D. S. Ropella, M. S. Cavilla, A. J. Petruska, M. H. Freeman, R. F. Labadie, J. J. Abbott, and R. J. Webster, “Magnetically steered robotic insertion of cochlear-implant electrode arrays: System integration and first-in-cadaver results,” *IEEE Robotics and Automation Letters*, vol. 5, no. 2, pp. 2240–2247, 2020.
- [28] T. da Veiga, J. H. Chandler, P. Lloyd, G. Pittiglio, N. J. Wilkinson, A. K. Hoshier, R. A. Harris, and P. Valdastri, “Challenges of continuum robots in clinical context: a review,” *Progress in Biomedical Engineering*, vol. 2, p. 032003, aug 2020.
- [29] G. Z. Lum, Z. Ye, X. Dong, H. Marvi, O. Erin, W. Hu, and M. Sitti, “Shape-programmable magnetic soft matter,” *Proceedings of the National Academy of Sciences*, vol. 113, no. 41, pp. E6007–E6015, 2016.
- [30] C. Culmone, S. F. Yikilmaz, F. Trauzettel, and P. Breedveld, “Follow-the-leader mechanisms in medical devices: A review on scientific and patent literature,” *IEEE Reviews in Biomedical Engineering*, pp. 1–1, 2021.
- [31] J. Edelmann, A. J. Petruska, and B. J. Nelson, “Estimation-Based Control of a Magnetic Endoscope without Device Localization,” *Journal of Medical Robotics Research*, vol. 03, no. 01, p. 1850002, 2018.
- [32] A. Hong, A. J. Petruska, A. Zemmar, and B. J. Nelson, “Magnetic Control of a Flexible Needle in Neurosurgery,” *IEEE Transactions on Biomedical Engineering*, vol. 68, no. 2, pp. 616–627, 2021.
- [33] T. L. Bruns, K. E. Riojas, D. S. Ropella, M. S. Cavilla, A. J. Petruska, M. H. Freeman, R. F. Labadie, J. J. Abbott, and R. J. Webster, “Magnetically Steered

- Robotic Insertion of Cochlear-Implant Electrode Arrays: System Integration and First-In-Cadaver Results,” *IEEE Robotics and Automation Letters*, vol. 5, no. 2, pp. 2240–2247, 2020.
- [34] M. C. Hoang, K. T. Nguyen, V. H. Le, J. Kim, E. Choi, B. Kang, J. O. Park, and C. S. Kim, “Independent Electromagnetic Field Control for Practical Approach to Actively Locomotive Wireless Capsule Endoscope,” *IEEE Transactions on Systems, Man, and Cybernetics: Systems*, vol. 51, no. 5, pp. 3040–3052, 2021.
- [35] M. Richter, V. K. Venkiteswaran, and S. Misra, “Multi-Point Orientation Control of Discretely-Magnetized Continuum Manipulators,” *IEEE Robotics and Automation Letters*, vol. 6, no. 2, pp. 3607–3614, 2021.
- [36] Z. Yang, L. Yang, M. Zhang, Q. Wang, S. C. H. Yu, and L. Zhang, “Magnetic Control of a Steerable Guidewire Under Ultrasound Guidance Using Mobile Electromagnets,” *IEEE Robotics and Automation Letters*, vol. 6, no. 2, pp. 1280–1287, 2021.
- [37] R. Chen, D. Folio, and A. Ferreira, “Mathematical approach for the design configuration of magnetic system with multiple electromagnets,” *Robotics and Autonomous Systems*, vol. 135, p. 103674, 2021.
- [38] J. J. Abbott, E. Diller, and A. J. Petruska, “Magnetic Methods in Robotics,” *Annual Review of Control, Robotics, and Autonomous Systems*, vol. 3, pp. 57–90, may 2020.
- [39] T. da Veiga, J. H. Chandler, P. Lloyd, G. Pittiglio, N. J. Wilkinson, A. K. Hoshiar, R. A. Harris, and P. Valdastrì, “Challenges of continuum robots in clinical context: a review,” *Progress in Biomedical Engineering*, vol. 2, no. 3, p. 32003, 2020.
- [40] G. Pittiglio, J. H. Chandler, M. Richter, V. K. Venkiteswaran, S. Misra, and P. Valdastrì, “Dual-Arm Control for Enhanced Magnetic Manipulation,” in *2020 IEEE/RSJ International Conference on Intelligent Robots and Systems (IROS)*, pp. 7211–7218, 2020.
- [41] M. Yousefi and H. Nejat Pishkenari, “Independent position control of two identical

- magnetic microrobots in a plane using rotating permanent magnets,” *Journal of Micro-Bio Robotics*, vol. 17, no. 1, pp. 59–67, 2021.
- [42] J. Sikorski, I. Dawson, A. Denasi, E. E. Hekman, and S. Misra, “Introducing Big-Mag - A novel system for 3D magnetic actuation of flexible surgical manipulators,” *Proceedings - IEEE International Conference on Robotics and Automation*, pp. 3594–3599, 2017.
- [43] P. Ryan and E. Diller, “Magnetic actuation for full dexterity microrobotic control using rotating permanent magnets,” *IEEE Transactions on Robotics*, vol. 33, no. 6, pp. 1398–1409, 2017.
- [44] A. J. Petruska, J. Edelmann, and B. J. Nelson, “Model-Based Calibration for Magnetic Manipulation,” *IEEE Transactions on Magnetism*, vol. 53, no. 7, pp. 1–6, 2017.
- [45] Magnetecs, “Magnetecs: Guiding Medical Technology.” <http://www.magnetecs.com/overview.php>, 2021.
- [46] K. Mandal, F. Parent, S. Martel, R. Kashyap, and S. Kadoury, “Vessel-based registration of an optical shape sensing catheter for MR navigation,” *International Journal of Computer Assisted Radiology and Surgery*, vol. 11, no. 6, pp. 1025–1034, 2016.
- [47] O. Erin, D. Antonelli, M. E. Tiryaki, and M. Sitti, “Towards 5-DoF Control of an Untethered Magnetic Millirobot via MRI Gradient Coils,” in *2020 IEEE International Conference on Robotics and Automation (ICRA)*, pp. 6551–6557, 2020.
- [48] O. Erin, C. Alici, and M. Sitti, “Design, Actuation, and Control of an MRI-Powered Untethered Robot for Wireless Capsule Endoscopy,” *IEEE Robotics and Automation Letters*, vol. 6, no. 3, pp. 6000–6007, 2021.
- [49] A. Azizi, C. C. Tremblay, K. Gagné, and S. Martel, “Using the fringe field of a clinical MRI scanner enables robotic navigation of tethered instruments in deeper vascular regions,” *Science Robotics*, vol. 4, no. 36, p. eaax7342, 2019.

## Chapter 2

# Single Magnet Control

**Chapter source:** G. Pittiglio, L. Barducci, J. W. Martin, J. C. Norton, C. A. Avizzano, K. L. Obstein, P. Valdastri, "Magnetic Levitation for Soft-Tethered Capsule Colonoscopy Actuated With a Single Permanent Magnet: A Dynamic Control Approach," in IEEE Robotics and Automation Letters, vol. 4, no. 2, pp. 1224-1231, April 2019, doi: 10.1109/LRA.2019.2894907.

**Other related papers:** L. Barducci, G. Pittiglio, J. C. Norton, K. L. Obstein and P. Valdastri, "Adaptive Dynamic Control for Magnetically Actuated Medical Robots," in IEEE Robotics and Automation Letters, vol. 4, no. 4, pp. 3633-3640, Oct. 2019, doi: 10.1109/LRA.2019.2928761.

## Abstract

The present paper investigates a novel control approach for magnetically driven soft-tethered capsules for colonoscopy - a potentially painless approach for colon inspection. The focus of this work is on a class of devices composed of a magnetic capsule endoscope actuated by a single external permanent magnet. Actuation is achieved by manipulating the external magnet with a serial manipulator, which in turn produces forces and torques on the internal magnetic capsule. We propose a control strategy which, counteracting gravity, achieves levitation of the capsule. This technique, based on a nonlinear backstepping approach, is able to limit contact with the colon walls, reducing friction, avoiding contact with internal folds and facilitating the inspection of non-planar cavities. The approach is validated on an experimental setup which embodies a general scenario faced in colonoscopy. The experiments show that we can attain 19.5 % of contact with the colon wall, compared to the almost 100 % of previously proposed approaches. Moreover, we show that the control can be used to navigate the capsule through a more realistic environment - a colon phantom - with reasonable completion time.

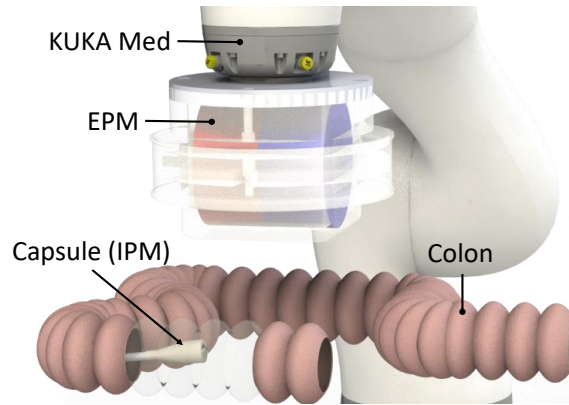


Figure 2.1: Schematic representation of the platform.

## 2.1 Introduction

Over the last decade, magnetically actuated robotic platforms have had a significant impact in the field of medical robotics, providing new tools to facilitate minimally invasive diagnosis and therapy in different regions of the human body. The main advantage of magnetically actuated robots is the application of functional forces and torques without the need for the alternative, often complex and bulky on-board locomotion mechanisms. Due to this advantage, these devices have been investigated for several endoscopic procedures such as *colonoscopy* [1; 2; 3], *gastroscopy* [4], *cardiac applications* [5; 6; 7; 8; 9], *surgery* [10] and *bronchoscopy* [11].

In general, magnetically actuated endoscopic robots can be subdivided in terms of external actuation, between *coil-based* [12; 13; 5; 14; 15; 16; 17], *rotating permanent magnets-based* [18; 19] and *permanent magnet-based* [1; 2; 3; 4; 20] devices. The first ones generate a magnetic field, generally, based on the usage of multiple coils within a predefined workspace. The second ones make use of rotating magnets instead of coils. Permanent magnet-based devices are actuated by a single permanent magnet, manipulated by a serial robot.

Systems that use multiple coils generally have higher controllability owing to the fine control over the magnetic field within the workspace. However, these systems are often more bulky, have a confined workspace, are expensive and have a high energy consumption that may hinder their practical use.

Rotating permanent magnets-based devices, permit 6 Degrees of Freedom (DOFs) steering, when employing multiple magnets [19]. This approach avoids heating normally associated with using coils, but shares the same limitations in terms of workspace.

The focus of the present work is Magnetic Flexible Endoscope (MFE) actuated with single External Permanent Magnet (EPM) [1; 3], shown in Fig. 2.1. This has been investigated as an alternative to standard colonoscopy, with the main advantages of being ease-of-use and reduced patient discomfort - two significant drawbacks with the current procedure. Standard colonoscopes, pushed from outside the body, advance through the colon by exerting pressure on the bowel wall. This environmental interaction is needed to steer the device and conform its shape to the tortuous lumen. On-the-other-hand, soft-tethered magnetic capsules are controlled by an externally applied force focused at the tip of the device. Therefore, in order to advance the capsule, there is no need to exert stress on the lumen; the forces are applied in the required direction only and the soft tether follows passively.

We refer to the flexible endoscope as a “soft-tethered capsule” since our main focus is navigating its tip (capsule). The tether, within the scope of this work, is not considered and its interaction with the anatomy is faced as it was a disturbance. The presented method could also be applied to untethered capsules, thus we use the word “capsule” for generality’s sake.

However, a potential limitation of this platform is the continuous attraction of the capsule to the EPM and lack of gravity compensation [21]. This may cause the capsule to become trapped in the anatomically complex and unstructured environment of the colon and may hinder locomotion through a steeply sloping lumen. The method in [21] is able only to control 4 DOFs: 2 DOFs on the plane, pitch and yaw. However, magnetic coupling between 2 single-dipole permanent magnets inherently permits the actuation of 5 DOFs; due to the cylindrical symmetry of the magnetic field, capsule roll is not possible. Therefore, the goal of our contribution is to enhance current practice by adding the actuation of the 5th DOF: the one along the gravity direction. This aims to reduce contact

with the environment and facilitate locomotion. However, the fundamental challenge of the proposed approach is that the equilibrium between magnetic force and gravity is highly unstable and, therefore, the control design is nontrivial.

While levitation is technically easier to implement in coil-based systems [22], in this paper we aim to show that accurate control can be used to counter the limited controllability of systems with a single EPM. We show that levitation (controlling the capsule in the gravity direction) is feasible and can be done in free-space, i.e. without the need for a fluid medium [4]. This is relevant in the context of colonoscopy because the lumen is routinely distended with a gas medium. This control strategy can bring significant benefit as it facilitates the avoidance of obstacles (eg. tissue folds), a reduction in contact force and therefore, a reduction in both friction and risk of trauma or discomfort. It may also assist with navigating sloped regions of the colon.

This paper is organized as follows: in Section 2.2 we provide a general overview of the method, which is explored further in Section 2.3. Sections 2.4 and 2.5 present the experimental data, which aims to prove the strength of the proposed approach; the former discusses free space levitation in a L-shaped acrylic tube, the latter reports the results obtained in a more realistic colon phantom. Section 5.8 draws our main conclusions and discusses future work. In Appendix 2.6 we give detail on the basics of magnetic manipulation and Appendix 2.6 reports proofs of lemmas and theorems employed in the paper.

## 2.2 Method

In the following we aim to describe a general approach for magnetic capsule levitation using a single EPM. The EPM is controlled by a serial manipulator and the capsule contains a magnet, referred to as Internal Permanent Magnet (IPM)<sup>1</sup>. This is shown in Fig. 2.1. Achieving accurate control with robotically actuated permanent magnets [4] is

---

<sup>1</sup>In the following we use the name Internal Permanent Magnet also in reference to the magnetic capsule.

challenging, due largely to the high inertia related to the movements of the large EPM and serial manipulator, compared to current flow. Moreover, when considering only a single magnetic source, point-wise control of the magnetic field and its gradient is not as straightforward as in using multiple coils.

In order to achieve levitation we need to guarantee that the force on the IPM counteracts gravity, in an equilibrium state that is highly unstable. The approach taken can either be to design a controller aware of the dynamics of the IPM or to design a suitable trajectory planner that does not require the dynamic equilibrium to be considered. Our initial approach was to pursue the latter and avoid the use of the system dynamics. As is shown in subsequent sections, this is a feasible approach that achieves asymptotic stability.

The overall control strategy is based on the *backstepping technique* and the global stability is formally proved by means of a Lyapunov-based approach [23]. This is guaranteed under the assumption that the desired trajectory of the IPM is a *piecewise-constant* function of the time. This means that desired velocity and acceleration of the IPM can be neglected. In this condition, a PD controller can be designed to steer the IPM and achieve asymptotic convergence. The assumption made does not interfere with the design of the controller, nor is limiting in any case when a smooth planning can be achieved.

This control technique uses capsule localization (100 Hz, 4 mm accuracy) [24], where the pose and inferred force and torque are known.

We chose a backstepping control approach since it permits a local linearization of the wrench applied to the capsule with respect to the robot's joint variables. The alternative approach of inverting the wrench-joint nonlinear relationship may result in computationally expensive iterative algorithms.

## 2.3 Dynamic Control

We take into account a *back-stepping* approach [23] on two levels (or loops): pose loop (Section 2.3.1) and force loop (Section 2.3.2). The latter, considered as an internal loop,

is designed to guarantee the convergence of the actual force on the IPM to the desired one, while the former aims to steer the IPM. The presence of the internal force loop improves the control properties, compared to previous approaches [21; 4], and it is fundamental for levitation. Given the unstable force equilibrium, it is essential to guarantee the stability of this internal loop before attempting to steer the IPM. This control strategy is summarized in Fig. 2.2.

In this work, we only consider the dynamics of the capsule subject to forces and torques exerted by the EPM. These forces and torques, embedded in the vector  $\tau_m \in \mathbb{R}^n$ , depend on the relative position between the IPM and EPM, as described in the Appendix 2.6. In general,  $n = 5$  for single external magnetic source and  $n = 6$  for multiple magnetic sources [14]. We consider that the two permanent magnets can be approximated with the *dipole model*, which is enough accurate given their geometry and relative distance. Possible errors related to dipole modelling are discussed along with the experimental data provided in Sections 2.4. For the sake of clarity, we discuss any implication, mathematical operator and variable in Appendix 2.6.

In the present work, the presence of a tether is considered an unmodelled disturbance. In the specific case under analysis, the tether is beneficial as it acts as a stabilizing damper on the dynamics along the gravity direction, improving stability in the system. There is no limitation in applying the proposed method to untethered capsules, but we expect the need for a faster control loop to handle the less damped dynamics.

Consider the nominal dynamics of the capsule

$$B(x)\ddot{x} + C(x, \dot{x})\dot{x} + G(x) = \tau_m(x, q), \quad (2.1)$$

where  $x \in \mathbb{R}^n$  is the capsule pose (position and orientation) and  $q \in \mathbb{R}^m$  embeds the robot joint variables; matrices  $B(x)$ ,  $C(x, \dot{x})$ ,  $G(x)$  are the respective *inertia*, *Coriolis matrix* and *gravity* [25]. Our aim is to find  $q$  such that  $x$  approaches a desired value  $x_d$ .

The relationship  $\tau_m(x, q)$  is the magnetic dipole force and torque exerted by the EPM

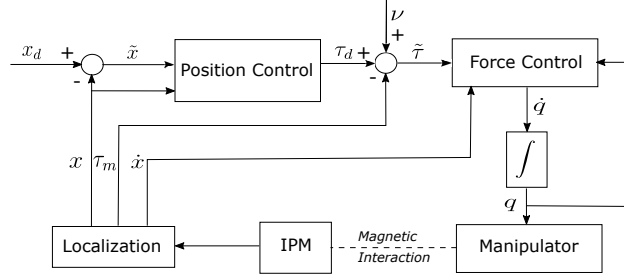


Figure 2.2: Control scheme.

on the IPM. This relationship is highly nonlinear, confounding computation of  $q$  given the desired force and torque on the IPM. Appendix 2.6 describes this in more detail. Therefore, we consider a time derivation of this function [21], which reads as

$$\dot{\tau}_m = \frac{\partial \tau(x, q)}{\partial x} \dot{x} + \frac{\partial \tau(x, q)}{\partial q} \dot{q} = J_x \dot{x} + J_q \dot{q}, \quad (2.2)$$

and turns  $\tau_m$  into a state variable for the system we aim to control and  $\dot{q}$  into the control input; matrices  $J_x$  and  $J_q$  are derived in the Appendix 2.6. The variables  $\dot{q}$  can be integrated to control the robot through its Direct Kinematics (DK) [25]. The novelty of our control system, compared to [21], is that we apply a closed-loop control on  $\tau_m$ .

The overall dynamics we aim to control reads as

$$\begin{cases} B(x)\ddot{x} + C(x, \dot{x})\dot{x} + G(x) = \tau \\ \dot{\tau} = J_x \dot{x} + J_q \dot{q} + \dot{\nu} \end{cases}, \quad (2.3)$$

where  $\nu$  models the tether interaction with the environment, for example: drag, elastic behaviour and friction;  $\tau$  is the actual force and torque on the capsule. The localization method [24] ensures that  $x$  and  $\dot{x}$  can be measured. The robot joints are measured by the embedded encoders.

In the following sections we describe the main steps in the derivation of the controller and conclude by proving the stability of the controlled system, using Lemma 2.1 and Theorem 2.3 (described in detail in Appendix 2.6).

### 2.3.1 Pose Control

Defining a pose controller that attempts to steer the IPM to a desired trajectory ( $x_d$ ) is the first step and is achieved by first considering that  $\tau$  can be deliberately set as a control input for the upper dynamics in (2.3). Because of the nonlinearities described in Appendix 2.6, we attempt to find a set of desired forces and torques (referred to as  $\tau_d$ ). Afterwards, as described in the next section, we aim to control the actual torque ( $\tau$ ) to  $\tau_d$ . The stability of this backstepping approach, as shown in Section 2.3.3, guarantees the overall convergence.

We want to prove that the *PD with gravity compensation*

$$\tau_d = G(x) + K_p \tilde{x} + K_d \dot{\tilde{x}}, \quad (2.4)$$

with  $\tilde{x} = x_d - x$ , guarantees  $x \rightarrow x_d$  as  $\tau \rightarrow \tau_d$ . This is achieved under the following assumption.

#### Assumption 1

The steering of the IPM is achieved by considering that:

- the force control, described in Section 2.3.2, is faster than the system dynamics in (2.1);
- the desired trajectory is a *piece-wise constant function of the time*.

The former leads to assume that there exists an instant  $T$ ,  $0 < T \ll 1$ , such that  $\tau(t) = \tau_d(t)$ ,  $t \geq T$ . In other words, we consider almost instantaneous convergence of force and torque. This simplification is used to prove the first step of the backstepping; Section 2.3.3 discusses the case of a weaker assumption. The need for this assumption is justified by the following lemma, on which the final proof of this work (Theorem 2.3) is based.

**Lemma 2.1.** *Under Assumption 1, the pose controller in (2.4) achieves asymptotic stability of the error  $\tilde{x}$ , for any positive definite design gains  $K_p$  and  $K_d$ .*

Appendix II includes further details on this.

### 2.3.2 Force Control

The second step in the design of the controller is to ensure that  $\tau$  converges to  $\tau_d$  and do so almost instantaneously (according to Assumption 1). The magnetic force and torque are computed from  $x$  and  $q$  by employing the localization data and dipole model.

In order to design an asymptotically stable controller for force and torque, we take into account (2.2) and search for  $\dot{q}$  such that the dynamics for  $\tilde{\tau} = \tau_d - \tau_m$  evolves as

$$\dot{\tilde{\tau}} = -K\tilde{\tau}, \quad (2.5)$$

with  $K$  positive definite design gain. This leads to asymptotic stability of the force and torque error dynamics.

By substituting (2.2) into (2.5) we obtain

$$\begin{aligned} \dot{\tau}_d - \dot{\tau}_m &= -K\tilde{\tau} \\ \dot{\tau}_d - J_x\dot{x} - J_q\dot{q} &= -K\tilde{\tau} \end{aligned}$$

whose solution, with respect to  $\dot{q}$ , is

$$\dot{q} = J_q^\dagger(\dot{\tau}_d + K\tilde{\tau} - J_x\dot{x}). \quad (2.6)$$

Here  $(\cdot)^\dagger$  stands for the *Moore-Penrose pseudoinverse* [25]. Note that the derivative of the desired torque  $\tau_d$  can be analytically computed from the localization data, by following the steps in Appendix 2.6.

**Lemma 2.2.** *Under the assumption that the disturbance  $\nu \simeq 0$ , any positive definite gain  $K$  achieves stability of the torque dynamics.*

*Proof.* Under the drawn assumption,  $\tau \simeq \tau_m \rightarrow \tau_d$ . □

Assuming the tether interactions to be negligible is justified by the fact that the tether used in our platform interacts with the environment with a very low friction coefficient - the tether and colon are both smooth and lubricated. Furthermore, considering that the tether is significantly stiffer than the colon, the elastic restoring forces would have minimal impact on capsule dynamics and any deformation would be seen primarily in the wall of the colon.

### 2.3.3 Overall Control

In the following, we describe the overall control strategy by considering the above results.

In particular, we show that with the choice of  $\dot{q}$

$$\begin{cases} \tau_d &= G(x) + K_p \tilde{x} + K_d \dot{\tilde{x}} \\ \dot{q} &= J_q^\dagger(\dot{\tau}_d + K \tilde{\tau} - J_x \dot{x} - \dot{x}) \end{cases}, \quad (2.7)$$

we can weaken Assumption 1. The new choice of  $\dot{q}$  leads to

$$\dot{\tilde{\tau}} = -K \tilde{\tau} + \dot{x},$$

which achieves overall convergence, as discussed in Theorem 2.3. Therefore, the assumption under which we guarantee the overall convergence of the controlled system is the following.

#### Assumption 2

The desired trajectory  $x_d$  is *piece-wise constant function* of the time and  $\nu \simeq 0$ .

We can prove the convergence of the controlled dynamics, as in the following theorem.

**Theorem 2.3.** *Under Assumption 2, the controller defined in (2.7) achieves asymptotic stability of the dynamics (2.3), for any positive definite design gains  $K_p$ ,  $K_d$  and  $K$ .*

This is elaborated in Appendix 2.6.

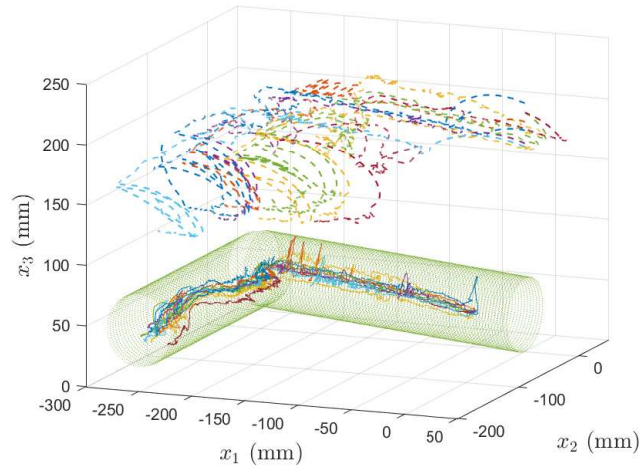
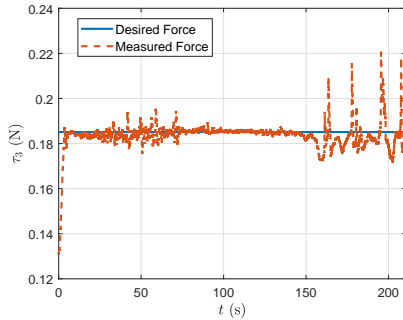
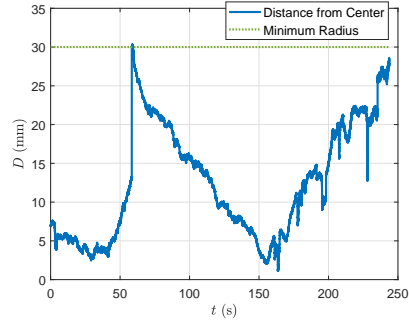


Figure 2.3: 3D tracking. The IPM (solid line) and EPM (dashed line) trajectories for all trials performed.



(a) Mean levitating force.



(b) Mean distance from wall.

## 2.4 Experimental Analysis: Free Space Levitation

The aim of the experimental work was to show that we can achieve levitation, including steering the capsule through inclined trajectories. This could be an essential tool for facilitating effective locomotion in the presence of obstacles and complex colon geometries. A video of the experiments is reported in the attached media of the paper.

The IPM was first placed into an acrylic tube with a realistic inner diameter of 60 mm [26], bent at an angle of 90 degrees in the center. Each half of the tube was 250 mm long. The tube was inclined by approximately 20 mm over its length. This was chosen to show our controller performance when moving the capsule along the gravity direction ( $x_3$ ).

The IPM (axially magnetized, 21 mm diameter, 19 mm length, 15 g mass) is actuated using an EPM (axially magnetized, 101.6 mm diameter and length, 1.48T, N52) at the

End Effector (EE) of a serial manipulator (KUKA LBR Med R820<sup>2</sup>). Localization [24] and control loop both run at approximately 100 Hz. The error in the dipole models were computed by considering [27] and the conditions during experiments. For the EPM, the maximum and mean error were 13 % and 3 % respectively. Whereas the corresponding errors for the IPM were 0.2 % and 0.06 % respectively. Magnetic interference was minimized by keeping the workspace free from ferromagnetic materials.

To show the efficacy of the control strategy, we commanded the capsule to traverse the acrylic tube in 10 trials. We report the 3D trajectories of the IPM and EPM in Fig. 2.3. The mean force along the gravity direction ( $\tau_3$ ), measured throughout the trajectories, is shown in Fig. 2.4a. The mean distance between the capsule and the center of the tube ( $D$ ), is shown in Fig. 2.4b. These both give an indication of the levitation performance; in-other-words, how effectively the system prevents the capsule from touching the surrounding walls.

We controlled the capsule to be in the center of the lumen on the  $x_1 - x_2$  plane while maintaining the minimum height on the axis  $x_3$  which achieves levitation - i.e. where  $\tau_3$  counteracts gravity. In the first part of the tube, this objective translates directly into levitating the capsule, as shown in Fig. 2.3. On-the-other-hand, in the second half of the path, the stiffness of the tether and acrylic tube leads to capsule-tube contact because of their large resistance to deformation. In this case the EPM is not able to exert enough force to counteract this resistance. Although the tether properties negatively impact simultaneous steering and levitation, the experiments show that the control strategy can resume capsule levitation after moving past the corner.

Fig. 2.4b quantifies the amount of contact with the internal wall. The event of the capsule touching the wall is quantified by geometric constraints and real-time localization. The latter provides information about the position of the capsule inside the acrylic tube (upon an initial registration). The result is that, on average, the capsule is in contact with the tube 19.5 % of the time, compared to almost 100 % for previous methods [21]. Less

---

<sup>2</sup><https://www.kuka.com/en-gb/industries/health-care/kuka-medical-robotics>

contact with the environment can be equated to smoother locomotion.

## 2.5 Experimental Analysis: Colon Phantom

In the following we describe an experiment performed on the M40 Colonoscope Training Simulator<sup>3</sup> in *standard configuration*. The aim was to show that the proposed method is able to control the IPM in a more realistic environment that is deformable, unstructured and contains obstacles. While quantitative feedback on capsule-environment contact could not be measured in this setup, the results show the feasibility of pursuing this control strategy.

These tests also validate our assumption of considering the tether dynamics as a disturbance, as the capsule is able to successfully traverse the complex environment despite tether-environment interaction. The colon has a low stiffness and provides little resistance to deformation from the comparatively stiffer tether.

We performed 5 trials in which the user (an individual with no prior endoscopic experience, but knowledge of the system) was tasked with traversing the colon phantom from sigmoid to caecum. The user was provided with visual feedback from the capsule's on-board camera and could manipulate the capsule pose using a 3D mouse. This setup is shown in Fig. 2.5.

In Fig. 2.6 we show the colon phantom with all 5 trajectories overlaid. An example of one of these trials can be seen in the supplementary media attachment.

The overall task had a mean completion time of 346.78 s with standard deviation of 119.37 s, for a path of approximately 0.85 m. This would equate to exploring a typical human colon in approximately 13 min, assuming an average colon length of 1.85m [26] and a mean capsule velocity of 2 mm/s seen in these experiments. In order to investigate the real performance of the proposed approach, a deeper analysis will be performed with expert users, as in [1].

---

<sup>3</sup><https://www.kyotokagaku.com/products/detail01/m40.html>

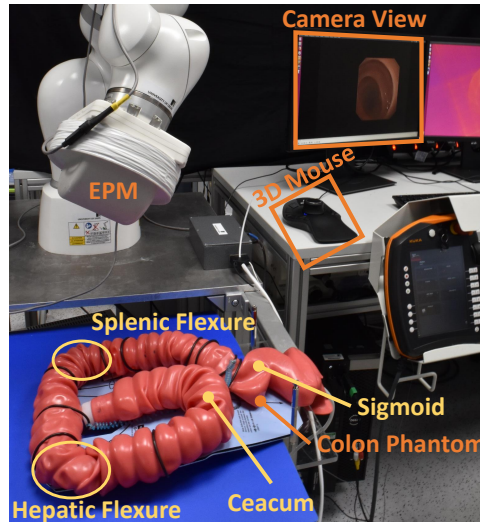


Figure 2.5: Experimental setup: colon simulator.

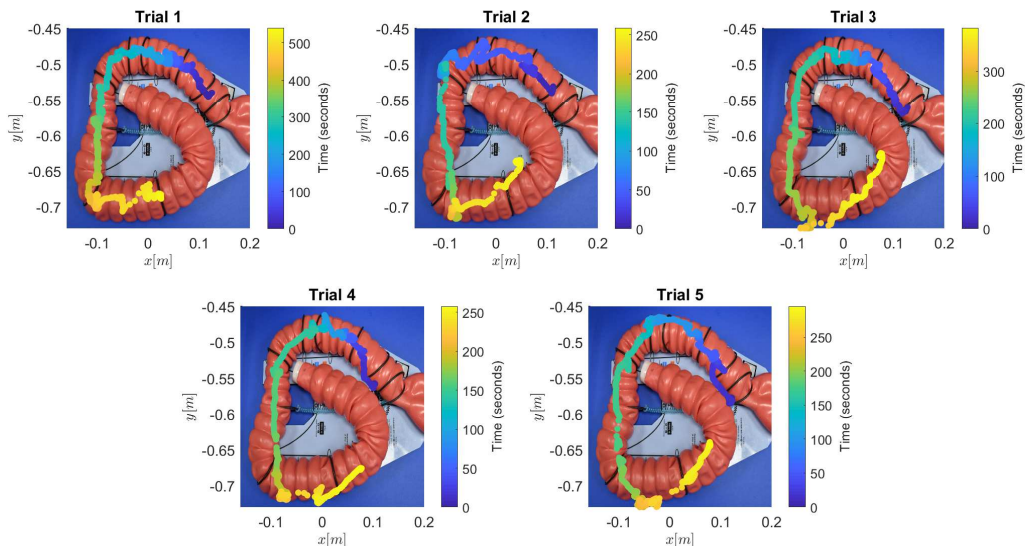


Figure 2.6: Trials on the colon simulator.

Increasing the velocity is related to two factors: the frequency of the control loop and the need for Assumption 2. The current localization frequency (100 Hz) is not fast enough to guarantee the capsule dynamics are handled completely and so increasing this would have a direct impact on system performance. Assumption 2 can be overcome by performing techniques which consider the system dynamics. These will be explored in future work.

## 2.6 Conclusions

The present paper discussed a novel control technique for capsule levitation in magnetically driven capsule colonoscopy. This was motivated by the potential benefits of reduced friction, and obstacle avoidance, for improved locomotion in complex environments such as the colon. This is important as locomotion in this context is extremely challenging; devices are prone to becoming trapped in the soft folds of tissue and friction/drag can hinder progress. Although the magnetic system is inherently gentle, deforming the environment very little, the proposed control strategy improves this further and so may reduce clinical risks and patient discomfort. The control strategy is based on a gravity compensation approach which attains capsule levitation and fine control along the gravity direction, while also permitting capsule steering.

The asymptotic stability of the proposed technique was proved by employing the Lyapunov approach and supported in the experimental results from tests in an acrylic tube. These results show that, while levitating, we are able to handle slopes and, compared to previous solutions, reduce contact with the cavity from approximately 100 % to 19.5 %. On the base of these results, we can conclude that the control approach is a promising technique for general application in magnetically driven capsule colonoscopy.

In order to strengthen this inference, we also performed colonoscopy on a phantom simulator for colonoscopy training. These results show that we can perform colonoscopy by employing the levitation technique. Due to the encouraging results obtained in the colon phantom, we aim to confirm our findings in more realistic experimental settings (i.e. animal and cadaver models) in the near future. Moreover, we will investigate the possibility of using the solely levitation or any combination of it with other control techniques.

One of the current limitations of the present work is assuming that tether-environment interactions are negligible disturbances. In our future works, we will also investigate how to integrate these interactions in our control scheme, possibly by embedding real-time shape sensors inside the tether.

# Appendices



---

## Magnetic Actuation

In this appendix, we aim to discuss some basic concepts about magnetic actuation and define some of the variables used in the paper. We consider that both IPM and EPM can be modelled as dipoles and recall some of the implications already discussed in [21]. We show how to compute the magnetic force  $\tau_m(x, q)$  and how magnetism relates to the dynamics in (2.1).

Consider the pose of the EE of the robot being referred to as  $\chi \in \mathbb{R}^n$  and introduce the vector between EE position  $p_E$  (or, equivalently, EPM) and IPM position  $p_I$  as  $p = p_E - p_I$ . We consider the robot EE being the EPM. The force and torque between the two magnets can be expressed as

$$\tau_m = \begin{pmatrix} \frac{3\lambda}{\|p\|} (\hat{m}_E \hat{m}_I^T + \hat{m}_I \hat{m}_E^T + (\hat{m}_I^T Z \hat{m}_I) I) \hat{p} \\ \lambda \hat{m}_I \times D \hat{m}_E \end{pmatrix}$$

where

$$\lambda = \frac{\mu_0 \|m_I\| \|m_E\|}{4\pi \|p\|^3},$$

$m_I = \|m_I\| \hat{m}_I$  and  $m_E = \|m_E\| \hat{m}_E$  are the respective *magnetic moments* of IPM and EPM,  $\hat{p} = \frac{p}{\|p\|}$ ,  $Z = I - 5\hat{p}\hat{p}^T$  and  $D = 3\hat{p}\hat{p}^T - I$ ; here  $I \in \mathbb{R}^{3 \times 3}$  is referred to as the *identity matrix* and  $\|\cdot\|$  is the *Euclidean norm*.

As in [21], we consider the time derivative of  $\tau_m$

$$\begin{aligned}
\dot{\tau}_m &= \begin{pmatrix} \frac{\partial \tau}{\partial p} & \frac{\partial \tau}{\partial \hat{m}_E} & \frac{\partial \tau}{\partial \hat{m}_I} \end{pmatrix} \begin{pmatrix} \dot{p} \\ \dot{\hat{m}}_E \\ \dot{\hat{m}}_I \end{pmatrix} \\
&= \begin{pmatrix} \frac{\partial \tau}{\partial p} & \frac{\partial \tau}{\partial \hat{m}_E} & \frac{\partial \tau}{\partial \hat{m}_I} \end{pmatrix} \left[ \begin{pmatrix} \dot{p}_E \\ \dot{\hat{m}}_E \\ 0 \end{pmatrix} - \begin{pmatrix} \dot{p}_I \\ 0 \\ \dot{\hat{m}}_I \end{pmatrix} \right] \\
&= \begin{pmatrix} \frac{\partial \tau}{\partial p} & \frac{\partial \tau}{\partial \hat{m}_E} \end{pmatrix} \begin{pmatrix} \dot{p}_E \\ \dot{\hat{m}}_E \end{pmatrix} - \begin{pmatrix} \frac{\partial \tau}{\partial p} & \frac{\partial \tau}{\partial \hat{m}_I} \end{pmatrix} \begin{pmatrix} \dot{p}_I \\ \dot{\hat{m}}_I \end{pmatrix}.
\end{aligned}$$

As in [4], we can rewrite

$$\begin{pmatrix} \dot{p}_I \\ \dot{\hat{m}}_I \end{pmatrix} = \begin{pmatrix} I & 0_{3,3} \\ 0_{3,3} & (\hat{m}_I)_\times^T \end{pmatrix} \dot{x} = M_I \dot{x},$$

and

$$\begin{pmatrix} \dot{p}_E \\ \dot{\hat{m}}_E \end{pmatrix} = \begin{pmatrix} I & 0_{3,3} \\ 0_{3,3} & (\hat{m}_E)_\times^T \end{pmatrix} \dot{\chi} = M_E \dot{\chi},$$

where  $(\cdot)_\times : \mathbb{R}^3 \rightarrow \mathfrak{so}(3)$  is the *skew operator* and  $0_{i,k} \in \mathbb{R}^{i \times k}$  is referred to as the zero matrix.

By taking into account the robot jacobian matrix  $J$ , i.e. the matrix for which  $\dot{\chi} = J\dot{q}$  [25], we can define

$$J_q = \begin{pmatrix} \frac{\partial \tau}{\partial p} & \frac{\partial \tau}{\partial \hat{m}_E} \end{pmatrix} M_E J$$

and

$$J_x = - \begin{pmatrix} \frac{\partial \tau}{\partial p} & \frac{\partial \tau}{\partial \hat{m}_I} \end{pmatrix} M_I.$$

---

The force and torque derivative reads, as in (2.2), as

$$\dot{\tau}_m = J_x \dot{x} + J_q \dot{q}.$$

## Proofs of Lemmas and Theorems

In the following we provide the proofs of Lemma 2.1 and Theorem 2.3.

### Proof of Lemma 1

Consider the positive definite Lyapunov function

$$V(\tilde{x}, \dot{\tilde{x}}) = \frac{1}{2} \dot{\tilde{x}}^T B(x) \dot{\tilde{x}} + \frac{1}{2} \tilde{x}^T K_p \tilde{x}.$$

Being  $\dot{x}_d = 0$  by assumption,  $\dot{\tilde{x}}^T B(x) \dot{\tilde{x}}$  is the kinetic energy of the mechanical system;  $K_p$  is positive definite by definition. The time derivative of the chosen Lyapunov function reads as

$$\begin{aligned} \dot{V}(\tilde{x}, \dot{\tilde{x}}) &= \dot{x}^T B(x) \ddot{x} + \frac{1}{2} \dot{x}^T \dot{B}(x) \dot{x} + \tilde{x}^T K_p \dot{\tilde{x}} \\ &= \dot{x}^T (\tau - C(x, \dot{x}) \dot{x} - G(x)) + \frac{1}{2} \dot{x}^T \dot{B}(x) \dot{x} \\ &\quad + \tilde{x}^T K_p \dot{x} \\ &= -\dot{x}^T K_d \dot{x} + \frac{1}{2} \dot{x}^T (\dot{B}(x) - 2C(x, \dot{x})) \dot{x} \\ &= -\dot{x}^T K_d \dot{x}. \\ &= -\dot{\tilde{x}}^T K_d \dot{\tilde{x}}. \end{aligned}$$

The last two inferences hold for the *work-energy theorem* [25], which implies  $\dot{x}^T (\dot{B}(x) - 2C(x, \dot{x})) \dot{x} = 0$ , and the fact that  $\dot{x}_d = 0$ . Being  $K_d$  positive definite, by design,  $\dot{V}(\tilde{x}, \dot{\tilde{x}}) \leq 0$  and the system is, at least, marginally stable.

One can prove the asymptotic stability by applying the La Salle's theorem. In fact, the set  $\Omega = \{(\tilde{x}, \dot{\tilde{x}}) | \dot{V}(\tilde{x}, \dot{\tilde{x}}) = 0\} = \{(\tilde{x}, 0)\}$  is closed and  $V(\tilde{x}, \dot{\tilde{x}})$  is radially unlimited. Moreover, being  $\dot{x}_d = 0$  by choice,  $\dot{\tilde{x}} = 0$  leads to  $\dot{x} = 0$ . By substitution in (2.1), being

---

$\tau = \tau_d$  by assumption, we obtain

$$K_p \tilde{x} = 0,$$

thus, the largest invariant set is  $M = \{(\tilde{x}, \dot{\tilde{x}}) | K_p \tilde{x} = 0\}$ . Being  $K_p$  positive definite, by definition,  $M = \{(\tilde{x}, \dot{\tilde{x}}) = (0, 0)\}$  and the equilibrium is asymptotically stable.

### Proof of Theorem 1

Consider the positive definite Lyapunov function

$$W(\tilde{x}, \dot{\tilde{x}}, \tilde{\tau}) = V(\tilde{x}, \dot{\tilde{x}}) + \frac{1}{2} \tilde{\tau}^T \tilde{\tau},$$

where  $V(\tilde{x}, \dot{\tilde{x}})$  is the Lyapunov function defined in the proof of Lemma 2.1. The time derivative of the chosen Lyapunov function is

$$\begin{aligned} \dot{W}(\tilde{x}, \dot{\tilde{x}}, \tilde{\tau}) &= \dot{x}^T B(x) \ddot{x} + \frac{1}{2} \dot{x}^T \dot{B}(x) \dot{x} + \tilde{x}^T K_p \dot{\tilde{x}} + \tilde{\tau}^T \dot{\tilde{\tau}} \\ &= \dot{x}^T (\tau - C(x, \dot{x}) \dot{x} - G(x)) + \frac{1}{2} \dot{x}^T \dot{B}(x) \dot{x} \\ &\quad + \tilde{x}^T K_p \dot{x} - \tilde{\tau}^T (K \tilde{\tau} - \dot{x}) \\ &= \dot{x}^T (\tau_d - \tilde{\tau} - C(x, \dot{x}) \dot{x} - G(x)) + \frac{1}{2} \dot{x}^T \dot{B}(x) \dot{x} \\ &\quad + \tilde{x}^T K_p \dot{x} - \tilde{\tau}^T (K \tilde{\tau} - \dot{x}) \\ &= \dot{x}^T (\tau_d - C(x, \dot{x}) \dot{x} - G(x)) \\ &\quad + \frac{1}{2} \dot{x}^T \dot{B}(x) \dot{x} + \tilde{x}^T K_p \dot{x} - \tilde{\tau}^T (K \tilde{\tau} - \dot{x}) \\ &\quad - \dot{x}^T \tilde{\tau} \\ &= -\dot{x}^T K_d \dot{x} + \frac{1}{2} \dot{x}^T (\dot{B}(x) - 2C(x, \dot{x})) \dot{x} \\ &\quad - \tilde{\tau}^T K \tilde{\tau} \\ &= \dot{V}(\tilde{x}, \dot{\tilde{x}}) - \tilde{\tau}^T K \tilde{\tau}, \end{aligned}$$

which is negative semidefinite. The La Salle's theorem can be applied, as in Lemma 2.1, to show the asymptotic stability of the controlled dynamics. By following the steps of the proof of Lemma 2.1, one can show that the largest invariant set is found with the same procedure:  $N = \{(\tilde{x}, \dot{\tilde{x}}, \tilde{\tau}) | K_p \tilde{x} = 0\}$ . Therefore, the asymptotic stability is proved.

---

## Bibliography

- [1] A. Arezzo, A. Menciassi, P. Valdastri, G. Ciuti, G. Lucarini, M. Salerno, C. Di Natali, M. Verra, P. Dario, and M. Morino, “Experimental assessment of a novel robotically-driven endoscopic capsule compared to traditional colonoscopy,” *Digestive and Liver Disease*, vol. 45, no. 8, pp. 657–662, 2013.
- [2] P. Valdastri, C. Quaglia, E. Susilo, A. Menciassi, P. Dario, C. Ho, G. Anhoeck, and M. Schurr, “Wireless therapeutic endoscopic capsule: in vivo experiment,” *Endoscopy*, vol. 40, pp. 979–982, dec 2008.
- [3] P. Valdastri, G. Ciuti, A. Verbeni, A. Menciassi, P. Dario, A. Arezzo, and M. Morino, “Magnetic air capsule robotic system: proof of concept of a novel approach for painless colonoscopy,” *Surgical Endoscopy*, vol. 26, no. 5, pp. 1238–1246, 2012.
- [4] A. W. Mahoney and J. J. Abbott, “Five-degree-of-freedom manipulation of an untethered magnetic device in fluid using a single permanent magnet with application in stomach capsule endoscopy,” *The International Journal of Robotics Research*, vol. 35, no. 1-3, pp. 129–147, 2016.
- [5] C. Chautems and B. J. Nelson, “The tethered magnet: Force and 5-DOF pose control for cardiac ablation,” *Proceedings - IEEE International Conference on Robotics and Automation*, pp. 4837–4842, 2017.
- [6] M. N. Faddis, W. Blume, J. Finney, A. Hall, J. Rauch, J. Sell, K. T. Bae, M. Talcott, and B. Lindsay, “Novel, magnetically guided catheter for endocardial mapping and radiofrequency catheter ablation,” *Circulation*, vol. 106, no. 23, pp. 2980–2985, 2002.
- [7] S. Toggweiler, J. Leipsic, R. K. Binder, M. Freeman, M. Barbanti, R. H. Heijmen, D. A. Wood, and J. G. Webb, “Management of vascular access in transcatheter aortic valve replacement: Part 2: Vascular complications,” *JACC: Cardiovascular Interventions*, vol. 6, no. 8, pp. 767–776, 2013.
- [8] S. K. Hilai, W. J. Michelsen, J. Driller, and E. Leonard, “Magnetically guided de-

- vices for vascular exploration and treatment: Laboratory and clinical investigations,” *Radiology*, vol. 113, no. 3, pp. 529–540, 1974.
- [9] S. Ernst, F. Ouyang, C. Linder, K. Hertting, F. Stahl, J. Chun, H. Hachiya, D. Bän-sch, M. Antz, and K. H. Kuck, “Initial Experience with Remote Catheter Ablation Using a Novel Magnetic Navigation System: Magnetic Remote Catheter Ablation,” *Circulation*, vol. 109, no. 12, pp. 1472–1475, 2004.
- [10] J. Sikorski, I. Dawson, A. Denasi, E. E. Hekman, and S. Misra, “Introducing Big-Mag - A novel system for 3D magnetic actuation of flexible surgical manipulators,” *Proceedings - IEEE International Conference on Robotics and Automation*, pp. 3594–3599, 2017.
- [11] W. J. Casarella, J. Driller, and S. K. Hilal, “The magnetically guided bronchial catheter of modified pod design: A new approach to selective bronchoscopy,” *Radiology*, vol. 93, no. 4, pp. 930–932, 1969.
- [12] J. Edelmann, A. J. Petruska, and B. J. Nelson, “Magnetic control of continuum devices,” *International Journal of Robotics Research*, vol. 36, no. 1, pp. 68–85, 2017.
- [13] J. Edelmann, A. J. Petruska, and B. J. Nelson, “Estimation-Based Control of a Magnetic Endoscope without Device Localization,” *Journal of Medical Robotics Research*, vol. 03, p. 1850002, Mar 2018.
- [14] A. J. Petruska and B. J. Nelson, “Minimum Bounds on the Number of Electromagnets Required for Remote Magnetic Manipulation,” *IEEE Transactions on Robotics*, vol. 31, no. 3, pp. 714–722, 2015.
- [15] C. Chautems, A. Tonazzini, D. Floreano, and B. J. Nelson, “A variable stiffness catheter controlled with an external magnetic field,” *2017 IEEE/RSJ International Conference on Intelligent Robots and Systems (IROS)*, pp. 181–186, 2017.
- [16] T. Greigarn, R. Jackson, T. Liu, and M. C. Çavuşoğlu, “Experimental validation of the pseudo-rigid-body model of the MRI-actuated catheter,” in *2017 IEEE In-*

- ternational Conference on Robotics and Automation (ICRA)*, pp. 3600–3605, May 2017.
- [17] S. Jeon, A. K. Hoshidar, K. Kim, S. Lee, E. Kim, S. Lee, J. Kim, B. J. Nelson, H. Cha, B. Yi, and H. Choi, “A magnetically controlled soft microrobot steering a guidewire in a three-dimensional phantom vascular network,” *Soft Robotics*, vol. 0, no. 0, 0. PMID: 30312145.
- [18] S. Yim and M. Sitti, “Design and Rolling Locomotion of a Magnetically Actuated Soft Capsule Endoscope,” *IEEE Transactions on Robotics*, vol. 28, pp. 183–194, Feb 2012.
- [19] P. Ryan and E. Diller, “Magnetic Actuation for Full Dexterity Microrobotic Control Using Rotating Permanent Magnets,” *IEEE Transactions on Robotics*, vol. 33, no. 6, pp. 1398–1409, 2017.
- [20] G. Ciuti, P. Valdastri, A. Menciassi, and P. Dario, “Robotic magnetic steering and locomotion of capsule endoscope for diagnostic and surgical endoluminal procedures,” *Robotica*, vol. 28, p. 199, Mar 2010.
- [21] A. Z. Taddese, P. R. Slawinski, K. L. Obstein, and P. Valdastri, “Nonholonomic closed-loop velocity control of a soft-tethered magnetic capsule endoscope,” in *2016 IEEE/RSJ International Conference on Intelligent Robots and Systems (IROS)*, pp. 1139–1144, IEEE, Oct 2016.
- [22] M. Miyasaka and P. Berkelman, “Magnetic levitation with unlimited omnidirectional rotation range,” *Mechatronics*, vol. 24, no. 3, pp. 252–264, 2014.
- [23] H. K. Khalil, *Nonlinear systems*. Macmillan Pub. Co., 1992.
- [24] A. Z. Taddese, P. R. Slawinski, M. Pirodda, E. De Momi, K. L. Obstein, and P. Valdastri, “Enhanced real-time pose estimation for closed-loop robotic manipulation of magnetically actuated capsule endoscopes,” *The International Journal of Robotics Research*, vol. 37, no. 8, pp. 890–911, 2018.

- [25] B. Siciliano, L. Sciavicco, L. Villani, and G. Oriolo, *Robotics: Modelling, Planning and Control*. Springer Publishing Company, Incorporated, 1st ed., 2008.
- [26] A. Alazmani, A. Hood, D. Jayne, A. Neville, and P. Culmer, “Quantitative assessment of colorectal morphology: Implications for robotic colonoscopy,” *Medical Engineering & Physics*, vol. 38, no. 2, pp. 148 – 154, 2016.
- [27] A. J. Petruska and J. J. Abbott, “Optimal permanent-magnet geometries for dipole field approximation,” *IEEE Transactions on Magnetics*, vol. 49, pp. 811–819, Feb 2013.

## Chapter 3

# Collaborative Magnetic Manipulation

**Chapter source:** G. Pittiglio, J. H. Chandler, M. Richter, V. K. Venkiteswaran, S. Misra and P. Valdastrì, "Dual-Arm Control for Enhanced Magnetic Manipulation," 2020 IEEE/RSJ International Conference on Intelligent Robots and Systems (IROS), 2020, pp. 7211-7218, doi: 10.1109/IROS45743.2020.9341250.

## Abstract

Magnetically actuated soft robots have recently been identified for application in medicine, due to their potential to perform minimally invasive exploration of human cavities. Magnetic solutions permit further miniaturization when compared to other actuation techniques, without loss in functionalities. Our long-term goal is to propose a novel actuation method for magnetically actuated soft robots, based on dual-arm collaborative magnetic manipulation. A fundamental step in this direction is to show that this actuation method is capable of controlling up to 8 coincident, independent Degrees of Freedom (DOFs). In present paper, we prove this concept by measuring the independent wrench components on a second pair of static permanent magnets, by means of a high resolution 6-axis load cell. The experiments show dominant activation of the desired DOFs, with mean cross-activation error of the undesired DOFs ranging from 2% to 10%.

## 3.1 Introduction

The last few decades have seen a significant growth of *minimally invasive procedures for diagnosis and treatment*. This generally equates to reduced pain, morbidity and recovery time. However, the application of minimally invasive techniques poses several challenges which have led to focused investigation of multi-Degrees of Freedom (DOFs), flexible structures: *continuum robots* [1; 2; 3]. These manipulators are characterised by several DOFs and low stiffness, which facilitates the safe exploration of tortuous environments.

Continuum robots have proven effective in several scenarios, and many diverse actuation mechanisms have been proposed, for example: *concentric tubes* [4]; *(multi-)backbone-based*

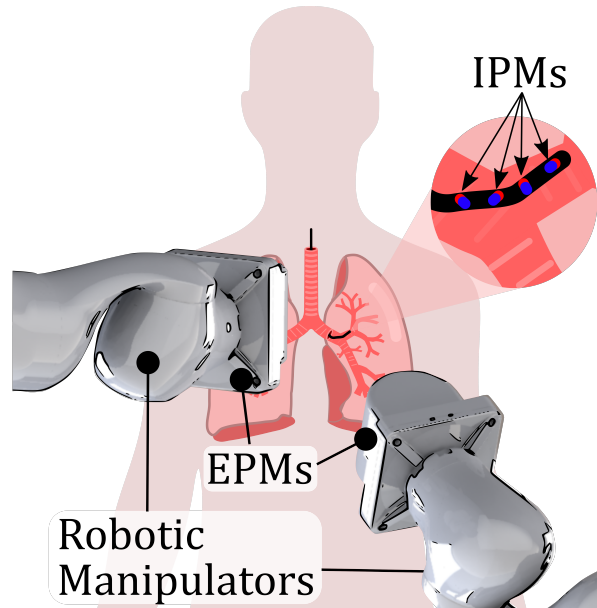


Figure 3.1: Example of application of multi-DOFs magnetic manipulation in endoscopy: bronchoscopy.

designs [5; 6]; *tendon driven* structures [7; 8; 9]; and soft *pneumatic* [10]; and *hydraulic* [11] implementations, among others. In general, these approaches comply with the requirements of minimally invasive procedures. However, they require physical coupling between the actuation unit and the continuum structure. This typically necessitates an increase in their size when more DOFs are required. For this reason, *magnetic actuation* has been recently proposed for actuating continuum robots [12; 13], as an improvement to controlling single magnet-based structures [14; 15; 16]. Moreover, this concept has been further investigated also for application to soft magnetized platforms [17].

In the case of magnetically actuated robots, reducing the volume of magnetic material, as necessary for miniaturization, results in a loss of magnetic wrench for a given field. However, this can be directly compensated through dimensioning of the actuation system. Specifically, more force/torque can be achieved by using more powerful actuation platforms, without a direct increase in the robot's dimensions, e.g. [18]. Several diverse actuation systems have been proposed for magnetic actuation, which can be subdivided into *coil-based* [18; 19; 20; 15; 21; 12], *rotating permanent magnets* [22], *robotically actuated coils* [23] and *robotically actuated permanent magnets* [24; 14]. The main limitation of the former two is the limited workspace and poor scalability, while their robotically

actuated counterpart [24; 23] have, generally, larger manipulability workspace with only limitation to the specific robot’s capabilities. However, using permanent magnets as alternative to coils facilitates energy reduction and possible electromagnetic interference.

In [21], the authors show that a set of 8 coils is able to manipulate 8 independent DOFs. This is the maximum number of DOFs that can be physically controlled in the same point of a magnetic workspace. Here, we aim to prove that same capabilities can be achieved with a minimal number of magnetic sources, i.e. 2, and that we can employ permanent magnets instead of coils. These two fundamental points facilitate cost reduction and enlarge the (magnetic) manipulability workspace, which is fundamental in the application to medical robotics. However, the proposed approach could also be applied to robotically actuated coil systems [23].

Recently, robotically manipulated single External Permanent Magnet (EPM)-based approaches have been shown to be effective in overcoming the challenges related to magnetic manipulation via non-homogeneous magnetic fields [25; 24]. Specifically, the difficulties in handling non-linear relationship between actuation variables (EPM-Internal Permanent Magnet (IPM) relative pose) and resulting wrench. However, the use of a single magnetic source limits the number of controllable DOFs to 5, given the dipole symmetries [26]. In this paper, we investigate the minimum number of magnetic sources able to achieve maximum manipulability (8 DOFs) in a single point of the workspace: 2 robotically manipulated EPMS.

The problem of magnetic manipulation with robotically actuated magnetic sources is introduced in Section 3.2 and, on the basis of this definition, we formulate the concept of *magnetic manipulability* in Section 3.3. Possible independent poses of the EPMS are analysed in Section 3.4 and experimentally validated in Section 3.5. We report our main conclusions and future directions in Section 5.8.

## 3.2 Problem Definition

In the present section, we discuss multi-DOFs manipulation, based on magnetic wrench control [25; 24]. In particular, we consider that we can manipulate  $N$  independent IPMs, by robotically controlling the pose of  $M$  EPMS, independently.

Consider the relative position between the  $i$ -th EPM ( $p_{E_i}$ ) and the  $j$ -th IPM ( $p_{I_j}$ ),  $p_{ij} = p_{E_i} - p_{I_j} \in \mathbb{R}^3$  and between the  $j$ -th and the  $k$ -th IPMs  $d_{jk} = p_{I_k} - p_{I_j} \in \mathbb{R}^3$ , and introduce the relative *magnetic wrench* [24]

$$\begin{aligned}
 w_{ij} &= \begin{pmatrix} f_{ij} \\ \tau_{ij} \end{pmatrix} \\
 &= \begin{pmatrix} \frac{3C_{ij}}{\|p_{ij}\|^4} (\hat{m}_{E_i} \hat{m}_{I_j}^T + \hat{m}_{I_j} \hat{m}_{E_i}^T + (\hat{m}_{I_j}^T Z_{ij} \hat{m}_{E_i}) I) \hat{p}_{ij} \\ \frac{C_{ij}}{\|p_{ij}\|^3} \hat{m}_{I_j} \times D_{ij} \hat{m}_{E_i} \end{pmatrix} \\
 &\quad + \sum_{k=1}^N \\
 &\quad \begin{pmatrix} \frac{3C_{jk}}{\|d_{jk}\|^4} (\hat{m}_{I_k} \hat{m}_{I_j}^T + \hat{m}_{I_j} \hat{m}_{I_k}^T + (\hat{m}_{I_j}^T \mathcal{Z}_{jk} \hat{m}_{I_k}) I) \hat{d}_{jk} \\ \frac{C_{jk}}{\|d_{jk}\|^3} \hat{m}_{I_j} \times \mathcal{D}_{jk} \hat{m}_{I_k} \end{pmatrix}
 \end{aligned} \tag{3.1}$$

where  $C_{ij} = \frac{\mu_0 \|m_{I_j}\| \|m_{E_i}\|}{4\pi}$ ,  $C_{jk} = \frac{\mu_0 \|m_{I_j}\| \|m_{I_k}\|}{4\pi}$ , with  $m_{I_j}, m_{I_k}, m_{E_i} \in \mathbb{R}^3$  *magnetic moments* of the respective IPMs and EPM;  $\mu_0 = 4\pi 10^{-7} \frac{N}{A^2}$  permeability of vacuum,  $Z_{ij} = I - 5\hat{p}_{ij}\hat{p}_{ij}^T$ ,  $D_{ij} = 3\hat{p}_{ij}\hat{p}_{ij}^T - I$ ,  $\mathcal{Z}_{jk} = I - 5\hat{d}_{jk}\hat{d}_{jk}^T$  and  $\mathcal{D}_{jk} = 3\hat{d}_{jk}\hat{d}_{jk}^T - I$ . We refer to  $I \in \mathbb{R}^{3 \times 3}$  as the *identity matrix*,  $\|\cdot\|$  as the *Euclidean norm* and  $\hat{\cdot} = \frac{\cdot}{\|\cdot\|}$ . Here,  $f_{ij}$  and  $\tau_{ij}$  are the force and torque, respectively. The wrench in (3.1) is found by applying the *superposition principle* under the assumption that the IPMs and EPMS involved can be modeled as *dipoles*, i.e. when they are *far enough* from each other, relative to their size [27]; this is a common approach in magnetic manipulation [26].

Compared to the case of coils [21], we can notice that (3.1) is highly nonlinear with respect to the control variables  $p_{E_i}$  and  $m_{E_i}$ . In fact, when using a system of multiple coils, these can be all orientated towards the center of the workspace and a linear relationship

between the current and generated field can be obtained - within a "small-enough" area of the workspace. In our case, these simplifications do not apply and deeper analysis is required.

To investigate the actuation capabilities of multiple EPMS, along the lines of [25; 24], we define the differential of the wrench as

$$\begin{aligned}
\delta w_{ij} &= \begin{pmatrix} \frac{\partial w_{ij}}{\partial p_{ij}} & \frac{\partial w_{ij}}{\partial \hat{m}_{I_j}} \end{pmatrix} \begin{pmatrix} \delta p_{I_j} \\ \delta \hat{m}_{I_j} \end{pmatrix} + \begin{pmatrix} \frac{\partial w_{ij}}{\partial p_{ij}} & \frac{\partial w_{ij}}{\partial \hat{m}_{E_i}} \end{pmatrix} \begin{pmatrix} \delta p_{E_i} \\ \delta \hat{m}_{E_i} \end{pmatrix} \\
&+ \sum_{\substack{k=1 \\ k \neq j}}^N \begin{pmatrix} \frac{\partial w_{ij}}{\partial d_{jk}} & \frac{\partial w_{ij}}{\partial \hat{m}_{I_k}} \end{pmatrix} \begin{pmatrix} \delta p_{I_k} \\ \delta \hat{m}_{I_k} \end{pmatrix} \\
&= \begin{pmatrix} \frac{\partial w_{ij}}{\partial p_{ij}} & \frac{\partial w_{ij}}{\partial \hat{m}_{I_j}} \end{pmatrix} \begin{pmatrix} I & 0_{3,3} \\ 0_{3,3} & (\hat{m}_{I_j})_{\times}^T \end{pmatrix} \delta x_j \\
&+ \begin{pmatrix} \frac{\partial w_{ij}}{\partial p_{ij}} & \frac{\partial w_{ij}}{\partial \hat{m}_{E_i}} \end{pmatrix} \begin{pmatrix} I & 0_{3,3} \\ 0_{3,3} & (\hat{m}_{E_i})_{\times}^T \end{pmatrix} \delta q_i \\
&+ \sum_{\substack{k=1 \\ k \neq j}}^N \begin{pmatrix} \frac{\partial w_{ij}}{\partial d_{jk}} & \frac{\partial w_{ij}}{\partial \hat{m}_{I_k}} \end{pmatrix} \begin{pmatrix} I & 0_{3,3} \\ 0_{3,3} & (\hat{m}_{I_k})_{\times}^T \end{pmatrix} \delta x_k \\
&= J_{x_{ij}} \delta x + J_{q_{ij}} \delta q_i, \tag{3.2}
\end{aligned}$$

with  $0_{k,l} \in \mathbb{R}^{k \times l}$  zero matrix,  $(\cdot)_{\times} : \mathbb{R}^3 \rightarrow \mathfrak{so}(3)$  is the skew operator and  $x = (x_1^T \ x_2^T \ \dots \ x_N^T)^T$ .

We refer to  $x_j \in \mathbb{R}^6$ ,  $j = 1, 2, \dots, N$  as the representation of the  $j$ -th IPM pose (i.e. position and Euler angles) and to  $q_j$  as the representation of the  $j$ -th EPM pose.

We will focus on the manipulation of multiple DOFs in a point  $p_I = p_{I_k} = p_{I_l} \ \forall \ i, l$ , that does not vary with time, i.e.  $\delta p_{I_j} = \delta m_{I_j} = 0 \ \forall \ j$ . We consider this scenario for two reasons: first, our aim is to focus on the manipulability properties in a fixed point within the workspace, with no constraints on the specific target point. Secondly, having multiple IPMs at the same point within the workspace represents the worst case scenario. In fact, the further the IPMs are apart, the more they behave as independent magnets (5 DOFs each). Moreover, under these assumptions, the interaction between

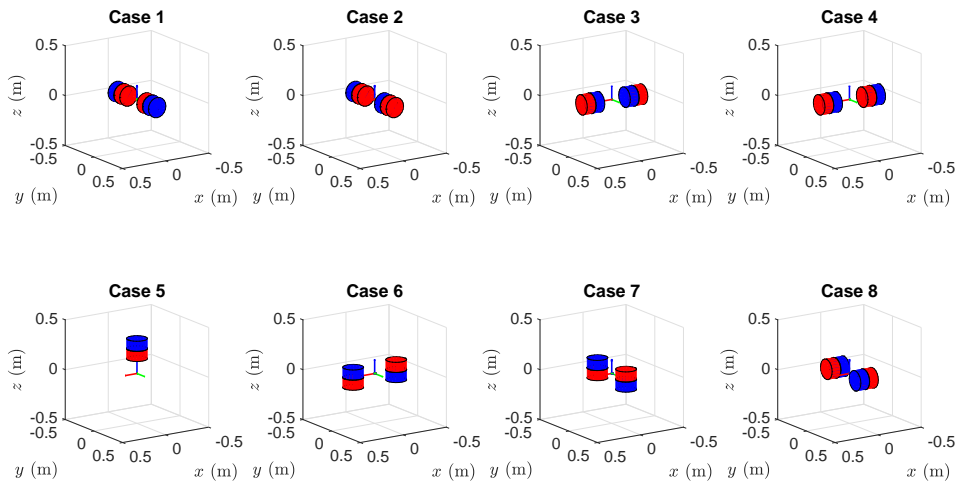


Figure 3.2: EPMs poses for independent DOFs control; cases are shown with EPM-IPM center to center distance of 0.25 m.

IPMs can be neglected, which does not change the number of DOFs, when the wrench is fully controllable from the input  $q = (q_1^T \ q_2^T \ \cdots \ q_M^T)^T$  [28]. This is discussed in the next section.

The variation of wrench can thus be directly related to EPMs motion (or actuation) only, as

$$\delta w = J_q \delta q, \quad (3.3)$$

where  $[J_q]_{ij} = J_{q_{ij}} \in \mathbb{R}^{6 \times 6}$  is the  $i, j$  block of  $J_q$  and

$$w = \begin{pmatrix} \sum_{i=1}^M w_{1i} \\ \sum_{i=1}^M w_{2i} \\ \vdots \\ \sum_{i=1}^M w_{Ni} \end{pmatrix}.$$

### 3.3 Definition of Magnetic Manipulability

We intend (magnetic) *manipulability* to be the measure of the number of (magnetic) DOFs that can be (magnetically) manipulated by a (magnetic) actuation system. This

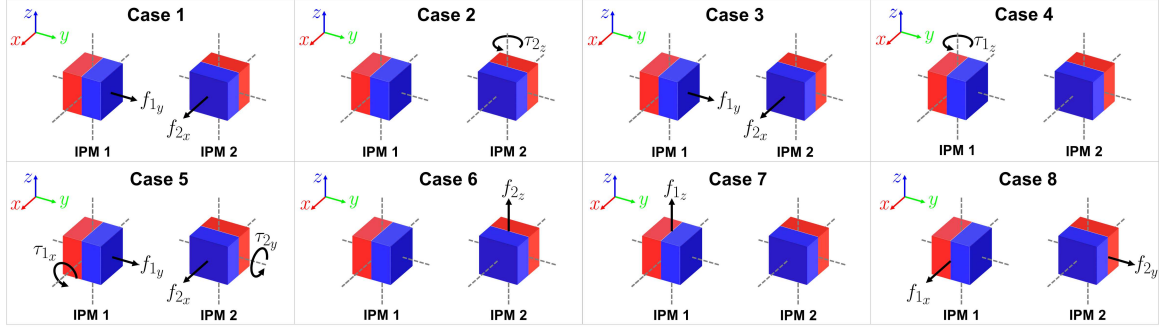


Figure 3.3: Example of orthogonal IPMs and directions of the wrench applied for each of the cases of Fig. 3.2.

means that, given a set of inputs ( $q$ ), we aim to measure the number of variables ( $w$ ) that can be independently actuated.

In the following, we prove that with 2 EPMS ( $M = 2$ ) we can control 8 DOFs of 2 orthogonal IPMs ( $N = 2$ ) in the same point of the workspace. First, we need to prove that the magnetic DOFs of 2 orthogonal IPMs are 8 in the same point in space, as in [21]. This is straightforward since, in the same point, they experience the same magnetic field ( $B$ ) and magnetic field jacobian ( $dB = \frac{\partial B}{\partial p}$ ). Therefore,

$$\begin{aligned}
 w_{ij} &= \begin{pmatrix} dB \ m_{I_j} \\ (m_{I_j})_{\times} B \end{pmatrix} \\
 &= \left( \begin{array}{cccc|c} m_{I_{j_1}} & m_{I_{j_2}} & m_{I_{j_3}} & 0 & 0 \\ 0 & m_{I_{j_1}} & 0 & m_{I_{j_2}} & m_{I_{j_3}} \\ -m_{I_{j_3}} & 0 & m_{I_{j_1}} & -m_{I_{j_3}} & m_{I_{j_2}} \\ \hline & & 0_{3,5} & & (m_{I_j})_{\times} \end{array} \right) \begin{pmatrix} \frac{\partial B_1}{\partial e_1} \\ \frac{\partial B_1}{\partial e_2} \\ \frac{\partial B_1}{\partial e_3} \\ \frac{\partial B_2}{\partial e_2} \\ \frac{\partial B_2}{\partial e_3} \\ B \end{pmatrix} \\
 &= S_j U.
 \end{aligned} \tag{3.4}$$

Here,  $e_i \in \mathbb{R}^3$  is the  $i$ -th element of the orthonormal basis of  $\mathbb{R}^3$ .

Intrinsically,  $U$  depends on the pose of all the EPMS involved. We can write the relation-

ship in (3.4) as

$$w = SU, \quad (3.5)$$

and (3.3), being  $m_{I_j}$  assumed constant  $\forall j$ , as

$$\delta w = S \frac{\partial U}{\partial q} \delta q = J_q \delta q,$$

with  $S = (S_1^T \ S_2^T \ \dots \ S_N^T)^T$ . Therefore,  $S \frac{\partial U}{\partial q} \equiv J_q$  and, as standard approach in robotics [29], the number of DOFs controllable from  $\delta q$  is  $\text{rank}(J_q)$ .

Since  $\text{rank}\left(S \frac{\partial U}{\partial q}\right) \leq \min\left(\text{rank}(S), \text{rank}\left(\frac{\partial U}{\partial q}\right)\right)$  and  $\text{rank}(S) \leq 8$ , the maximum number of DOFs we can control in a point is 8. It is known that, for any  $j$ ,  $\text{rank}(S_j) = 5$ . Moreover, one can notice that  $\text{rank}(S) = 8$ , if  $S = (S_1^T \ S_2^T)^T$  and  $m_{I_1} \times m_{I_2} \neq 0$  (i.e. 2 IPMs are not parallel). Specifically, maximum manipulability is obtained with 2 orthogonal IPMs.

We can assume, from here on, that we select the two IPMs to be orthogonal and, thus,  $\text{rank}(S) = 8$ . In this case,

$$\text{rank}\left(S \frac{\partial U}{\partial q}\right) = \text{rank}\left(\frac{\partial U}{\partial q}\right) = \text{rank}(J_q),$$

thus, independently of the IPMs, we can investigate magnetic manipulability by analysing  $J_q$  or, equivalently  $\frac{\partial U}{\partial q}$ . However, the analysis of these matrices has two main disadvantages: they are nonlinear with respect to the control variables ( $q$ ) and they map variations in the input ( $\delta q$ ) onto the output ( $\delta w$ ). Therefore, any solution is local and difficult to quantify. For this reason, we describe a more suitable approach to identify the DOFs, in the next section.

In a real scenario, we cannot guarantee the IPMs to be always orthogonal, when organized in a serial structure such as a continuum robot. This means that manipulability, as for general robotic systems [29], is a local property and there exist conditions of singularity. This can be physically avoided by mechanical constraints or considered in the controller design. For the scope of the presented work, we analyse IPMs in a non-singular scenario;

avoiding dependence on their local configurations. However, we expect that there will exist situations for which some degree of controllability may be lost, in real applications.

### 3.4 Degrees of Freedom Analysis

In the following, we will be considering the actuation of  $N = 2$  *orthogonal* IPMs with  $M = 2$  *independently actuated* EPMS. Increasing the number of EPMS would not have a real effect on the number of DOFs we can control in a point, due to the properties of the magnetic field:  $\text{rank}(S) \leq 8$  (see previous section).

Finding 8 independent DOFs is equivalent to finding 8 poses of the EPMS that led to 8 orthogonal directions of the wrench  $w$  onto the IPMs. This can be expressed as searching for the set  $Q = \{q(T), T = 1, 2, \dots, 8\}$  such that

$$\text{rank}(w(1) \cdots w(8)) = \text{rank}(S(U(1) \cdots U(8))) = 8.$$

Since, in this case,  $\text{rank}(S) = 8$ ,

$$\text{rank}(S(U(1) \cdots U(8))) = \text{rank}(U(1) \cdots U(8)).$$

Thus, we need to find 8 poses for which we obtain 8 independent  $U(T)$ ,  $T = 1, 2, \dots, 8$ . Due to the nonlinearities of the problem, solving (3.4) or (3.1) with respect to  $q$  is not trivial. Therefore, we opted for a direct analysis of primitive poses, in terms of effects on the magnetic field, as detailed below. Some of the analysed poses are known to be suboptimal, due to the workspace limitations of the actuating robotic system: 2 LBR iiwa 14 (KUKA, Germany). However, they show independent activation of each field component. These poses are reported in Fig. 3.2 and their effect on the wrench applied to 2 orthogonal IPMs reported in Fig. 3.3. Specifically, in Fig. 3.3, we show the force and torque that are activated for each case of Fig. 3.2. To underline the independent DOFs activation, we schematically represent the components of field and differentials in Table 3.1, according to the dipole model. These represent the directions of the 8 linearly

Table 3.1: Field and Differential components in the 8 cases, normalized to their maximum value.

	Case 1	Case 2	Case 3	Case 4	Case 5	Case 6	Case 7	Case 8
$\frac{\partial B_1}{\partial e_1}$	$\frac{1}{2}$		-1		$\frac{1}{4}$			
$\frac{\partial B_1}{\partial e_2}$								1
$\frac{\partial B_1}{\partial e_3}$						1		
$\frac{\partial B_2}{\partial e_2}$	-1		$\frac{1}{2}$		$\frac{1}{4}$			
$\frac{\partial B_2}{\partial e_3}$							1	
$B_1$				1				
$B_2$		1						
$B_3$					1			

independent vectors that led to the analysed DOFs. In particular, we normalized each component to its maximum value over the 8 cases and obtain the reported scale-free values. This eliminates any dependency between field and differentials strength, EPM-IPM distance and their respective size, and permits comparison between magnetic field and differentials, which are inherently different physical quantities. The strength of the actuation, being case-specific, could be changed by designing the geometric parameters of the magnets or controlled through EPM-IPM distance.

**Poses for Field Solutions** The last 3 components of  $U$  (see (3.4)) are related to the magnetic field  $B$ . In order to have 3 orthogonal vectors  $U(T)$ , for different times  $T$ , we look for configurations where the magnets are aligned (case 2, 4, 5 in Fig. 3.2). In this case, by aligning the EPMS with each of the main axis, we obtain  $\hat{B}(2) = e_2$ ,  $\hat{B}(4) = e_1$  and  $\hat{B}(5) = e_3$ , thus 3 independent components of  $U$ . Due to physical limitations of the robots' workspace, reaching the bottom of the IPMs was not possible. Therefore, we propose the control of  $U(5)$  by only using one EPM. This, inherently, generates differential components.

**Poses for Differentials Solutions** To obtain independent components of  $U$  related to the differentials of the field, we consider solutions with no field components. This is achieved by positioning the EPMS in opposite directions (case 1, 3, 6, 7, 8). In both cases

1 and 3, we obtain differentials  $\frac{\partial B_1}{\partial e_1}$  and  $\frac{\partial B_2}{\partial e_2}$ . In the cases 6, 7, 8, we obtain only the component  $\frac{\partial B_1}{\partial e_3}$ ,  $\frac{\partial B_2}{\partial e_3}$  and  $\frac{\partial B_1}{\partial e_2}$ , respectively.

## 3.5 Experimental Analysis

Validation of the proposed inferences, was performed through a series of experiments, aimed at proving the 8 DOFs manipulation capabilities. In particular, we tested 8 configurations of the EPMS for which we can control, independently, the 8 components of the field  $U$ , defined in Section 3.3. This proves the results in previous section, as reported in Table 3.1.

Each experiment was performed by placing a 6-axis load cell (Nano17 Titanium, ATI, USA) between 2 robotic arms (LBR iiwa 14, KUKA, Germany); each manipulating one of the actuating EPMS (Cylindrical permanent magnet with a diameter and length of 101.6 mm and an axial magnetization of 970.1 Am<sup>2</sup> (N52)), as shown in Fig. 3.4. Each experiment was repeated twice, in order to emulate the presence of more than 5 DOFs in the same point of the workspace. To realize this arrangement experimentally, we captured the load cell data during EPMS manipulation first with an IPM (Cubic permanent magnet with length of 12.6 mm and an axial magnetization of 2.1 Am<sup>2</sup> (N42)) mounted along the global  $y$  axis (Config. 1, Fig. 3.4), and subsequently rotated the IPM to align with the  $x$  axis (Config. 2, Fig. 3.4) and repeated the EPMS manipulation sequence, detailed in Fig. 3.2.

For each of the *cases* reported in Fig. 3.2 and Table 3.1, we performed an independent experiment, in order to better visualize the behaviour of the field<sup>1</sup>, specifically, in its steady final configuration. The two robotic arms were controlled to the each pose reported in Fig. 3.2, synchronously, from an initial *zero-field pose*. This initial pose was found as a trade-off between reachable workspace, i.e. the one each end-pose would be reached from, and minimum field strength; to eliminate residual magnetic coupling, the load cell was de-biased in this initial configuration. A detailed video of the performed experiments

<sup>1</sup>We refer to "field" as the vector field  $U$ , introduced in (3.4), to simplify the dissertation.

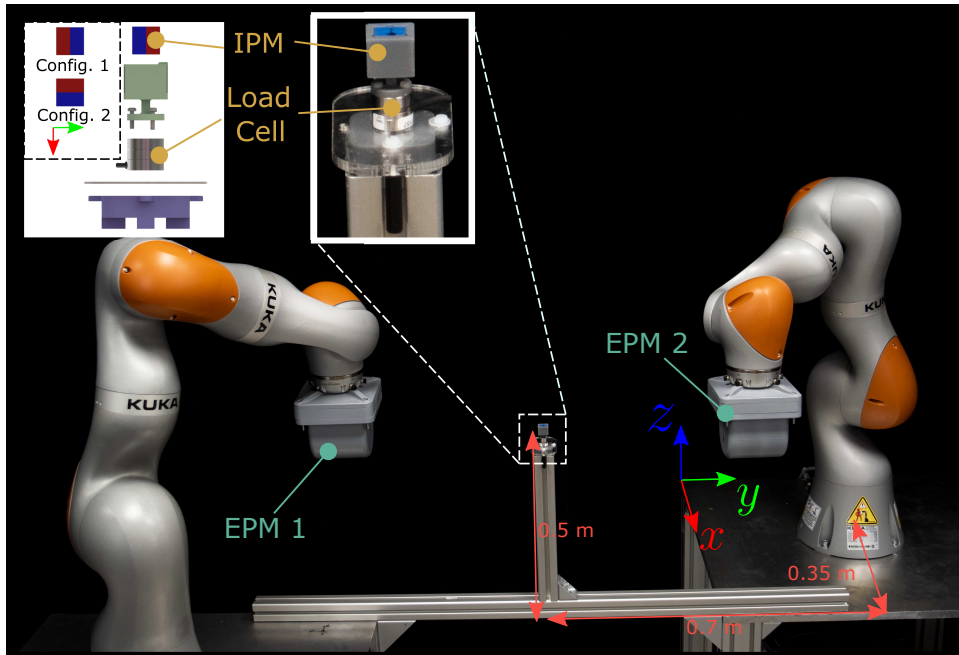


Figure 3.4: Experimental Setup.

can be found in media attached to the paper.

A total of 16 experiments were performed with the 8 cases being repeated twice (for each IPM orientation). The wrench  $w_1(T)$  and  $w_2(T)$  was measured on each load cell for every period  $T \in [0, t_i]$ , for the  $i$ -th case; note that  $t_i \neq t_j$ ,  $i \neq j$ , in general, since some configurations can be reached faster than others from the same initial pose. We rearrange  $w(T) = (w_1^T(T) \ w_2^T(T))^T$  and, according to (3.5), we map the measured wrench onto the independent field components  $U(T) = S^\dagger w(T)$ ; with  $\cdot^\dagger$  we intend the *Moore-Penrose pseudoinverse*.

Our main aim is proving that the 8 components of the field  $U$  can be manipulated independently and, in particular, we are interested in their direction. Moreover, the magnetic field and its differentials are inherently measured on different scales and the maximum field we can generate is higher than its gradient, at the same relative distance between EPM and IPM. Therefore, for each case, we found the mean value of the last 20 s (once convergence is achieved), and normalized each component of the field to its steady state maximum value, over the 8 cases. This data processing eliminates any dependency between measured data and specific IPMs-EPM distance and magnets dimensions, giving an idea of the capabilities of this manipulation approach from a more general perspective.

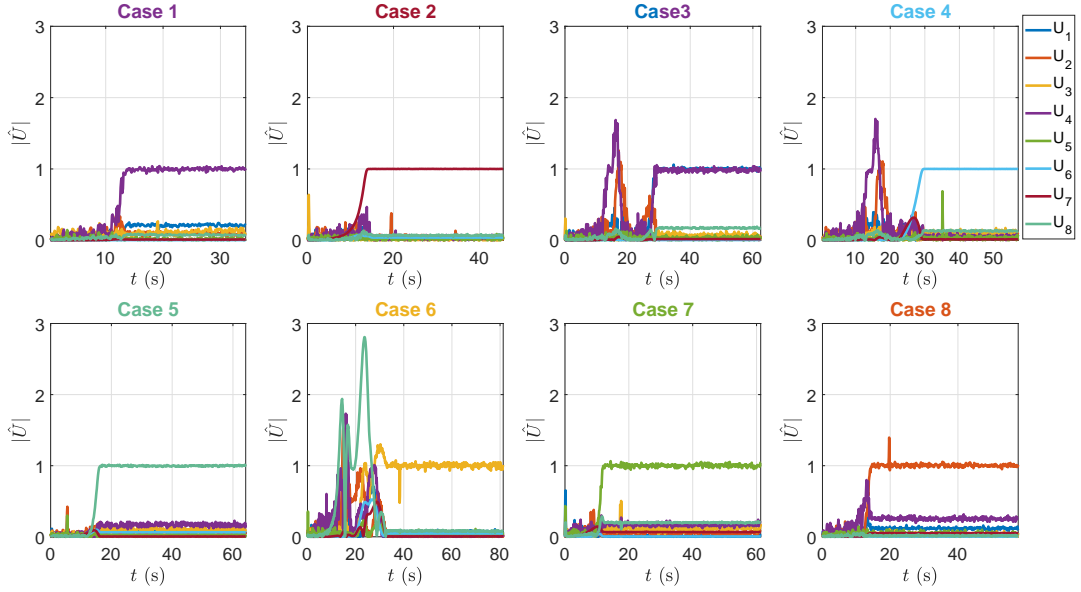


Figure 3.5: Normalized response for magnetic field and differentials. Title colors are referred to the component activated for each case.

In Fig. 3.5 we report the dynamic evolution of the field amongst the 8 experiments, as the EPMS move from initial to final pose. Each case is a combination of the data from the 2 independently analysed IPMS configurations. The title of each case was highlighted with the color of the component(s) of the field we expect to be activated, according to the static scenario in Fig. 3.6. In particular, Fig. 3.6a shows the generated field from the dipole model in (3.1), given the relative EPMS-IPMS pose and normalized to their maximum value ( $|\bar{U}_i|$ ). Fig. 3.6b maps the field components activated for each experimental case ( $|\hat{U}_i|$ ), i.e. the mean steady state value (last 20 s) in Fig. 3.5. For comparison between the theoretical and experimental field, the error  $|E_{U_i}| = |\bar{U}_i| - |\hat{U}_i|$ , is reported in Fig. 3.6c.

In achieving control of the desired DOFs, significant activation of other components of the field is evident in certain cases; specifically, case 3, 4, and 6. This occurs due to the nature of the planned trajectory from the initial *zero-field pose* to the case-specific end pose. Indeed, trajectories were selected to achieve path length minimization, rather than minimizing cross-activation.

Fig. 3.6b shows that we can control 8 independent DOFs and, in particular, the compo-

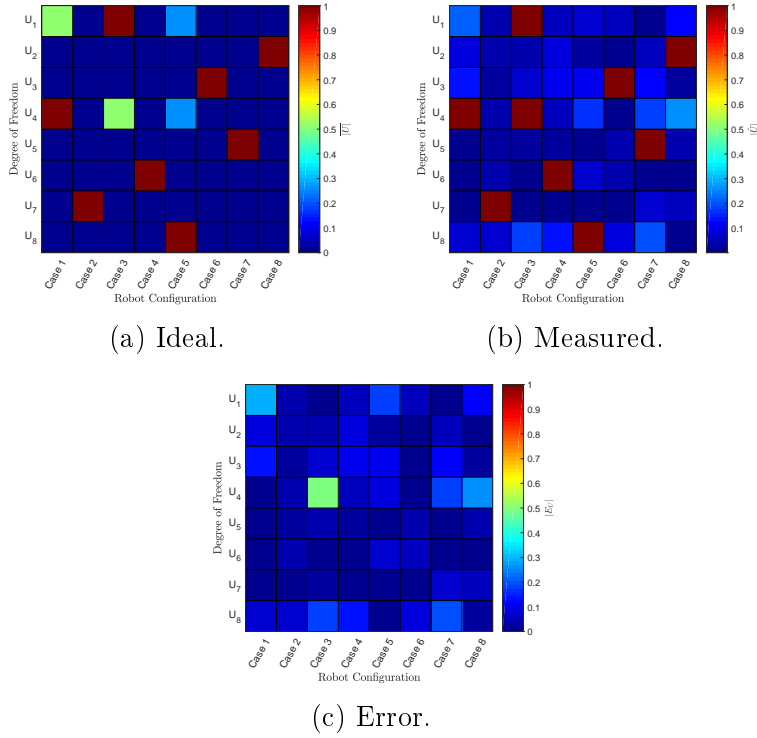


Figure 3.6: Comparison of the ideal (dipole)  $U$  field generated by the poses in Fig. 3.2, as per Table 3.1, and measured field, normalized to their maximum over the cases.

nents predicted by the dipole model. Through comparison of the measured and predicted values, less activation of  $U_1$  and more activation of  $U_4$  is apparent for case 1 and case 3, respectively. This is mainly due to the sensitivity of the gradient to accurate alignment between EPMS and IPMS, which is difficult to achieve open-loop.

From the absolute error  $|E_U|$ , reported in Fig. 3.6c, we computed the mean percentage cross-activation

$$\overline{|E_U|}_{\%} = (5.4, 4.9, 7.9, 10.5, 2.5, 2.3, 2.4, 10.6).$$

This was computed by considering only the components of  $E_U$  that are not desired to activate for each case, i.e. the blank boxes of Table 3.1. This measures the cross-activation, intended as the amount of actuation in a direction that is not required to activate. This is the main difficulty in magnetic actuation: limiting the actuators to very fine control of specific DOFs, without cross-talk. In our case, by employing an open-loop dipole model-based method, we achieve 10.6% of cross-activation, in the worst

case scenario. We believe that the main sources of cross-activation are the usage of an approximated model for the field and the inaccurate knowledge of the IPM pose. An appropriate localization approach will be investigated to further reduce this undesired behaviour.

In practical application of the proposed actuation method, we will consider applying closed-loop wrench control [25; 24], which is expected to reduce these errors significantly.

## 3.6 Conclusions

The present work discussed the manipulation capabilities of robotically manipulated magnetic sources. In particular, we showed that 2 actuated EPMS are able to independently manipulate 8 DOFs.

Both theoretical dissertation and experiments prove that the proposed approach achieves same capabilities of coil based actuation [21], i.e. manipulation of 8 DOFs, in terms of wrench applied to 2 orthogonal independent IPMs within the workspace. The approach of using robotically controlled EPMS, compared to the usage of a coil-based counterpart, has the advantage of minimizing costs, energy consumption and maximizing the target workspace.

To improve the accuracy in controlling each component, future work will be focused on applying closed loop control of the wrench, as in [25; 24], by applying an accurate localization technique. We expect that this approach would enhance the accuracy of control of single components, related EPM-IPM alignment, and reduce the errors related to dipole modeling.

## Bibliography

- [1] J. Burgner-Kahrs, D. C. Rucker, and H. Choset, “Continuum Robots for Medical Applications: A Survey,” dec 2015.

- 
- [2] M. T. Chikhaoui and J. Burgner-Kahrs, “Control of Continuum Robots for Medical Applications : State of the Art,” pp. 25–27, June 2018.
- [3] M. Runciman, A. Darzi, and G. P. Mylonas, “Soft robotics in minimally invasive surgery,” *Soft Robotics*, vol. 6, no. 4, pp. 423–443, 2019. PMID: 30920355.
- [4] P. J. Swaney, J. Burgner, H. B. Gilbert, and R. J. Webster, “A flexure-based steerable needle: High curvature with reduced tissue damage,” *IEEE Transactions on Biomedical Engineering*, vol. 60, no. 4, pp. 906–909, 2013.
- [5] N. Simaan, K. Xu, W. Wei, A. Kapoor, P. Kazanzides, R. Taylor, and P. Flint, “Design and Integration of a Telerobotic System for Minimally Invasive Surgery of the Throat,” *International Journal of Robotics Research*, vol. 28, no. 9, pp. 1134–1153, 2009.
- [6] R. J. Webster, A. M. Okamura, and N. J. Cowan, “Toward active cannulas: Miniature snake-like surgical robots,” in *IEEE International Conference on Intelligent Robots and Systems*, pp. 2857–2863, 2006.
- [7] T. Kato, I. Okumura, H. Kose, K. Takagi, and N. Hata, “Tendon-driven continuum robot for neuroendoscopy: validation of extended kinematic mapping for hysteresis operation,” *International Journal of Computer Assisted Radiology and Surgery*, vol. 11, pp. 589–602, apr 2016.
- [8] P. Breedveld, J. S. Sheltes, E. M. Blom, and J. E. I. Verheij, “A new, easily miniaturized steerable endoscope,” *IEEE Engineering in Medicine and Biology Magazine*, vol. 24, pp. 40–47, Nov 2005.
- [9] G. Gerboni, P. W. J. Henselmans, E. A. Arkenbout, W. R. van Furth, and P. Breedveld, “HelixFlex : bioinspired maneuverable instrument for skull base surgery,” *Bioinspiration & Biomimetics*, vol. 10, p. 066013, dec 2015.
- [10] N. Garbin, L. Wang, J. H. Chandler, K. L. Obstein, N. Simaan, and P. Valdastri, “Dual-continuum design approach for intuitive and low-cost upper gastrointestinal

- endoscopy,” *IEEE Transactions on Biomedical Engineering*, vol. 66, pp. 1963–1974, July 2019.
- [11] S. Calò, J. H. Chandler, F. Campisano, K. L. Obstein, and P. Valdastri, “A compression valve for sanitary control of fluid driven actuators,” *IEEE/ASME Transactions on Mechatronics*, pp. 1–1, 2019.
- [12] J. Edelmann, A. J. Petruska, and B. J. Nelson, “Magnetic control of continuum devices,” *International Journal of Robotics Research*, vol. 36, no. 1, pp. 68–85, 2017.
- [13] S. Jeon, A. K. Hoshidar, K. Kim, S. Lee, E. Kim, S. Lee, J.-y. Kim, B. J. Nelson, H.-J. Cha, B.-J. Yi, and H. Choi, “A Magnetically Controlled Soft Microrobot Steering a Guidewire in a Three-Dimensional Phantom Vascular Network,” *Soft Robotics*, vol. 6, pp. 54–68, oct 2018.
- [14] L. B. Kratchman, T. L. Bruns, J. J. Abbott, and R. J. Webster, “Guiding Elastic Rods With a Robot-Manipulated Magnet for Medical Applications,” *IEEE Transactions on Robotics*, vol. 33, no. 1, pp. 227–233, 2017.
- [15] J. Sikorski, I. Dawson, A. Denasi, E. E. G. Hekman, and S. Misra, “Introducing BigMag - A novel system for 3D magnetic actuation of flexible surgical manipulators,” in *2017 IEEE International Conference on Robotics and Automation (ICRA)*, pp. 3594–3599, 2017.
- [16] P. Valdastri, G. Ciuti, A. Verbeni, A. Menciassi, P. Dario, A. Arezzo, and M. Morino, “Magnetic air capsule robotic system: proof of concept of a novel approach for painless colonoscopy,” *Surgical endoscopy*, vol. 26, no. 5, pp. 1238–1246, 2012.
- [17] Y. Kim, G. A. Parada, S. Liu, and X. Zhao, “Ferromagnetic soft continuum robots,” *Science Robotics*, vol. 4, p. eaax7329, aug 2019.
- [18] A. Azizi, C. C. Tremblay, K. Gagné, and S. Martel, “Using the fringe field of a clinical MRI scanner enables robotic navigation of tethered instruments in deeper vascular regions,” *Science Robotics*, vol. 4, p. eaax7342, nov 2019.

- 
- [19] O. Erin, H. B. Gilbert, A. F. Tabak, and M. Sitti, “Elevation and azimuth rotational actuation of an untethered millirobot by MRI gradient coils,” *IEEE Transactions on Robotics*, vol. 35, pp. 1323–1337, Dec 2019.
- [20] X. Zhang, T.-A. Le, A. K. Hoshiar, and J. Yoon, “A Soft Magnetic Core can Enhance Navigation Performance of Magnetic Nanoparticles in Targeted Drug Delivery,” *IEEE/ASME Transactions on Mechatronics*, vol. 23, no. 4, pp. 1573–1584, 2018.
- [21] S. Salmanipour and E. Diller, “Eight-Degrees-of-Freedom Remote Actuation of Small Magnetic Mechanisms,” in *2018 IEEE International Conference on Robotics and Automation (ICRA)*, pp. 3608–3613, 2018.
- [22] P. Ryan and E. Diller, “Magnetic actuation for full dexterity microrobotic control using rotating permanent magnets,” *IEEE Transactions on Robotics*, vol. 33, no. 6, pp. 1398–1409, 2017.
- [23] C. Heunis, J. Sikorski, and S. Misra, “Flexible Instruments for Endovascular Interventions: Improved Magnetic Steering, Actuation, and Image-Guided Surgical Instruments,” *IEEE robotics & automation magazine*, vol. 25, no. 3, pp. 71–82, 2018.
- [24] L. Barducci, G. Pittiglio, J. C. Norton, K. L. Obstein, and P. Valdastrì, “Adaptive Dynamic Control for Magnetically Actuated Medical Robots,” *IEEE Robotics and Automation Letters*, vol. 4, pp. 3633–3640, jul 2019.
- [25] G. Pittiglio, L. Barducci, J. W. Martin, J. C. Norton, C. A. Avizzano, K. L. Obstein, and P. Valdastrì, “Magnetic Levitation for Soft-Tethered Capsule Colonoscopy Actuated With a Single Permanent Magnet: A Dynamic Control Approach,” *IEEE Robotics and Automation Letters*, vol. 4, no. 2, pp. 1224–1231, 2019.
- [26] J. J. Abbott, E. Diller, and A. J. Petruska, “Magnetic methods in robotics,” *Annual Review of Control, Robotics, and Autonomous Systems*, vol. 3, no. 1, p. null, 2020.
- [27] A. J. Petruska and J. J. Abbott, “Optimal permanent-magnet geometries for dipole

field approximation,” *IEEE Transactions on Magnetics*, vol. 49, no. 2, pp. 811–819, 2013.

[28] A. Isidori, *Nonlinear control systems*. Springer Science & Business Media, 2013.

[29] B. Siciliano, L. Sciavicco, L. Villani, and G. Oriolo, *Robotics: Modelling, Planning and Control*. Springer Publishing Company, Incorporated, 2010.

## Chapter 4

# Optimal Design for Magnetic Continuum Robots

**Chapter source:** G. Pittiglio, P. Lloyd, T. da Veiga, O. Onaizah, C. Pompili, J. H. Chandler, and P. Valdastrì, "Patient-specific Magnetic Catheters for Atraumatic Autonomous Endoscopy," *Soft Robotics* 0 0:0, doi:10.1089/soro.2021.0090.

**Other related papers:** P. Lloyd, G. Pittiglio, J. H. Chandler and P. Valdastrì, "Optimal Design of Soft Continuum Magnetic Robots under Follow-the-leader Shape Forming Actuation," 2020 International Symposium on Medical Robotics (ISMR), 2020, pp. 111-117, doi: 10.1109/ISMR48331.2020.9312943.

## Abstract

Despite increasing interest in minimally invasive surgical techniques and related developments in flexible endoscopes and catheters, follow-the-leader motion remains elusive. Following the path of least resistance through a tortuous and potentially delicate environment without relying on interaction with the surrounding anatomy requires the control of many degrees of freedom. This typically results in large diameter instrument. One viable solution to obtain dexterity without increasing size is via multiple point magnetic actuation over the length of the catheter. The main challenge of this approach is planning magnetic interaction to allow the catheter to adapt to the surrounding anatomy during navigation. We design and manufacture a fully shape-forming, soft magnetic catheter of 80 mm length and 2 mm diameter, capable of navigating a human anatomy in a follow-the-leader fashion. Whilst this system could be exploited for a range of endoscopic or intravascular applications, here we demonstrate its efficacy for navigational bronchoscopy. From a patient specific pre-operative scan, we optimize the catheters magnetization profiles and the shape-forming actuating field. To generate the required transient magnetic fields, a dual-robot arm system is employed. We fabricate three separate prototypes to demonstrate minimal contact navigation through a three-dimensional bronchial tree phantom under pre-computed robotic control. We also compare a further four separate optimally designed catheters against mechanically equivalent designs with axial magnetization profiles along their length and only at the tip. Using our follow-the-leader

approach, we demonstrate up to 50% more accurate tracking, 50% reduction in obstacle contact time during navigation over the state of the art, and an improvement in targeting error of 90%.

## 4.1 Introduction

Over the last few decades, minimally invasive approaches to diagnosis and treatment have emerged to reduce patient trauma and decrease recovery times. Specifically, methods based on flexible endoscopy have gained interest, as they can reach distal anatomical structures without the need for incisions and associated scarring. Despite clear benefits to the patient, minimally invasive, and endoscopic procedures in particular, may require longer learning curves, for surgeons, and system-specific training. Furthermore, surgeons suffer increased fatigue, and the diagnostic yield may vary considerably.[1] Continuum robots (CRs) have been proposed as a possible solution to these problems[2,3,4], owing to the mitigation of cognitive burden and high dexterity. These manipulators, with potentially unlimited Degrees of Freedom (DOFs), can leverage intelligent robotic control to improve capability and attenuate the mental and physical demand on the operator. Despite the benefits of high-DOF actuation, in most cases, this limits CR miniaturization due to the associated need for increased numbers of actuation tendons (e.g. Nguyen and Burgner-Kahrs [5]), pressure lines (e.g. De Falco, et al. [6]), or active internal components (e.g. Kang et al. [7]). To mitigate this problem, magnetically actuated CRs have emerged [8]. These manipulators represent an extension to magnetically actuated endoscopes [9], which have been proven effective in colonoscopy [10]. The possibility to control the tip [11] or full length [12] of magnetic CRs without an associated increase in diameter particularly advantageous. As their diameter reduces, magnetic catheters made from the same material show a greater reduction in stiffness compared to magnetic torque for a given magnetic field (i.e., fourth order diameter-to-stiffness relation vs a second order diameter-to-magnetic torque relation). This gives the potential for highly dexterous manipulators at small scales; well suited to catheter designs. A further advantage of

this actuation strategy is the possibility to control multiple DOFs, via pre-programmed magnetic signatures [13,14], i.e. a lengthwise magnetization profile. This has the potential to facilitate autonomous navigation at the expense of introducing design, fabrication and control challenges to achieve desired shape control during progression through the anatomy. In this paper, we present an improved locomotion approach for magnetically driven soft catheters based on a follow-the-leader (FTL) motion. We combine manipulation properties [15] with signature-based magnetization [12,16] to vary the catheter shape during insertion (see Figure 4.1). The proposed approach is applied to navigational bronchoscopy, which is typically used for performing biopsy of lung lesions that are difficult to reach by traditional bronchoscopy.[17] Electro-Magnetic Navigation (EMN) is a recently introduced image-based procedure with the goal of navigating a small catheter through the bronchial pathway of the lung up to the distal end of the bronchi [17]. In EMN, a passive catheter (rigid and pre-bent) is inserted into the tool channel of the bronchoscope and manually manipulated using continuous electromagnetic feedback combined with pre- and/or intra-operative images. The rigidity of the tool and its limited DOFs and proximal control make the procedure complex to perform, with reliance on catheter-tissue interactions and operator skill. Moreover, cone beam computed tomography (CT) or fluoroscopy, used to visualize instrument location with respect to the lesion, is undesirable in terms of radiation exposure for both patient and medical staff, and adds additional cost to the procedure.[12]

Recent data found that EMN procedures had a diagnostic yield of only 57% over a total of 687 patients.[18] The difficulties in navigating the convoluted bronchial tree led researchers to investigate robotic solutions, such as the MONARCH Platform and Ion Endoluminal System. These approaches have been introduced with the premise that better navigation and more accurate deployment of biopsy tools can improve the diagnostic yield. However, cable-driven robotic systems of this type are comprised of hard components with relatively large diameters; 4.2 mm (MONARCH, Auris Health, Inc., USA ) and 3.5 mm (Ion, Intuitive Surgical, USA). This makes them effective for navigation to the proximal anatomy, but deeper exploration must still be performed using manual, stiff

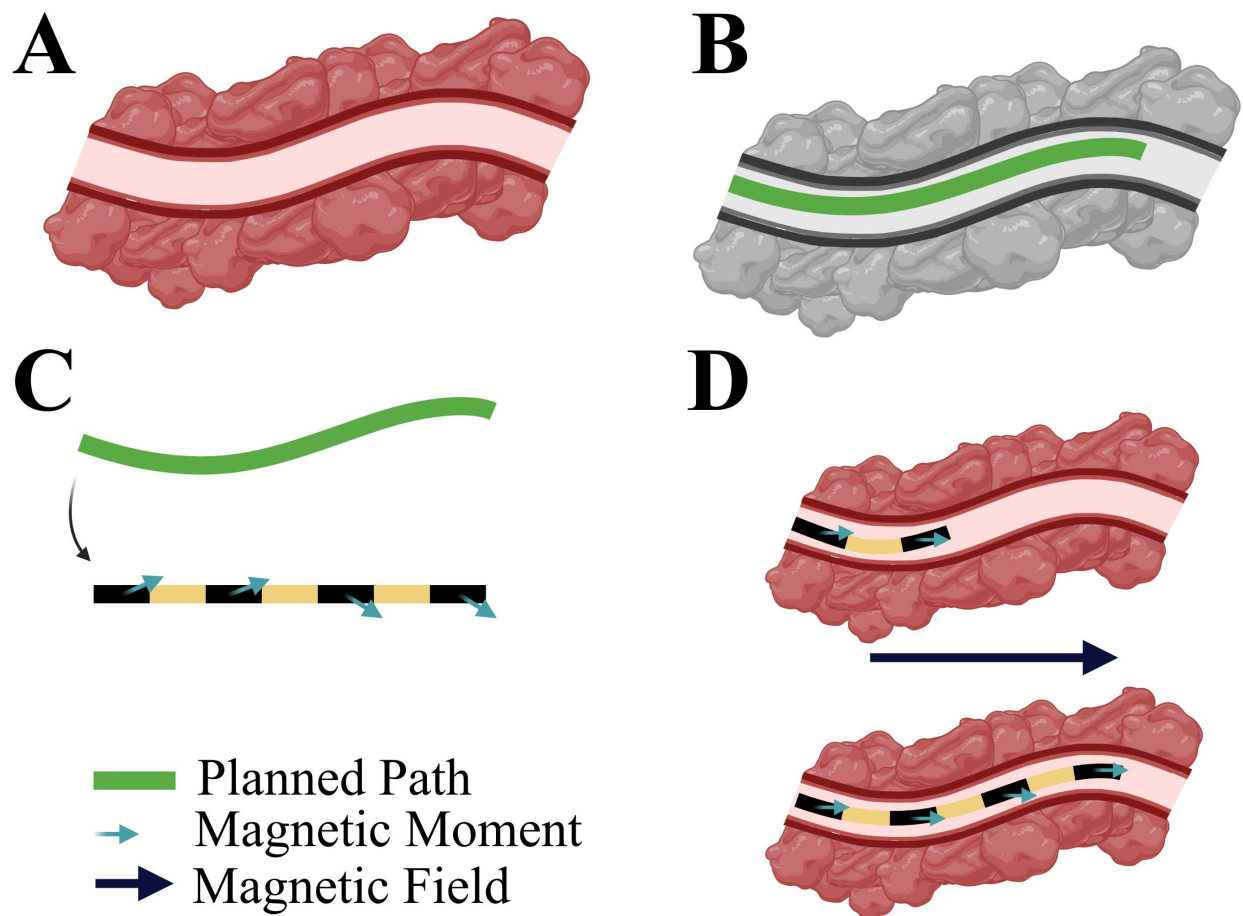


Figure 4.1: Magnetic signature optimization for follow-the-leader navigation. A. Target lumen to navigate; B. Path planning on pre-operative image; C. Signature optimization based on desired path; D. Navigation through the anatomy under applied field.

instruments. In contrast, we show that our proposed 2 mm diameter patient-specific soft magnetic catheter can navigate autonomously, with the potential to penetrate deeper into areas of the anatomy inaccessible to standard instrumentation. The proposed catheter is the same diameter as the rigid tools used in EMN, however, is also soft, anatomy-specific, fully shape-forming and remotely robotically-actuated.[15] We compare the proposed design approach with tip- and axially magnetized catheters, and demonstrate improved navigation in terms of interaction with the environment and reduced targeting error. This is shown via 2D navigation experiments where the shape of the catheter is tracked throughout the insertion process and magnetic field controlled using the dual-robot-arm approach proposed by Pittiglio et al. [19] To demonstrate autonomous navigation in more realistic convoluted pathways, we evaluate our approach on an anatomically accurate 3D phantom of the bronchi extracted from CT scan.

## 4.2 Materials and Methods

The high-level approach to realize shape-forming soft magnetic catheters under follow-the-leader control consists of: (1) determination of the desired navigational path (e.g. extraction from 3D image-based planning [20]); (2) optimization of the lengthwise magnetic profile for the catheter and the magnetic control fields using a magneto-elastic CR model; (3) fabrication of the magnetic catheter from soft elastomeric material with the desired optimized magnetic profile; and (4) synchronous control of the magnetic catheter insertion and the local magnetic field (in line with the optimization). The following sections detail the approaches taken to realize these specific elements.

### 4.2.1 Rigid-link Modelling and Design Optimization

A popular approach for modelling elastomeric CRs is as a serial chain of spring-loaded rigid links.[14,20] With sufficient links, such that no individual joint angle is large enough to violate the assumption of elastic linearity, an accurate representation of the CR when influenced by forces and torques is provided. One advantage of the rigid-link representa-

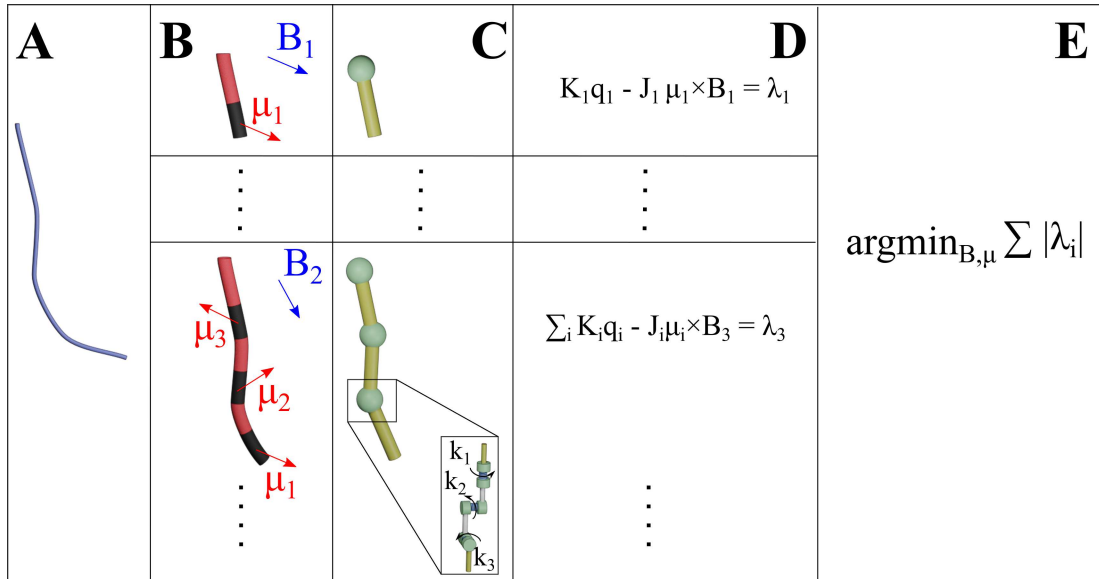


Figure 4.2: Building the optimization routine. A. The desired path extracted from a pre-operative image. B. The catheter as a serial chain of magnetized segments at each time-step of insertion. C. The rigid-link representation for the purpose of optimization and, inset, the three orthogonal virtual joints. D. Formulate an equilibrium at each time-step. E. Sum of the normal of each time-step gives the input to the genetic algorithm function.

tion is the ease with which the CR fits into the traditional robotics manipulator Jacobian model. As shown in Figure 4.2, the rigid-link mechanical model and the magnetic torque equation for a current free field are employed within an optimization routine based on Lloyd et al. [14]. Given a desired path (Figure 4.2A), the optimization determines the lengthwise magnetization profile ( $\mu_i$ ) of the catheter and the applied field ( $B_i$ ) at each time-step.

For the presented examples, each catheter design is formed from multiple segments (Figure 4.2B); each with its own magnetization direction and represented by a single rigid link (Figure 4.2C). The mechanical joint torque is determined as the product of joint angle ( $q_i$ ) and pseudo-spring stiffness ( $k_i$ ). All joints are of the same geometry and material, meaning the pseudo-spring constants ( $k_i$ ) used to represent mechanical resistance to beam deformation are uniform at every virtual joint. As shown in Figure 4.2C, each manipulator joint we modeled as a serial chain of three joints representing rotation about each of three axes; the  $z$  joint manifests as the twisting primitive whereas the  $y$  and  $x$  joints represent two orthogonal bending primitives. The pseudo-spring constants for each

joint are given by  $k = EI$ ,  $I = \text{diag}(I_x, I_y, I_z)$ ; where  $I_z = \pi r^4/2$  is the area moment of inertia in the twisting primitive,  $I_x = I_y = \pi r^4/4$  is the area moment of inertia in the bending primitive  $E$  is the elastic modulus.

The magnetic joint torque is defined as the product of the manipulator Jacobian transpose ( $J_i$ ) at any given time-step ( $i$ ) and the magnetic wrench; determined as the cross product of the magnetic moment ( $\mu_i$ ) and applied magnetic field ( $B_i$ ), assuming the field is homogeneous. The difference between magnetic and mechanical joint torque ( $\lambda_i$ ) is given by the relationship in Figure 4.2D and, for a system in equilibrium, should be zero;  $K_i = \text{diag}(k_1, k_2, k_3)$ . Balancing the mechanical and magnetic wrenches gives, for a known set of joint angles, an open form solution with unknowns in magnetization and applied field. These are three dimensional vectors at four locations (in the case of  $\mu$ ) and four time-steps (in the case of  $B$ ), resulting in a 24-dimensional optimization with non-unique solutions. We then minimize the sum of the Euclidean norm of the residual torque (see Figure 4.2). This scalar optimization was solved using the MATLAB genetic algorithm function (MATLAB and Global Optimization Toolbox R2018b, The MathWorks Inc., Natick, MA, USA) with a population size of 200, maximum generation count of 200, a mutation rate of 1% and a function tolerance of  $10^{-9}$  Nm.

### 4.2.2 Catheter Fabrication

To produce the optimized catheter designs, individual magnetic segments were first fabricated with specific geometric and magnetic properties. Magnetic segments were formed by casting silicone pre-polymer (Dragon Skin<sup>TM</sup> 30, Smooth-On Inc., U.S.A.) mixed with magnetic microparticles (NdFeB, MQFP-B+, Magnequench GmnH, Germany) in a 3D-printed mold (Tough PLA, Ultimaker S5, USA), see Figure 4.3A. The two-part mold was assembled with inclusion of two guide pins per segment (0.33 mm diameter Nitinol (NiTi) wire); inserted orthogonally to the long axis of the segments to act as indexing features for subsequent magnetization and assembly. The silicone and magnetic particles, in a 1:1 ratio by mass, were mixed and degassed for 90 seconds in a high vacuum-mixer (ARV310, THINKYMIXER, Japan) followed by injection into the mold using a standard

syringe. The silicone was cured at room temperature for a minimum of 4 hours before demolding. Once demolded and separated, each segment was magnetized using an impulse magnetizer (IM-10-30, ASC Scientific, U.S.A.). To induce the desired magnetic moment, as determined through the design optimization process, Figure 4.2, custom magnetizing trays were printed for each segment (Tough PLA, Ultimaker S5, USA) with indexing pin holes to guarantee segment orientation with respect to the unidirectional magnetizing field, see Figure 4.3B. Once all required magnetic segments were magnetized, they were assembled in appropriate order into a second two-part mold; using the indexing holes and pins to facilitate correct alignment and spacing during molding, see Figure 4.3C. Finally, silicone (Ecoflex<sup>TM</sup> 00-30, Smooth-On Inc., USA) without magnetic particles was mixed, degassed and injected into the mold to produce the complete catheter with specific magnetic signature, see Figure 4.3D.

To generate locally invariant magnetic properties under actuation and improve conformation to the rigid-link model, magnetic segments (representing links) were formed from silicone with higher stiffness than the adjacent inter-segment ‘joints’. For 2D phantom tests reported below, an overall catheter diameter of 4 mm was used to improve image capture and data acquisition, while in the 3D anatomical model the overall diameter was reduced to 2 mm, which is our clinical target size. To improve contrast with the 3D anatomical model, red pigment (PM5 186 Sil Pig, Smooth-On Inc., USA) was added to the non-magnetic silicone (0.1% by mass). For 2D phantom tests reported below, four optimally-magnetized catheters were fabricated (in addition to one each of tip- and axially-magnetized control samples). For the 3D anatomical demonstration, a further three optimally magnetized catheters were fabricated.

### 4.2.3 Dual Arm Magnetic Manipulation

We apply the controlling magnetic field via the dual-robot-arm approach proposed by Pittiglio et al. [19]. The aim of this dual External Permanent Magnet (dEPM) system (represented in Figure 4.4) is to produce specific magnetic fields to generate torques on the magnetic segments of the catheter, as in Figure 4.2D. Compared to a single permanent

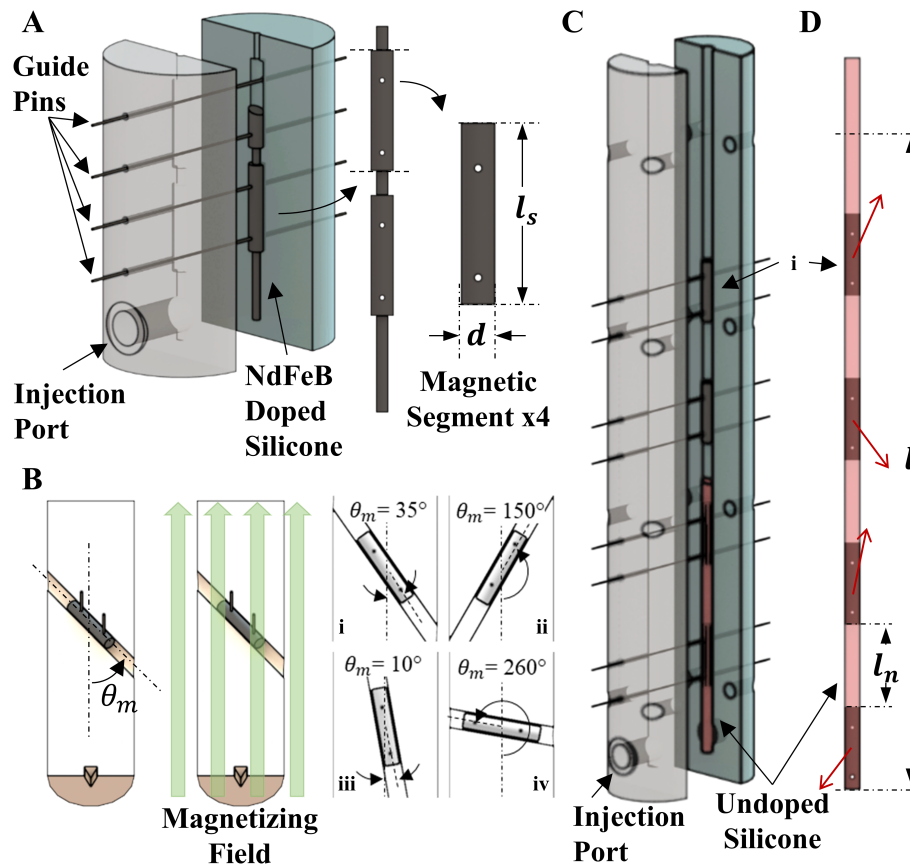


Figure 4.3: Fabrication process to produce SCMRs with specific magnetic signatures. Independent magnetic segments with indexing features are cast from silicone doped with magnetic microparticles (NdFeB), see A. Each segment is subsequently fixed with a specific rotational alignment angle (" $\theta_m$ ") using guide pins and bespoke printed trays, and a high strength uniform magnetic field applied, see B. Magnetic segments are transferred to a second mold and arranged using their indexing features while un-doped silicone is injected into the mold, see C. Subsequent curing and demolding results in SCMRs with specific magnetic signatures, see D.

magnet [21, 22], the dEPM system can produce gradient-free magnetic manipulation and, with respect to electromagnetic coil [2,3] systems, can more readily generate strong magnetic fields over a larger workspace. Furthermore, permanent magnets represent a more efficient solution than coils, since they provide higher magnetic flux density and do not require the supply of current to operate. However, this is at the expense of complexity, as coil systems can offer more intuitive control by current modulation. [21,22] The design procedure is based on the assumption that the actuation method can generate a homogeneous field. Although the dEPM cannot generate the same field everywhere in the workspace, we can balance the gradient generated by 1 EPM with 2 opposing EPMs. For safety purposes, we also restrict the position of the robots to be always on the opposite sides of the patient (see Figure 4.4). This ensures they do not collide with the patient or with each other. We can describe the actuation approach by using the dipole model

$$\begin{aligned} B_i &= \frac{\mu_0}{4\pi|r_i|^3}(3\hat{r}_i\hat{r}_i^T - Id)m_i \\ \frac{\partial B_i}{\partial r_i} &= \frac{\mu_0}{4\pi|r_i|^4}((Id - 5\hat{r}_i\hat{r}_i^T)(\hat{r}_i^T m_i) + m_i^T \hat{r}_i + \hat{r}_i m_i^T) \end{aligned}$$

where  $B_i$  is the field generated by the  $i$ th EPM at position  $r_i$  with respect to the center of the workspace,  $m_i$   $i$ th EPM's magnetic moment and  $\frac{\partial B_i}{\partial r_i}$  the field gradients; herein  $|\cdot|$  refers to the Euclidean norm and  $\hat{\cdot}$  to the vector direction. We impose the EPMs to be respectively along  $+y$  and  $-y$  axis, i.e.  $\hat{r}_1 = \hat{r}_2 = -e_2$ ,  $e_2$  second element of the identity matrix  $Id$ . Also, we consider only poses for which  $m_1 = m_2 = m$  and  $|r_1| = |r_2| = |r|$ , thus simplifying the overall field

$$\begin{aligned} B_i &= \frac{\mu_0}{4\pi|r|^3}(3e_2e_2^T - Id)|m|\hat{m} \\ \frac{\partial B_i}{\partial r_i} &= 0 \end{aligned}$$

Given the desired field  $B_d = |B_d|\hat{B}_d$  we find the pose of the robots as

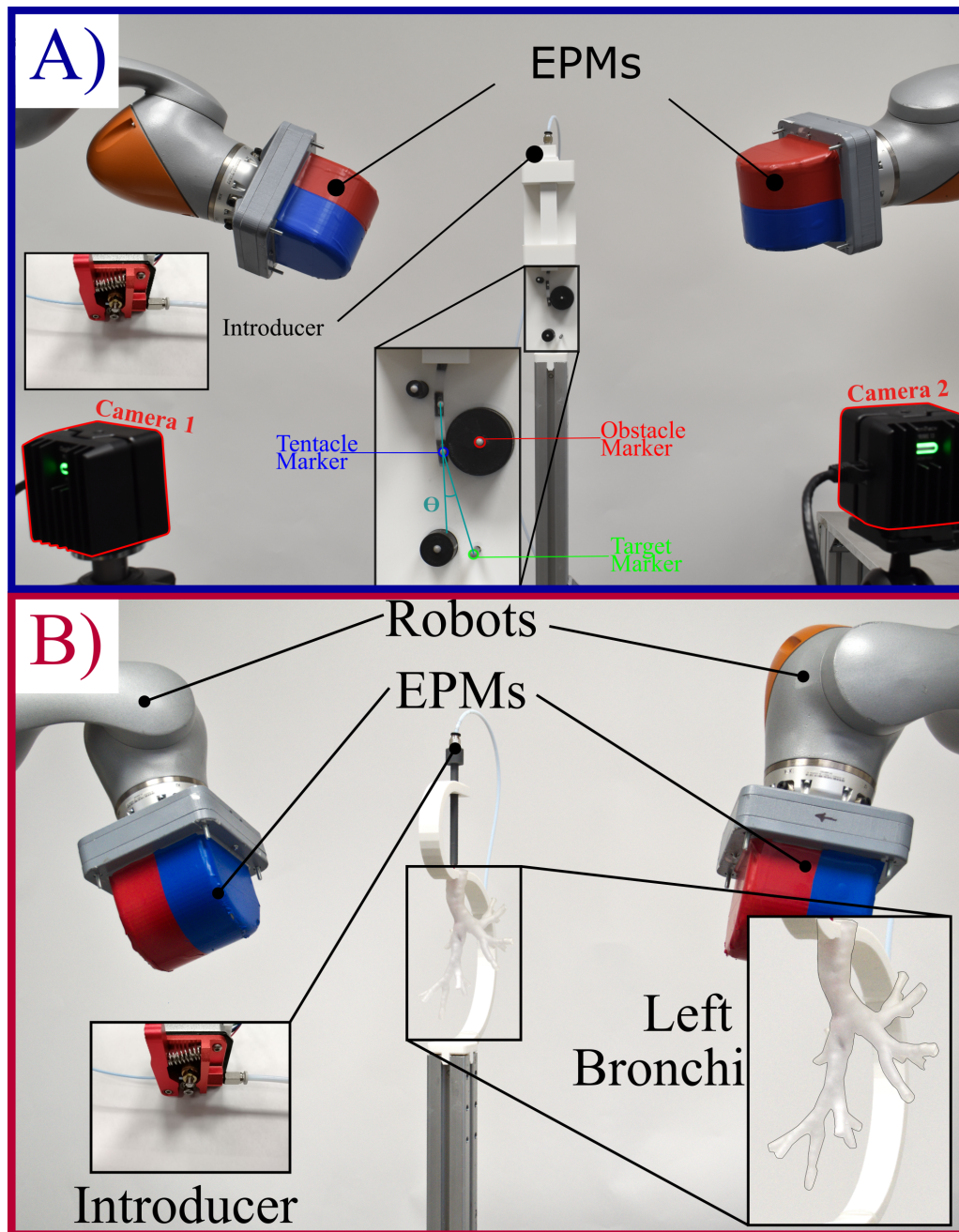


Figure 4.4: A. Experimental setup for comparison between tip-, axially-, and optimally-magnetized catheters. Markers were placed on the 4 magnetic segments of the catheters, on the obstacles and the target. Infrared cameras were used to track these markers. The angle  $\theta$  is referred to as heading error and measures the accuracy of the tentacle to reach the target. B. Dual-arm magnetic manipulation platform for navigational bronchoscopy. A 3D printed anatomically-accurate phantom, extracted from CT imaging, is used for demonstration purposes.

$$\begin{cases} |r| &= \left( \frac{2\pi|B_d|}{\mu_0|m|} \right) \\ \hat{m} &= (3e_2e_2^T - Id)^{-1}\hat{B}_d \end{cases}$$

Notice that the norm of the magnetic moment  $|m|$  is constant and not controllable for permanent magnets. The robots are eventually controlled to the desired pose by kinematics inversion, depicted from the desired position  $r_i$  and EPM magnetic moment  $m_i$ . This control is synchronized with the actuation of the insertion of the catheter. Notice that, in the center of the workspace, we can generate negligible gradients, while a single EPM would inherently generate field gradients. This guarantees a minimization of field inhomogeneity, which is an assumption of the proposed optimization approach.

#### 4.2.4 2D Experiments

To demonstrate the advantages of the proposed approach with respect to more simple catheter magnetizations, we performed 2 experiments: (1) a static (fixed length) obstacle avoidance example, and (2) three 2D navigation scenarios. For each experiment, three catheter designs were produced: (i) a catheter with only the distal segment magnetized in the axial direction - tip-magnetized, (ii) a catheter with all segments axially magnetized - axially-magnetized and (iii) an optimized catheter with variable length-wise magnetization - optimized. The optimization technique detailed in Figure 4.3 was implemented in the same way for all three catheter designs. In the first two cases, the magnetization directions were constrained throughout the optimization to tip-segment axial and all-segments axial, respectively. Similarly, identical implementation of the algorithm to generate optimal actuating fields was employed for all cases. All catheter designs and controlling fields were therefore optimized with the goal of controlling the catheter shapes to the desired path as accurately as possible. All catheters were fabricated with identical mechanical properties at a diameter of 4 mm to facilitate placement of 3 mm diameter position tracking markers. 3D tracking of the magnetic segments was performed using an optical tracking system (OptiTrack, Natural Point Inc., USA). Each 2D workspace and obstacle design was 3D printed (Tough PLA, Ultimaker, USA) and additional tracking

markers were located at each obstacle to act as reference points. Desired magnetic fields were generated using the dEPM system in all cases. A representative example of the experimental setup is presented in Figure 4.4A. For experiment (1), three catheter designs (i.e. tip-magnetized, axially-magnetized and optimized) were actuated at fixed length (i.e. 60 mm) to deform around a single circular obstacle. In each case, the maximum bending angle at the tip (with respect to a referential vertical position) was evaluated up to the point of contact with the obstacle. For the navigation experiment (2), we considered 3 scenarios with varied obstacle and target positions. The choice of obstacle and target locations, and therefore catheter trajectories, was driven by both a practical constraint and a desire to demonstrate the multi-directional capacity of the optimization algorithm. The 2D demonstrative pathways were not based on anatomical images. These are a proof of concept in which obstacle and target locations were chosen to best demonstrate the multi-directional capacity of the optimization algorithm. The resulting catheter trajectories are defined as those which give the maximum aggregate clearance from all the obstacles in the navigation whilst terminating at the target node. We selected trajectories which challenge our optimization procedure to accommodate multiple changes of direction in one navigation, i.e., S-shaped deformation as opposed to C-shaped deformation. These convoluted routes represent a more rigorous test of shape-forming capacity and result in non-intuitive magnetizations and applied fields. To facilitate insertion of the catheter designs, a bespoke introducer system was developed based on a Bowden cable mechanism (Figure 4.4). A low-friction Bowden tube was connected between the drive mechanism and the test phantom using threaded Bowden mounts. A 2mm diameter filament was inserted through the Bowden tube and gripped at the proximal end between a drive gear and a spring-loaded idler bearing. A stepper motor (17HD34008-22B, Brusheng), coupled directly to the drive gear and controlled via a microcontroller (Arduino UNO, Arduino), was used to control the insertion length of the filament. To connect each catheter design, the filament was extended beyond the distal end of the Bowden tube and the catheter design reversibly coupled to the filament using a 3D printed pressure-fit coupling. The filament was subsequently retracted to the insertion start position for the catheter-test

configuration (representing 0 mm displacement along the z axis). Subsequently, continuous insertion of the coupled filament and catheter was synchronized with the dEPM system and optical tracker to actuate and measure the catheter shapes respectively.

### 4.2.5 Anatomical Phantom Experiments

To demonstrate the proposed approach with realistic 3D anatomy, we extracted 3D pathways from a preoperative CT scan of the lungs from the Lung Image Database Consortium image collection (LIDC-IDRI-0807) ([www.cancerimagingarchive.net](http://www.cancerimagingarchive.net)). Full pathways were extracted from trachea to sub-segmental bronchi (diameter less than 4mm); segmented from the CT data using 3D Slicer ([www.slicer.org](http://www.slicer.org)). In contrast to standard EMN and Robotic Assisted Bronchoscopy (RAB), we used pre-operative imaging to design and fabricate patient-specific magnetic catheters to facilitate autonomous navigation via synchronized field-insertion control. Since the magnetic catheter is designed to shape autonomously to the pre-determined path, the surgeon is completely relieved of the cognitive burden of navigation. The procedure from image segmentation to design optimization is shown in Figure 4.4B. A section of the left bronchial tree, from left primary bronchus to subsegmental bronchi, was extracted from pre-operative CT (Figure 4.5A). Three independent 80 mm pathways of minimum diameter 2mm were selected (Figure 4.5B), optimization of the magnetization and control field for each was performed (as detailed in Figure 4.2) to produce three path-specific catheters (Figure 4.5C).

A phantom corresponding to the isolated anatomical region was 3D printed in flexible resin (Flexible 80A, Form 2, Formlabs, USA) and fixed in place within the dEPM robotic field control system using a 3D printed holder (Ultimaker Tough PLA, Ultimaker S5, Ultimaker, USA), see Figure 4.4. Prior to testing, the catheter was connected to the same introducer mechanism described in the previous section. In this case, the distal end of the introducer was coupled to a rigid 3D printed insertion channel with internal and external diameter of 3 mm and 6 mm respectively (Figure 4.4B). This was designed to be comparable to the tool channel and outer diameter of standard bronchoscopes used for EMN (e.g. BF-1T180, Olympus Corporation, USA). As in the 2D navigation case,

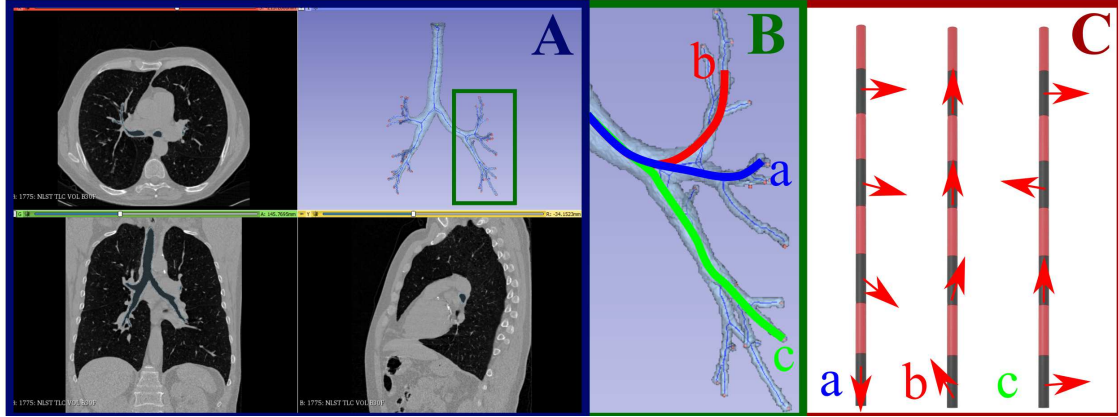


Figure 4.5: From a pre-operative CT image to an optimized magnetic catheter. A. The slicer dataset from the CT scan. B. Datapoints are extracted and aggregated into a connectivity matrix, paths from proximal to distal nodes are extracted for three different targets. C. Optimized magnetizations will follow-the-leader shape form along their respective desired navigations.

forward motion of the catheter is actuated by step commands which run synchronously with the robot arms such that the catheter is inserted into the anatomy as the magnetic field is manipulated to the desired vector. The experimental setup detailed is shown in Figure 4.4. To demonstrate successful navigation of the optimized catheters through the phantom, due to lack of an absolute measure, we performed a visual analysis of the videos. In fact, due to the opacity of the phantom, we could only visualise the catheter by transforming the video of the area of interest to black and white and increasing the contrast. This makes the catheter visible through most of the phantom (particularly in the narrower branches).

## 4.3 Results

### 4.3.1 2D Obstacle Avoidance

Results from the 2D obstacle avoidance experiment can be seen in Figure 4.6, where alpha represents the angle between the catheter tip in its actuated and unactuated (vertical) poses. It can be observed that larger deflection is possible before contact occurs in the optimized arrangement (Figure 4.6C). Both tip and axially magnetized specimens (Figure 4.6A and B respectively) impact the obstacle long before achieving the level of tip rotation

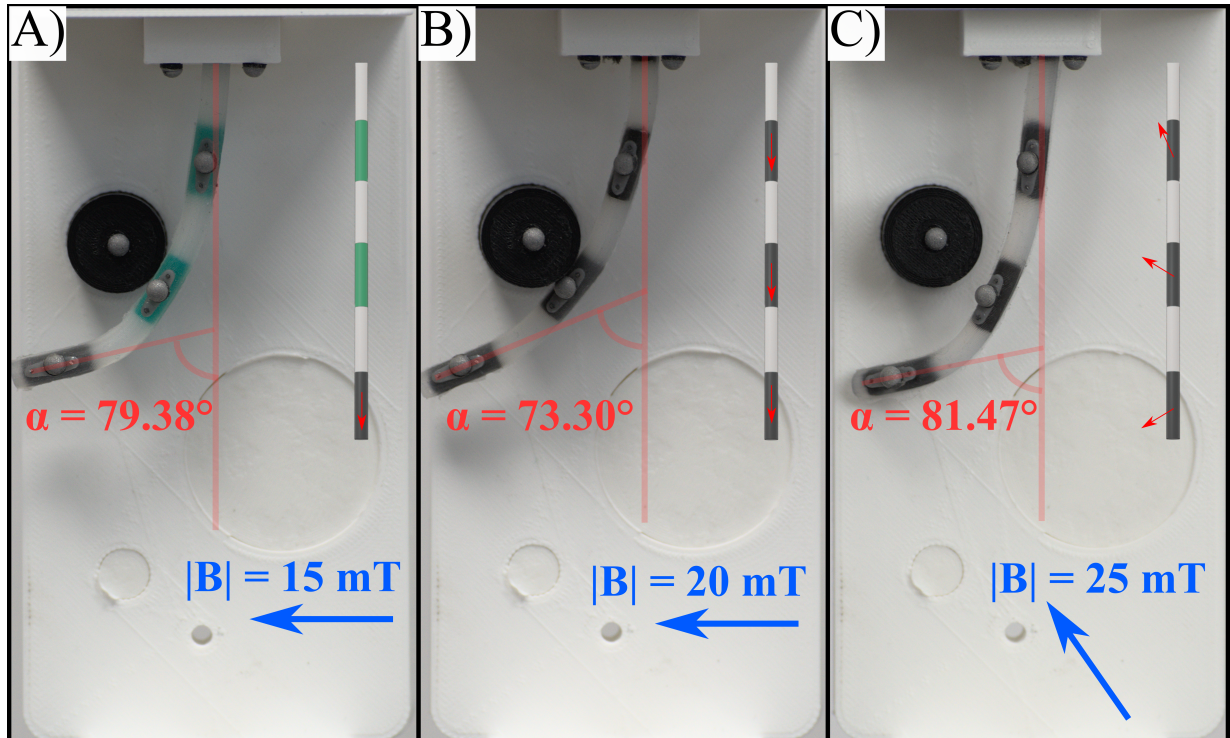


Figure 4.6: Results of obstacle avoidance experiments. Comparison of tip-magnetized (A), axially-magnetized (B) and optimally-magnetized (C) catheters. The angle  $\alpha$  refers to the amount of deflection, compared to the vertical axis.

attained by the optimized specimen. Under actuation, the tip and axially magnetized specimens can only achieve the large deflections shown by utilizing contact with the obstacle. The optimized specimen can be seen to deform through a larger angle whilst also avoiding obstacle contact. This is believed to facilitate navigation, since we can decouple tip from full-body shaping, guaranteeing we can shape to the anatomy without inherent contact with it.

These experiments are presented in Supplementary Video 1. It can be seen that, transitioning to the final state, the optimally-magnetized catheter experiences some torsion around its main axis. This is particular to magnetic catheters whose magnetization is not purely axial. In some cases, this can cause undesirable behaviour due to instabilities. The result from the obstacle avoidance presents a simplified and intuitive example of the optimized magnetic signature concept, which is expanded in the following sections.

### 4.3.2 2D Navigation

Results are shown for three scenarios in which we report the shape of the catheter during navigation with tip magnetization, axial and finally with optimal magnetization; Figure 4.7, Figure 4.8 and Figure 4.9 respectively. Videos of the insertion processes for the three scenarios are shown in Supplementary Videos 2, 3 and 4, respectively. Also shown are the results of a Finite Element Analysis (FEA) which employed the Maxwell Stress Tensor to simulate the Magneto-Mechanical interaction. The tip- and axially- magnetized catheters can be seen to not shape form to these convoluted trajectories. This, as shown in Figure 4.7, Figure 4.8 and Supplementary Video 2 and 3, leads to physical interaction with the surrounding environment which compromises navigational capacity: i.e., not reaching the target (e.g., Figure 4.7A, tip magnetized). The tip-driven catheter interacts with the environment since its full shape cannot be controlled with any applied field. In Scenario A (Figure 4.7), it cannot overcome the last obstacle since it is constrained by the penultimate obstacle and cannot shape around it. Similar results are observed in Scenario B (Figure 4.8). In Scenario C (Figure 4.9), navigation to the target is achieved, since bending is not constrained. In all the three scenarios, however, it cannot reach the target as accurately as the optimized catheter, due to interaction with the obstacles.

The axially-magnetized catheter, despite interaction with the obstacles, is always able to reach the target. We hypothesize that this is due to the higher torque that can be applied to the overall catheter, compared to the tip-magnetized version. Nevertheless, environmental interaction is always present and hinders navigation capabilities. As obstacles are impacted, targeting abilities are adversely affected in comparison to the optimized approach; since tip position depends on the interaction of the full shape with the obstacles. In contrast to the tip- and axially-magnetized cases, we observe minimal interaction between the optimally designed catheter and the obstacles around which it is shaping across the three scenarios. The catheter can shape-form to the anatomy in a follow-the-leader fashion, as designated by the preoperative planning.

These results are summarized in Table 4.1, where the heading error  $\theta$  (defined in

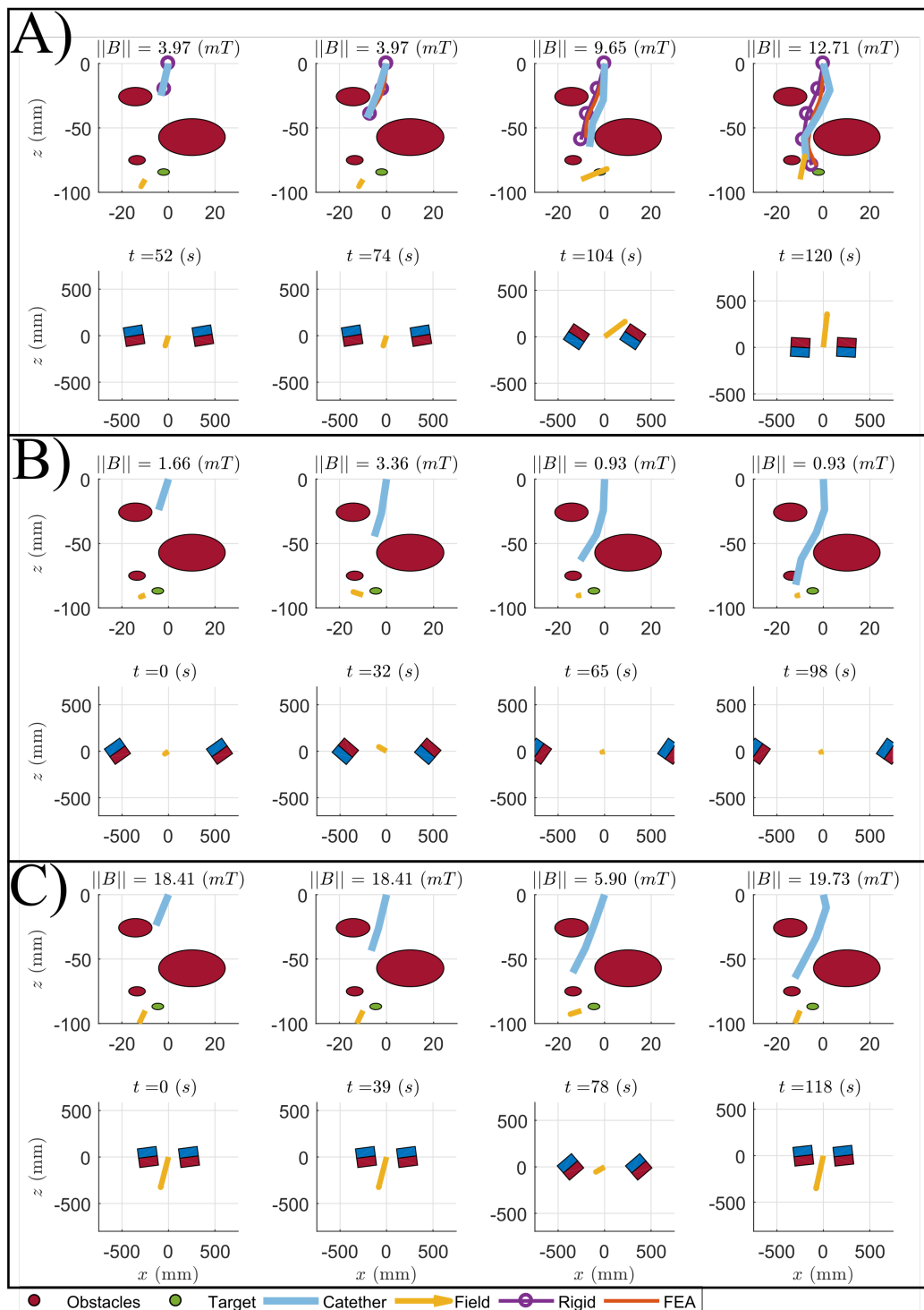


Figure 4.7: Scenario A of comparison between the tip-magnetized (A), axially-magnetized (B) and optimally-magnetized (C) catheters.

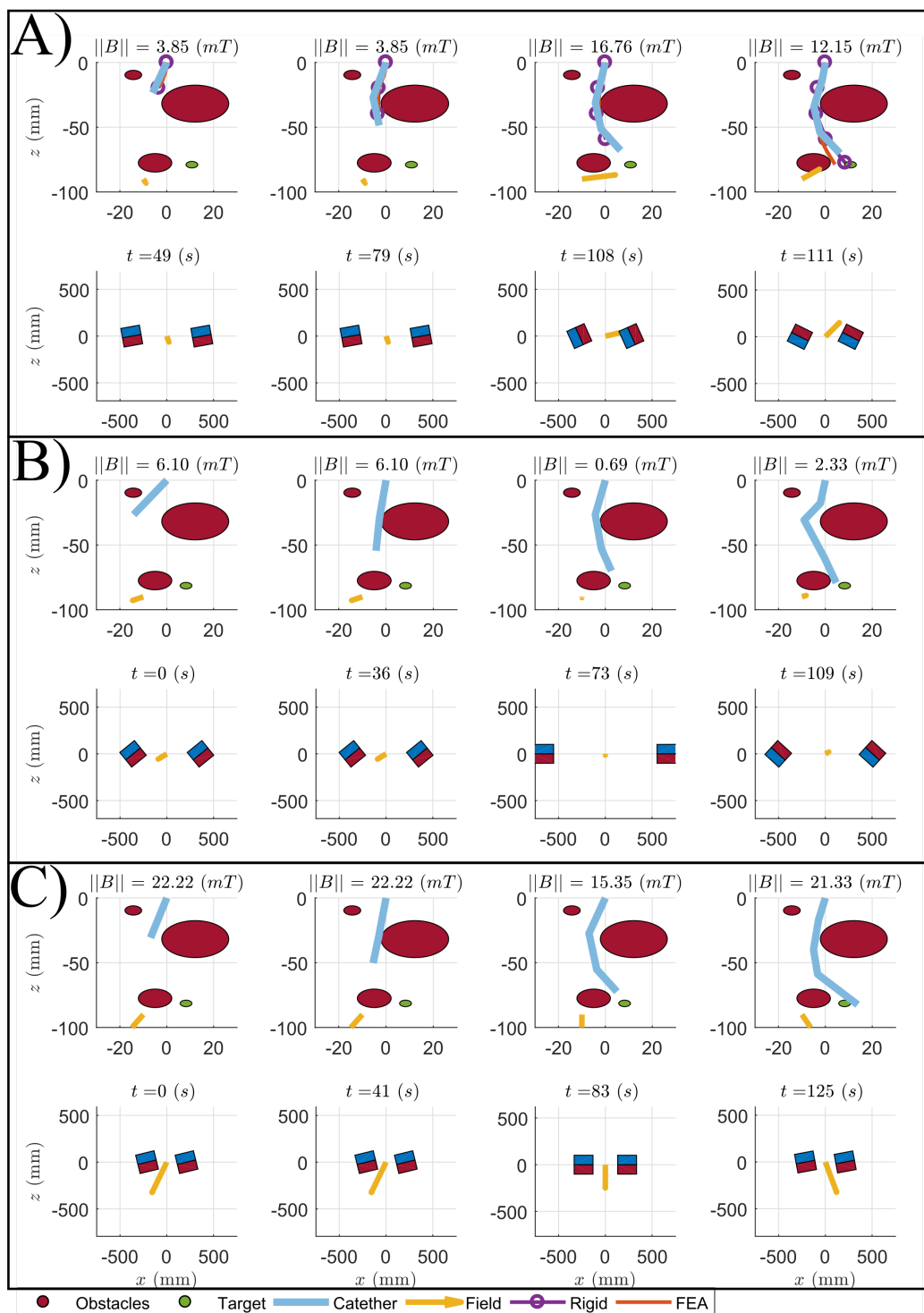


Figure 4.8: Scenario B of comparison between the tip-magnetized (A), axially-magnetized (B) and optimally-magnetized (C) catheters.

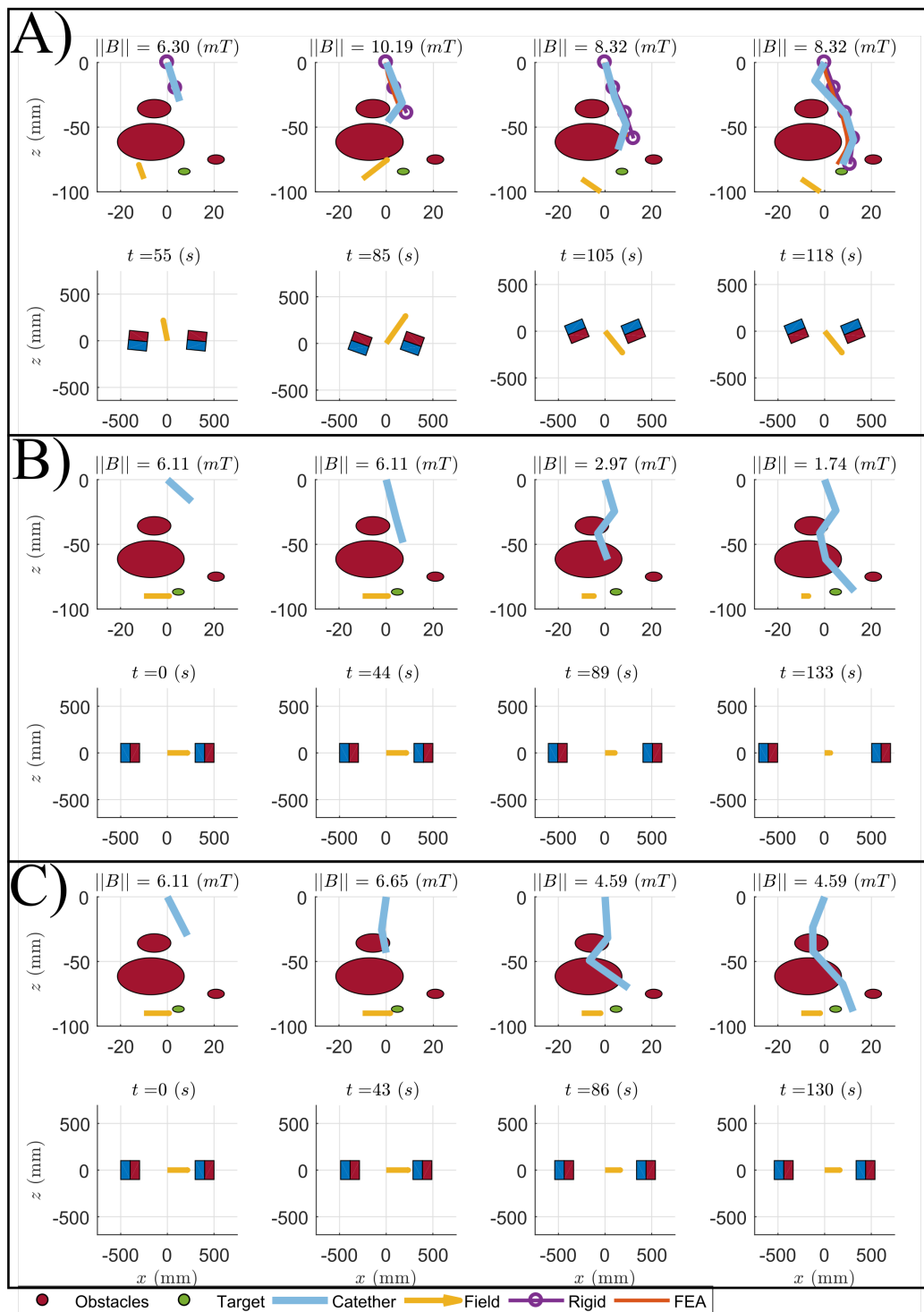


Figure 4.9: Scenario C of comparison between the tip-magnetized (A), axially-magnetized (B) and optimally-magnetized (C) catheters.

	Scenario A			Scenario B			Scenario C		
	Tip	Axial	Opt.	Tip	Axial	Opt.	Tip	Axial	Opt.
<b>Heading Error (deg)</b>	36.8	79.9	10.9	35.9	47.5	8.6	96.7	102.5	4.2
<b>Contact Time (s)</b>	65	42	3	71	58	13	63	44	25
<b>Tracking Error (mm)</b>	27.0	25.7	26.4	25.0	28.1	22.7	67.8	58.0	32.4

Table 4.1: Summary of the results of the 2D experiments. Heading Error, Contact Time and Tracking Error through each navigation.

Figure 4.4A), and obstacle contact time and tracking error, are reported. The former is computed at the completion of each insertion (Scenarios A, B, C, in Figure 4.7, Figure 4.8 and Figure 4.9 respectively). The contact with the obstacles was computed by timing the contact between each obstacle and any section of the catheter from the supplementary videos. The overall results show that the optimal catheter can improve the navigation capabilities, by both reducing contact with the surrounding environment and achieving better targeting. For each insertion step, we compute the error between the optical marker(s)’ measured position and their desired position as along the x axis. We compute the absolute value of the error and sum it through the insertion steps and use it as a measure of the “Tracking Error” in Table 4.1. From this metric we can see how tip- and axially-magnetized catheters can follow the path by benefiting from the interaction with the environment, while the proposed design is always consistent regardless of the surroundings. In fact, in Scenario A the axially-magnetized catheter’s tracking error is comparable to the optimal catheter. However, in Scenarios B and C, where the environment provides less aid in shaping, the optimal design guarantees the desired shaping, while the others fail (see also Figure 4.9 and the Supplementary videos 1, 2 and 3). In summary, the proposed design achieves contact minimization and consequently guarantees path following without the need for environmental interaction. This is fundamental in complex anatomical scenarios when the obstacles cannot provide the needed aid or, worse, they would prevent the catheter from following the desired path, forcing it to undesired shapes.

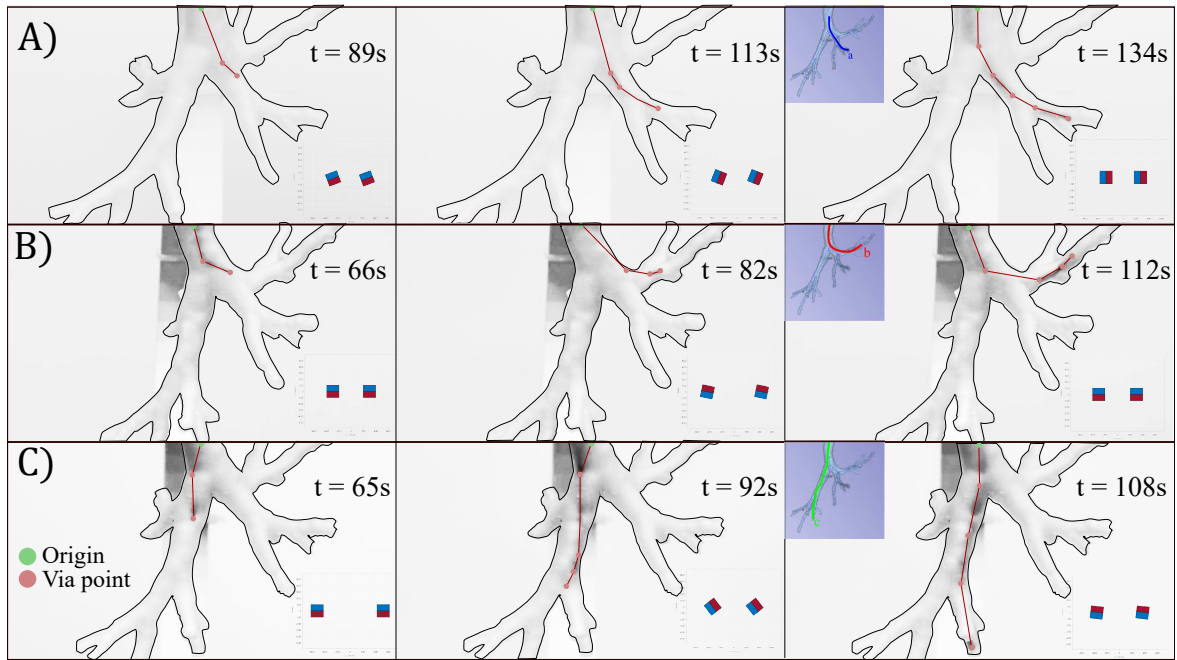


Figure 4.10: Demonstration of Navigation in 3D. Highlighted in red, the shape of the catheter. On the bottom right corner of each image, the position of the EPMS (grid size  $200 \times 100$  mm). On the top right corner of each last step the desired pathway for which the catheter is designed.

### 4.3.3 Anatomical Phantom Experiments

The selected routes were chosen to demonstrate navigation capabilities in diverse anatomical features that may be encountered in EMN. These pathways are commonly difficult to reach with standard bronchoscopy, due to their convoluted shapes. In Figure 4.10 we show the three anatomical experiments. Since the phantom is only partially transparent, we detail the shape of the catheter (red line); extracted by visual analysis. Specifically, we marked the via points (red dots), i.e., the sections of the catheter visible from the black and white images, and connected linearly with origin of insertion (green dot); this process was performed on a zoomed version of the images to enhance visibility. For additional information regarding these experiments, refer to Supplementary Video 5.

The results in Figure 4.10 show the ability of the fabricated catheter to autonomously shape to a convoluted anatomy. Three main distal ends of the left bronchi were successfully reached by manipulating the 3D field with the proposed actuation method on the optimally designed catheters. The autonomous shaping under the field applied by the dEPM is performed by design. In fact, shape-forming is completely defined by the design

magnetization and applied field, informed by the preoperative CT, as discussed in the Methods section. The case in Figure 4.10B shows that the catheter can achieve high levels of bending (almost 90°) and target hard-to-reach anatomical areas. This is achieved as a combination of high flexibility, small cross-section, high magnetic material concentration and strong applied field. The three scenarios analyzed herein describe diversity in the anatomy and successful navigation demonstrates that the proposed approach is applicable to a variety of anatomical conditions.

## 4.4 Discussions

The performed experiments show the advantages of using patient-specific magnetic catheters in endoscopy. We demonstrated improved shape-forming, obstacle avoidance and targeting, compared to tip- and axially-magnetized catheter designs. Specifically, we obtain 50% contact reduction and improved tracking, fundamental both for improving the navigation capabilities and reducing pain and discomfort for the patient. The reduced contact is also reflected in better tracking of the desired trajectory and targeting (90% improvement). In fact, in some cases, tip- and axially-magnetized catheters may follow the trajectory since forced by the anatomy and fail in mitigating contact. We also demonstrate how the proposed shape-forming catheters can navigate realistic anatomy, namely, a phantom of the bronchial tree derived from patient CT data. We selected three diverse anatomical features and show successful navigation of the catheter in open-loop in around 2 minutes, for all cases. The presented work is based on pre-operative planning and open-loop control. In real clinical scenarios, we may not guarantee feasible navigation, without tracking of the catheter and the anatomy on-line. Therefore, we will consider intraoperative imaging (e.g. fluoroscopy) and shape sensing of the catheters, to guarantee navigation via closed-loop control. In our experimental analysis in the bronchial tree, we employed a constrained dEPM platform to guarantee an EPM-EPM distance of 50 cm, which can fit an average patient. However, we do not exclude larger permanent magnets would be needed for clinical application, to account for any possible patient size. The optimized

catheters were designed with a planar magnetization and proven effective in the scenarios proposed. The discussed optimization and actuation can deal with non-planar magnetization, but the current fabrication method may fail in creating out-of-plane magnetic dipoles. We will develop a more appropriate fabrication method, which we expect to further improve navigation and reduce contact with the environment. The optimized catheters are inherently characterized by a non-axial magnetization, which we proved to facilitate navigation. However, this may also lead to undesired torsion, as seen in some experiments. This behavior is mainly due to the applied gradient-free actuation, which may cause instabilities. We will consider the usage of gradients, already discussed by Pittiglio et al., [24] to control the torsion of the designed catheters. In case the torsional behavior is undesired, we will also integrate optimization constraints and/or mechanical constraints, as discussed by Lloyd et al. [25]

## 4.5 Conclusions

In the presented work, we have introduced a novel design approach for patient-specific, magnetically driven, shape-forming soft catheters. The goal of the approach is to design and fabricate catheters to navigate the human body with minimal and atraumatic environmental interaction. Thus, facilitating enhanced navigation and targeting ability while reducing post-operative recovery time. The use of pre-operative imaging in the design paradigm ensures the catheter follows the anatomical pathway whilst subject to an omni-directional controlled magnetic field. We demonstrate that the proposed approach can perform less invasive navigation and more accurate targeting, compared to previously proposed magnetic catheterization techniques. Moreover, we describe and demonstrate the full process of pre-operative path planning, design optimization and navigation in bronchoscopy. We present the capabilities of the proposed catheters in an anatomically accurate 3D bronchi phantom by exploring three diverse branches. Experiments were performed in a static environment to demonstrate the accuracy of the proposed design technique. To achieve full autonomy, as demonstrated for colonoscopy in Martin et al

[26], and for further reduction of intraoperative imaging, future work will address closed loop control of both catheter location and shape.

In the present work, we modelled each magnetic element as a rigid link. This approximation is accurate for small relative deflection of the catheter. The model is mainly used for the optimal distribution of the magnetic Degrees of Freedom (DOFs). In conjunction with closed-loop control, we expect that this approximation will not negatively affect the navigation, even in case of large deflections.

Furthermore, future research will aim to control magnetic field gradients and thus, magnetic force, during navigation; target torsion reduction via both design/fabrication and control approaches; and integration with diagnostic or therapeutic instruments for (e.g., biopsy). These developments will be in concert with further miniaturization, automated fabrication and the addition of friction reduction strategies. Through the presented patient-specific magnetic catheter approach, we believe that atraumatic autonomous exploration of a wide range of anatomical features will be possible, with the potential to reduce trauma and improve diagnostic yield.

## Bibliography

- [1] Attanasio A, Scaglioni B, De Momi E, et al. Autonomy in Surgical Robotics. *Annual Review of Control, Robotics, and Autonomous Systems*. 2021;4(1):651–679.
- [2] Veiga T, Chandler J, Lloyd P, et al. Challenges of Continuum Robots in Clinical Context: A Review. *Progress in Biomedical Engineering*. 2020;2.
- [3] Berthet-Rayne P, Sadati SMH, Petrou G, et al. MAMMOBOT: A Miniature Steerable Soft Growing Robot for Early Breast Cancer Detection. *IEEE Robotics and Automation Letters*. 2021;6(3):5056–5063.
- [4] Li M, Obregon R, Heit JJ, et al. VINE Catheter for Endovascular Surgery. *IEEE Transactions on Medical Robotics and Bionics*. 2021;3(2):384–391.
- [5] Nguyen TD, Burgner-Kahrs J. A Tendon-Driven Continuum Robot with Extensible

Sections. In 2015 IEEE/RSJ International Conference on Intelligent Robots and Systems (IROS); Institute of Electrical and Electronics Engineers Inc., 2015; pp. 2130–2135.

[6] De Falco I, Cianchetti M, Menciassi A. A Soft Multi-Module Manipulator with Variable Stiffness for Minimally Invasive Surgery. *Bioinspiration & Biomimetics*. 2017;12(5):56008.

[7] Kang B, Kojcev R, Sinibaldi E. The First Interlaced Continuum Robot, Devised to Intrinsically Follow the Leader. *PLoS ONE*. 2016;11(2):e0150278.

[8] Edelmann J, Petruska AJ, Nelson BJ. Magnetic Control of Continuum Devices. *International Journal of Robotics Research*. 2017;36(1):68–85.

[9] Heunis C, Sikorski J, Misra S. Flexible Instruments for Endovascular Interventions: Improved Magnetic Steering, Actuation, and Image-Guided Surgical Instruments. *IEEE Robotics and Automation Magazine*. 2018;25(3):71–82.

[10] Norton JC, Slawinski PR, Lay HS, et al. Intelligent Magnetic Manipulation for Gastrointestinal Ultrasound. *Science Robotics*. 2019;4(31):1–14.

[11] Jeon S, Hoshiar AK, Kim K, et al. A Magnetically Controlled Soft Microrobot Steering a Guidewire in a Three-Dimensional Phantom Vascular Network. *Soft Robotics*. 2018;00(00):soro.2018.0019.

[12] Lloyd P, Hoshiar AK, Veiga T da, et al. A Learnt Approach for the Design of Magnetically Actuated Shape Forming Soft Tentacle Robots. *IEEE Robotics and Automation Letters*. 2020;5(3):3937–3944.

[13] Lum GZ, Ye Z, Dong X, et al. Shape-Programmable Magnetic Soft Matter. *Proceedings of the National Academy of Sciences*. 2016;113(41):E6007 LP-E6015.

[14] Lloyd P, Pittiglio G, Chandler JH, et al. Optimal Design of Soft Continuum Magnetic Robots under Follow-the-Leader Shape Forming Actuation. In 2020 International Symposium on Medical Robotics (ISMR); 2020; pp. 111–117.

[15] Jeon S, Hoshiar AK, Kim K, et al. A Magnetically Controlled Soft Microrobot Steering a Guidewire in a Three-Dimensional Phantom Vascular Network. *Soft Robotics*.

2018;00(00):soro.2018.0019.

[16] Lum GZ, Ye Z, Dong X, et al. Shape-Programmable Magnetic Soft Matter. *Proceedings of the National Academy of Sciences*. 2016;113(41):E6007 LP-E6015.

[17] Cicienia J, Avasarala SK, Gildea TR. Navigational Bronchoscopy: A Guide through History, Current Use, and Developing Technology. *Journal of thoracic disease*. 2020;12(6):3263–3271.

[18] Silvestri GA, Bevill BT, Huang J, et al. An Evaluation of Diagnostic Yield From Bronchoscopy: The Impact of Clinical/Radiographic Factors, Procedure Type, and Degree of Suspicion for Cancer. *Chest*. 2020;157(6):1656–1664.

[19] Pittiglio G, Chandler JH, Richter M, et al. Dual-Arm Control for Enhanced Magnetic Manipulation. In *2020 IEEE/RSJ International Conference on Intelligent Robots and Systems (IROS)*; 2020; pp. 7211–7218.

[20] Hoelscher J, Fu M, Fried I, et al. Backward Planning for a Multi-Stage Steerable Needle Lung Robot. *IEEE Robotics and Automation Letters*. 2021;6(2):3987–3994.

[21] Barducci L, Pittiglio G, Norton JC, et al. Adaptive Dynamic Control for Magnetically Actuated Medical Robots. *IEEE Robotics and Automation Letters*. 2019;4(4):3633–3640.

[22] Pittiglio G, Barducci L, Martin JW, et al. Magnetic Levitation for Soft-Thetered Capsule Colonoscopy Actuated With a Single Permanent Magnet: A Dynamic Control Approach. *IEEE Robotics and Automation Letters*. 2019;4(2):1224–1231.

[23] Heunis CM, Wotte YP, Sikorski J, et al. The ARMM System - Autonomous Steering of Magnetically-Actuated Catheters: Towards Endovascular Applications. *IEEE Robotics and Automation Letters*. 2020;5(2):705–712.

[24] Pittiglio G, Chandler JH, Richter M, et al. Dual-Arm Control for Enhanced Magnetic Manipulation. In *2020 IEEE/RSJ International Conference on Intelligent Robots and Systems (IROS)*; 2020; pp. 7211–7218.

[25] Lloyd P, Koszowska Z, di Lecce M, et al. Feasibility of Fiber Reinforcement Within Magnetically Actuated Soft Continuum Robots . *Frontiers in Robotics and AI* , 2021, 8,

214.

[26] Martin J, Martin J, Norton J, et al. Toward Autonomous Robotic Colonoscopy: Motion Strategies for Magnetic Capsule Navigation. In 2018 IEEE International Conference on Cyborg and Bionic Systems (CBS); 2018; pp. 240–244.



## Chapter 5

# Attitude Sensing within Strong Magnetic Field

**Chapter source:** G. Pittiglio, S. Calò and P. Valdastrì, "On the Observability and Observer Design on the Special Orthogonal Group Based on Partial Inertial Sensing," in IEEE Transactions on Automatic Control, vol. 66, no. 10, pp. 4998-5005, Oct. 2021, doi: 10.1109/TAC.2020.3047553.

## Abstract

The aim of the present work is to discuss the observability properties and observer design for the attitude of a rigid body, in conditions of partial inertial sensing. In particular, we introduce an observability analysis tool for the attitude dynamics when only accelerometer and gyroscope measurements are available, as in several robotics applications. In various scenarios, in fact, the measurement of the magnetic field via a magnetometer is unreliable, due to magnetic interferences. Herein, we first focus on a formal observability analysis, which reveals that the target dynamics is *weakly locally observable*, but not first-order observable. The lack of first-order observability prevents standard observers from achieving global convergence. Therefore, we discuss a more suitable approach for observer design to deal with this problem. The proposed approach is validated by providing numerical and experimental results. The former show that the proposed approach is able to achieve convergence (final error 0.004%). Experiments validate our inference about observability and show the improvements brought by the proposed approach concerning the error convergence (final error 0.15%).

## 5.1 Introduction

Over the last decades, a large amount of research has focused on the estimation of the attitude of a rigid body [14]. This is crucial in several applications such as human motion tracking [20], small aerial vehicles [1], underactuated robotic systems [16], magnetically actuated robots [19] etc. Inertial Measurement Units (IMUs), composed of an *accelerometer* and a *gyroscope*, are widely employed as a sensing solution to the problem. In addition to this setup a *magnetometer* is also frequently used and the overall system

has been shown to provide enough information for the design of convergent observers for estimating the attitude [14; 13].

The main drawback of this sensing approach is that the magnetometer is a very unreliable measurement to be used. In fact, for indoor scenarios [11], applications for which IMUs are close enough to electrical motors [1; 16] and problems that involve strong magnetic fields [19], the magnetometer output is unpredictable. On-the-other-hand, not using the magnetometer leads to singularities in the estimation of the rotation. Physically, the *rotation around the gravity direction* can not be estimated. This is due to the fact that, for any rotation around this axis, the inertial output does not change and estimators can not distinguish between different rotations. Our aim is to show that this is an *observability singularity condition* for *weakly locally observable* dynamics. This goal is achieved by performing a detailed observability analysis of the problem.

Previous methods have inferred that the problem of estimating the attitude is observable if the measurement from a magnetometer is provided [14]. In line with this statement we show that, provided of accelerometer and gyroscope only, the system is not *first-order observable*. This means that the state cannot be estimated given *only the measurement of the output for any input* [8]. As a consequence, standard well-known techniques relying on first-order approximations, *e.g.* the Extended Kalman Filter (EKF) [18], fail in the state estimation [2]. However, for intrinsically nonlinear systems, observability is a local property which also depends on the inputs [8].

Observability analysis on *matrix groups* has been a topic of research for several years [3; 5; 10]. However, all these works deal with outputs on *coset spaces*, while we are interested into outputs lying on *homogeneous spaces* [13]. More recently, the authors of [17] proposed an observability analysis tool for aerial vehicles formations based on bearing measurements. This technique is based on the Observability Rank Condition (ORC) [8] and deals with outputs on homogeneous spaces. Moreover, the application of this technique reveals that a more suitable approach for observer design exists, as we will discuss.

Therefore, inspired by [17], we prove the system's *weak local observability*. This means that there exist inputs for which the system is observable, thus the state can be estimated. The lack of first order observability leads standard methods, such as [14], to fail and force to a more suitable choice for the observer. Based on these observations, we aim to describe a novel approach in designing *asymptotically convergent observers* based only on the measurement of *acceleration* (accelerometer) and *angular velocity* (gyroscope). We assume these measurements to be available and, unlike the magnetometer data, free from artifacts. We show that the information gained from the accelerometer output and its derivatives of, at least, order 1 is enough for designing a stable observer. This information leads to *marginal stability* when observability singularities occur and *asymptotic stability* in the case of full observability. Moreover, we emphasize that the first order derivative of the accelerometer output can be analytically computed and there is no need for approximated differentiation, which would lead to noise enhancement.

Before discussing the main contribution of our work, we formulate the problem under analysis and introduce some preliminaries about *Riemannian Geometry* [7] in Section 5.2. The latter is fundamental for the *observability analysis* presented in Section 5.3 and is employed for the design of the proposed observer, as discussed in Section 5.4 and 5.5. The proposed technique is validated through numerical analysis provided in Section 5.6 and experimental results in Section 5.7. In both the cases, a comparison with a Nonlinear Complementary Filter (NCF) [14] and an EKF [18] is discussed. Section 5.8 reports our conclusion and future perspectives, in light of our results.

## 5.2 Preliminaries

For an in depth understanding of the paper's contents some key concepts of Riemannian geometry [7] need to be introduced and discussed. We will partially consider the introduction in [17] and underline the basics we are also interested into.

### 5.2.1 Problem Formulation

Consider the problem of estimating the *attitude* of a rigid body based on the measurements from an IMU [14]. We describe the attitude on the *special orthogonal group*<sup>1</sup>  $SO(3)$ , i.e. the rotation of the rigid body is embedded in  $R \in SO(3)$ , where

$$SO(3) = \{R \in \mathbb{R}^{3 \times 3} | R^T R = I, \det(R) = 1\},$$

with  $I \in \mathbb{R}^{3 \times 3}$  identity matrix. This group is associated with the *Lie algebra* composed of the *skew-symmetric matrices*

$$\mathfrak{so}(3) = \{S \in \mathbb{R}^{3 \times 3} | S^T = -S\}.$$

Detailed geometric definitions of  $SO(3)$  are discussed in Section 5.2.2. With the aim of formulating our problem, we define the operators  $(\cdot)_\times : \mathbb{R}^3 \rightarrow \mathfrak{so}(3)$  and  $(\cdot)^V : \mathfrak{so}(3) \rightarrow \mathbb{R}^3$ .

For any vector  $v = (v_1 \ v_2 \ v_3)^T \in \mathbb{R}^3$

$$v_\times = \begin{pmatrix} 0 & -v_3 & v_2 \\ v_3 & 0 & -v_1 \\ -v_2 & v_1 & 0 \end{pmatrix}, (v_\times)^V = v.$$

Since in many robotics applications the measurement from the magnetometer is unreliable, we consider to be provided with only *acceleration* (accelerometers) and *angular velocity* (gyroscopes).

The main aim is to estimate the rotation matrix from the *local* reference frame  $\{B\}$  to *global* frame  $\{G\}$

$$R = {}^G R_B : \{B\} \rightarrow \{G\}.$$

The overall system, is

$$\dot{R} = R(\omega + \delta)_\times \tag{5.1a}$$

---

<sup>1</sup>We will always refer to matrices with real entries, thus the reference is avoided for simplicity's sake.

$$\bar{y} = R^T(g + a + \sigma) \quad (5.1b)$$

where  $\omega$  is angular velocity in body frame,  $\omega + \delta$  the measured angular velocity (gyroscopes),  $g$  is the gravitational acceleration and  $a$  the linear acceleration in global frame;  $\bar{y}$  is the measurement provided by the accelerometer, and  $\sigma$  and  $\delta$  measurement noise in the global and local reference frames, respectively.

In the present work, we consider  $\delta$  and  $\sigma$  as a null mean Gaussian noise and that the gravitational acceleration ( $g$ ) dominates over linear accelerations ( $a$ ), as per common approach in literature [14]. Filtering linear acceleration, is a common approach when the aim is reconstructing the attitude of a rigid body. In this work, the accelerometer is only used to sense the direction of gravity and not for position tracking. This assumption is valid in condition of small accelerations, which generally applies to medical procedures.

Under these assumptions, our *nominal model for the attitude dynamics* is

$$\dot{R} = R\omega_{\times} \quad (5.2a)$$

$$y = R^T g. \quad (5.2b)$$

Other linear components of the acceleration ( $a$ ) and noises ( $\delta$ ,  $\sigma$ ) will be taken into account in the design of the EKF in Section 5.5, while the observability analysis (see Section 5.3) will consider the nominal dynamics in (5.2).

The aim of the present work is to find an asymptotically convergent estimate for  $R$ , referred to as  $\hat{R} = {}^G R_E : \{E\} \rightarrow \{G\}$ . Here  $\{E\}$  is referred to as the *estimator* reference frame.

## 5.2.2 Riemannian Geometry

We refer to a generic manifold as  $\mathcal{M}$ , when generality is needed, and  $x \in \mathcal{M}$  for any of its points.

**Tangent Spaces** We define the *tangent space* of a manifold  $\mathcal{M}$  at the point  $x$ , referred to as  $T_x\mathcal{M}$ , as the space spanned by the tangents of the curves passing through  $x$ . For the Euclidean space  $\mathbb{R}^3$  the tangent space is  $\mathbb{R}^3$  itself [9]. In the case of  $SO(3)$ , we assume  $R(t) : T \rightarrow SO(3)$  being a parametrised curve, with  $T \subset \mathbb{R}$ . Therefore,  $\dot{R}(t) \in T_R SO(3)$ . Moreover, it can be shown that the tangent space at  $R$  is given by

$$T_R SO(3) = \{Rv_\times : v \in \mathbb{R}^3\}.$$

Notice that we made use of this fact for the definition of the system in (5.2). Furthermore, note that  $T_I SO(3) \equiv \mathfrak{so}(3)$ , in line with the classical definition of  $\mathfrak{so}(3)$ .

**Metrics** We refer to Riemannian metric  $\langle \cdot, \cdot \rangle$  as the operator which assigns an inner product to a tangent space. In the case of  $\mathbb{R}^3$ , the standard *dot product* is associated. On  $SO(3)$ , we consider the metric

$$\langle Rv_\times, Rw_\times \rangle = \frac{1}{2} \text{tr}(v_\times^T w_\times) = v^T w, \quad (5.3)$$

for  $Rv_\times, Rw_\times \in T_R SO(3)$ ; here  $\text{tr}(\cdot)$  is the trace operator.

**Differentials** Consider a vector field  $\mu(x) \in T_x\mathcal{M}$  and a scalar function  $l(x)$ ,  $l : \mathcal{M} \rightarrow \mathbb{R}$ . We define the  $i$ -th order *Lie derivative* of  $l(x)$  with respect to  $\mu(x)$  as the scalar function

$$\mathcal{L}_{\mu(x)}^i l(x) = \langle \nabla_x \mathcal{L}_{\mu(x)}^{i-1} l(x), \mu(x) \rangle, \quad (5.4)$$

with  $\mathcal{L}_{\mu(x)}^0 l(x) = l(x)$ ; here  $\nabla_x$  is referred to as the gradient with respect to  $x$ . Moreover, for any parametrized curve  $x(t)$ ,  $t \in T \subset \mathbb{R}$ ,

$$\mathcal{L}_{\mu(x)}^i l(x) = \frac{d^i l(x)}{dt^i} = l^{(i)}(x). \quad (5.5)$$

Direct derivation is shown to be immediate, while defining the gradients on  $SO(3)$  is less straightforward, but fundamental for observability analysis purposes.

By following the steps of [17], we infer that for a general scalar function  $l(R)$ ,  $R \in SO(3)$

$$\frac{dl(R)}{dt} = \text{tr}(M^T \dot{R}) = \text{tr}(\text{skew}(R^T M)^T R^T \dot{R}) \quad (5.6)$$

for some matrix<sup>2</sup>  $M$ ;  $\text{skew}(A) = \frac{1}{2}(A - A^T)$ ,  $A \in \mathbb{R}^{3 \times 3}$ . By comparing (5.6) and (5.3), we deduce

$$\nabla_R l(R) = 2 (\text{skew}(R^T M)^V)^T. \quad (5.7)$$

According to the introduced metric on  $SO(3)$  (see (5.3)),

$$\frac{dl(R)}{dt} = 2 (\text{skew}(R^T M)^V)^T \dot{R}^V.$$

In [17], this solution is referred to as the *trace trick*.

**Covectors and codistributions** We interpret a (*smooth*) *covector field*  $\eta(x) \in (\mathbb{R}^m)^*$ , as a (smooth) assignment of an element of the manifold  $\mathcal{M}$  to an element of  $(\mathbb{R}^m)^*$ . We refer to  $(\mathbb{R}^m)^*$  as the dual of  $\mathbb{R}^m$  [9], when  $\mathcal{M}$  is a  $m$ -dimensional manifold.

Examples of covector fields, employed in the present work, are the differentials of any scalar function  $l(x) : \mathcal{M} \rightarrow \mathbb{R}$ , i.e.  $\nabla_x l(x) \in (\mathbb{R}^m)^*$ . In the case  $\mathcal{M} \equiv SO(3)$ ,  $\nabla_R l(R) \in (\mathbb{R}^3)^*$ .

A (smooth) codistribution is the span of covector fields, i.e., given the covector fields  $\eta_1(x), \eta_2(x), \dots, \eta_r(x)$ ,

$$\Lambda(x) = \text{span}(\eta_1(x), \eta_2(x), \dots, \eta_r(x))$$

is a codistribution. It can be also interpreted, in matrix form, as  $\Lambda(x) = (\eta_1^T(x) \eta_2^T(x) \cdots \eta_r^T(x))^T$ .

---

<sup>2</sup>More details about matrix  $M$  will be discussed in Section 5.3.

**Exponential Map of  $SO(3)$**  We define the exponential map as  $\exp : \mathfrak{so}(3) \rightarrow SO(3)$ .

For  $v_\times \in \mathfrak{so}(3)$  we define the exponential as<sup>3</sup>

$$\exp(v_\times) = \sum_{k=0}^n \frac{v_\times^k}{k!}.$$

We can also compute the differential of the exponential map with respect to  $v_\times$  as

$$\frac{\partial}{\partial v_\times} \exp(v_\times) = \sum_{k=0}^n \frac{v_\times^k}{(k+1)!}.$$

To avoid possible singularities for  $\|v\| = 0$  we will not use the Rodrigues formula but an approximation of the series, up to some order  $n$ .

### 5.3 Observability Analysis

The present section aims to derive the observability properties of the system in (5.2), based the results in Section 5.2.2. In the following, we employ the classical definition of observability, based on the ORC [8], as stated below.

**Definition 5.1.** *The system in (5.2) is weakly locally observable if the codistribution*

$$\nabla_R \mathcal{O} = \text{span}(\{\nabla_R \mathcal{L}_R^i y, i \in \mathbb{N}^+ \cup 0\})$$

*is full-rank.*

The definition of the observability codistribution undergoes to finding the gradients of the Lie derivatives of the outputs with respect to the tangent space. This is achieved, on  $SO(3)$ , by using the *trace trick* introduced in Section 5.2.2. We will describe how that tool applies to the case under analysis.

We consider system in (5.2) and introduce the angular velocity in  $\{G\}$  as  $\gamma = R\omega$ . The

---

<sup>3</sup>Note that this is valid for any matrix Lie group.

output derivatives for (5.2) can be computed recursively as

$$\begin{aligned} y_i^{(j)} &= e_i^T \left( \dot{R}^T \alpha_j + R^T \dot{\alpha}_j \right) g \quad j > 0, \\ \alpha_j &= -\gamma_{\times} \alpha_{j-1} + \dot{\alpha}_{j-1}, \end{aligned} \quad (5.8)$$

where  $e_i$  is the  $i$ -th element of the canonical basis of  $\mathbb{R}^3$  and selects the  $i$ -th row of  $y^{(j)}$  and  $\alpha_1 = I$ .

For the computation of the gradients, we use a general property of the scalar product, i.e. for any  $v, w \in \mathbb{R}^3$ ,  $L \in \mathbb{R}^{3 \times 3}$ ,

$$v^T L w = \text{tr}(v w^T L^T).$$

Therefore, (5.8) can be rewritten as

$$\begin{aligned} y_i^{(j)} &= \text{tr} \left( e_i g^T \alpha_j^T \dot{R} \right) + R^T \dot{\alpha}_j g \\ &= \langle \nabla_R \mathcal{L}_R^{j-1} y_i, \dot{R} \rangle + \langle \nabla_\gamma \mathcal{L}_\gamma^{j-1} y_i, \dot{\gamma} \rangle, \end{aligned} \quad (5.9)$$

according to Section 5.2.2.

From (5.9) and according to (5.6), we define

$$M_i^{<j>} = \alpha_j g e_i^T. \quad (5.10)$$

We can also define the generalized gradient with respect to  $R$  based on (5.6)

$$\nabla_R y_i^{(j-1)} = 2 \left( \text{skew}(R^T M_i^{<j>})^V \right)^T, \quad j > 0. \quad (5.11)$$

On the base of the defined gradients, we discuss the two main steps to prove the lack of first-order observability and the system weak local observability in Sections 5.3.1 and

5.3.2, respectively. For this purpose, we define

$$\begin{aligned}\nabla_R \mathcal{O}_{i+1} &= \left( \nabla_R \mathcal{L}_{\dot{R}}^i y_1^T \quad \nabla_R \mathcal{L}_{\dot{R}}^i y_2^T \quad \nabla_R \mathcal{L}_{\dot{R}}^i y_3^T \right)^T \\ &= \left( \nabla_R y_1^{(i)T} \quad \nabla_R y_2^{(i)T} \quad \nabla_R y_3^{(i)T} \right)^T\end{aligned}\quad (5.12)$$

and the  $i$ -th order observability codistribution

$$\nabla_R \mathcal{O}^i = \left( \nabla_R \mathcal{O}_1^T \quad \nabla_R \mathcal{O}_2^T \quad \cdots \quad \nabla_R \mathcal{O}_i^T \right)^T \quad i > 0. \quad (5.13)$$

In order to simplify the following dissertation, we will assume  $g = e_j$ ,  $j$ -th element of the canonical basis of  $\mathbb{R}^3$ , being free of defining  $\{G\}$ . Moreover, since  $\|g\|$  is a constant multiplicative scalar, it does not affect the rank of the observability distribution and the approach does not loose generality.

### 5.3.1 First-order Observability Analysis

The analysis of the first-order observability, based on previous definitions, is the analysis of rank  $\{\nabla_x \mathcal{O}^1\}$ . It undergoes to the computation of matrices  $M_i^{<1>}$ ,  $i = 1, 2, 3$ , defined in (5.10).

Since  $M_i^{<1>} = g e_i^T$ ,

$$R^T e_j e_i^T = \rho_j^T e_i^T = \begin{pmatrix} 0_{3,i-1} & \rho_j^T & 0_{3,3-i} \end{pmatrix} \quad (5.14)$$

where  $\rho_j$  is the  $j$ -th row of  $R$  and  $0_{l,k} \in \mathbb{R}^{l \times k}$  is referred to as the zero matrix. Eventually, we find

$$2\text{skew}(R^T e_j e_i^T) = \begin{pmatrix} 0_{3,i-1} & \rho_j^T & 0_{3,3-i} \end{pmatrix} - \begin{pmatrix} 0_{i-1,3} \\ \rho_j \\ 0_{3-i,3} \end{pmatrix}$$

and, from (5.7),

$$\nabla_R y_1 = (0 \quad -R_{j3} \quad R_{j2})$$

$$\nabla_R y_2 = (R_{j3} \quad 0 \quad -R_{j1})$$

$$\nabla_R y_3 = (-R_{j2} \quad R_{j1} \quad 0).$$

By stacking the gradients together, we obtain

$$\nabla_R \mathcal{O}_1 = \begin{pmatrix} 0 & -R_{j3} & R_{j2} \\ R_{j3} & 0 & -R_{j1} \\ -R_{j2} & R_{j1} & 0 \end{pmatrix}$$

which is skew-symmetric (its rank is 2), thus, only two *modes* of the attitude dynamics are first-order observable. Physically, we can conclude that the unobservable rotation is the one around  $g$ , as inferred in previous works [14].

### 5.3.2 Second-order Observability Analysis

In the following, we show that the computation of the second-order observability codistribution leads to conclude for the *weak local observability*. In this case, we aim to compute the matrices  $M_i^{<2>} = -\gamma_{\times} g e_i^T$ ,  $i = 1, 2, 3$ .

The direct computation of these matrices is long and involves several algebraic steps. Also, the generalization to any  $g$  is difficult to be described, therefore, we report the results for the case of  $g = -e_3$

$$\nabla_R \dot{y}_1 = (0 \quad \gamma_1 R_{23} - \gamma_2 R_{13} \quad \gamma_2 R_{12} - \gamma_1 R_{22}) \quad (5.15)$$

$$\nabla_R \dot{y}_2 = (\gamma_2 R_{13} - \gamma_1 R_{23} \quad 0 \quad \gamma_1 R_{21} - \gamma_2 R_{11})$$

$$\nabla_R \dot{y}_3 = (\gamma_1 R_{22} - \gamma_2 R_{12} \quad \gamma_2 R_{11} - \gamma_1 R_{21} \quad 0).$$

The codistribution  $\nabla_R \mathcal{O}_2 = (\nabla_R \dot{y}_1^T \quad \nabla_R \dot{y}_2^T \quad \nabla_R \dot{y}_3^T)^T$  is rank 2. However, the second-order codistribution  $\nabla_R \mathcal{O}^2 = (\nabla_R \mathcal{O}_1^T \quad \nabla_R \mathcal{O}_2^T)^T$  is rank 3. This proves the *weak local*

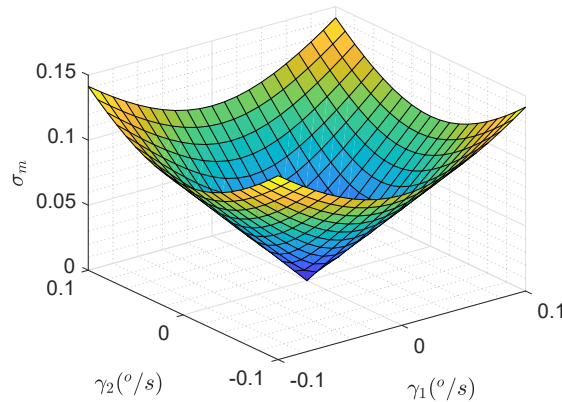


Figure 5.1: Analysis of the minimum singular value of  $\nabla_R \mathcal{O}^2 (\sigma_m)$ .

*observability.* By analysing (5.15), one can notice that it does not depend on  $\gamma_3$ , which is the rotation around  $g$  (for the specific case under analysis). This means that, for any rotation around  $g$ , the system observability does not change. Moreover, the only condition for which the system loses observability (*singularity condition*) is  $\gamma_1 = \gamma_2 = 0$ . This means that any rotation around any axis orthogonal to  $g$  makes the system observable. This is summarized by the analysis of the minimum singular value of  $\nabla_R \mathcal{O}^2$  in Fig. 5.1, which shows that the minimum singular value of the second-order observability codistribution is zero only when  $\gamma_1 = \gamma_2 = 0$ . Therefore, observability is lost only in case of either no rotation ( $\omega = 0$ ) or pure rotation around  $g$ . Without taking into account numerical precision related to observers implementation, in real environments pure rotation around an axis is very hard to occur. In the case no rotation occurs, only the rotations around axis orthogonal to  $g$  can be estimated. Therefore, in applying the proposed results, the IMU needs to be rotated to calibrate the initial error, at least once, before use.

### Example 5.1

A simple example of this inference is rotation around the gravity direction, assumed being  $e_j$  (observability singularity). This can be composed as  $\text{rot}_{e_j}(\theta) = \text{rot}_{e_i}(\phi)\text{rot}_{e_j}(\theta)\text{rot}_{e_i}(-\phi)$  for any  $i \neq j$ , and guarantees  $\gamma_k \neq 0$ , if  $\phi \neq 0$ , for some  $k \neq j$ . We refer to  $\text{rot}_{e_i}(\psi)$  as the rotation matrix around the axis  $e_i$  of an angle  $\psi$ .

## 5.4 Observer Design

The proof of weak local observability, provided in the previous section, supports the possibility of defining an asymptotically convergent observer. However, it also points out that first-order approximations [18] are not suitable, being the system not first order observable [2]. Moreover, the sole output does not provide enough information for state estimation, as discussed in [14].

Although, since the dynamics in (5.2) is second-order observable, the system

$$\dot{R} = R\omega_{\times} \quad (5.16a)$$

$$z = \begin{pmatrix} y \\ \dot{y} \end{pmatrix} = \begin{pmatrix} R^T g \\ -\omega_{\times} R^T g \end{pmatrix} \quad (5.16b)$$

is first order observable, as a direct consequence of the definition of observability codistribution in (5.12) and (5.13).

Therefore, we can design any first-order approximated observer for the extended system in (5.16), which considers all the information from the output and its derivative, without the need for approximated numerical differentiation. This avoids noise enhancement and reduces approximations.

### Example 5.2

Intuitively, the “virtual” measurement  $\dot{y} = -\omega_{\times} R^T g = -R^T \gamma_{\times} g$  captures the modes that are not measured with the sole  $y$ . In fact, assume  $g = -e_3$  again, if we aim to distinguish the initial configurations  $R_0 = \text{rot}_{e_3}(\theta)$  from  $R'_0 = I$ , we can rotate with angular velocity  $\gamma = (\dot{\phi} \ 0 \ 0)^T$ . We obtain the instantaneous measurement and its derivative as

$$\begin{cases} y &= -e_3 \\ \dot{y} &= -\text{rot}_{e_3}(-\theta)\dot{\phi}e_2 \end{cases}$$

Therefore, even if  $y$  does not capture the rotation around  $g$ ,  $\dot{y}$  does, as it is function of  $\text{rot}_{e_3}(-\theta)$ . This justifies the results of the observability analysis in Section 5.3 and

confirms the possibility of designing a first-order observer on the system in (5.16), as discussed in the next section.

## 5.5 Discrete EKF on $SO(3)$

Particularly effective in providing state estimation is the EKF [18], when systems are first order observable. In the following we present a discrete time version on  $SO(3)$  [17], which is employed in the following sections to enforce our conclusions on the system weak local observability.

We define the discrete dynamics of the estimated attitude  $\hat{R}$ , based on EKF, as

$$\hat{R}_{k+1} = \hat{R}_k \exp(\omega_{k \times} T) \exp((K_k \tilde{z}_k)_{\times}) \quad (5.17a)$$

$$\tilde{z}_k = z_k - h(\hat{R}_k, \omega_k), \quad (5.17b)$$

with  $k = 0, T, 2T, \dots$  and  $K_k$  gain, defined by the standard EKF *prediction* and *update* steps defined below. We intend with  $\exp(\cdot)$  the exponential map of  $SO(3)$ , introduced in Section 5.2.2 (we use order  $n = 10$  to approximate the series). Here  $h : SO(3) \times \mathbb{R}^3 \rightarrow \mathbb{R}^{3N}$ , where  $N = 1, 2$  represents whether we employ the output extension proposed in (5.16b) ( $N = 2$ ) or we apply the EKF to the sole accelerometer output, as in (5.2b) ( $N = 1$ ).

**Prediction** We consider the error  $\tilde{R} = \hat{R}^T R \sim \mathcal{N}(\mu_k, P_k)$ , with<sup>4</sup>  $\mu_k \in \mathbb{R}^3$  and  $P_k \in \mathbb{R}^{3 \times 3}$ , and the input noise  $\delta \sim (0_{3,1}, Q_n)$ ;  $Q_n \in \mathbb{R}^{3 \times 3}$ , constant matrix. The state covariance evolves as

$$P_k = F_k \bar{P}_{k-1} F_k^T + G_k Q_n G_k^T,$$

with  $F_k = \exp(\omega_{k \times} T)$  and  $G_k = R_k \frac{\partial}{\partial \omega_{k \times}} \exp(\omega_{k \times} T)$ . The computation of the exponential map and its differential is defined in Section 5.2.2.

---

<sup>4</sup>Note that  $SO(3)$  is a 3-dimensional manifold.

**Update** Consider the output noise  $\sigma = \mathcal{N}(0_{m,1}, R_n)$ , with  $R_n \in \mathbb{R}^{m \times m}$ , constant matrix, for  $z \in \mathbb{R}^m$ . The update aims at computing the observer's gain, by following the steps

$$\begin{aligned} S_k &= H_k P_k H_k^T + R_n \\ K_k &= P_k H_k^T S_k^{-1} \\ \bar{P}_k &= P_k - K_k S_k K_k^T. \end{aligned}$$

Fundamental to our discussion is matrix  $H_k = \frac{\partial z_k}{\partial R_k}$ . In fact [17],

$$\begin{cases} H_k = \nabla_R \mathcal{O}^1|_{R=R_k} & \text{if } z = y \\ H_k = \nabla_R \mathcal{O}^2|_{R=R_k} & \text{if } z = (y^T \dot{y}^T)^T \end{cases}$$

Therefore, we propose to apply a standard EKF to an extended dynamics, which considers also the output derivatives. This guarantees state estimation, as long as the system does not evolve on an observability-singular submanifold of  $SO(3)$ . In fact, only if  $H_k$  is full-rank the gain of the EKF would act on all the modes of the system [2].

We experimentally observed more stability in the proposed method by adding a further output derivative, i.e.  $z = (y^T \dot{y}^T \ddot{y}^T)^T$ . This is probably due to an increase of amount of information over the noise. On-the-other-hand, the second order derivatives, according to (5.8), reads as

$$\ddot{y} = R^T \gamma_{\times}^2 g + R^T \dot{\gamma}_{\times} g,$$

so only the left-most term can be analytically computed. We will consider the right-most one being part of the output noise parametrization, considering it in matrix  $R_n$ .

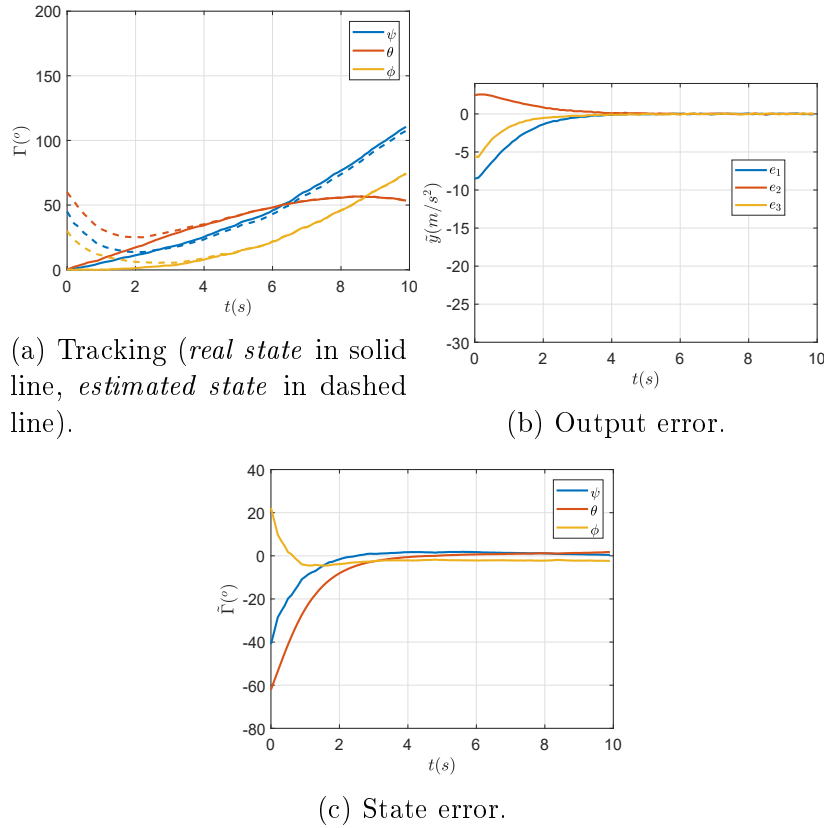


Figure 5.2: Proposed method numerical results.

Therefore, we propose a *first order* EKF as in (5.17), with

$$z_k = \begin{pmatrix} R_k^T g \\ -\omega_{k \times} R_k^T g \\ \omega_{k \times}^2 R_k^T g \end{pmatrix}.$$

## 5.6 Numerical Results

In the following we report the results obtained by applying the proposed approach to observer design. This technique is compared with a standard EKF and a NCF [14], applied to the dynamics in (5.1). Both the EKFs were implemented as discussed in previous section. As a difference, the proposed technique employs the output and its derivatives up to second order.

We consider  $g = -9.81 e_3 \text{ m/s}^2$ . Concerning the initial error  $\tilde{R}_0 = \text{rot}_{e_3}(45)\text{rot}_{e_2}(60)\text{rot}_{e_1}(30)$ . The proposed EKF and standard EKF parameters are reported in Table 5.1. The gain

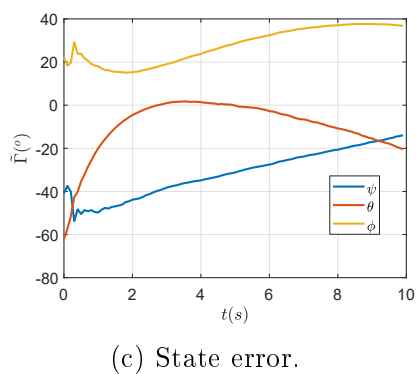
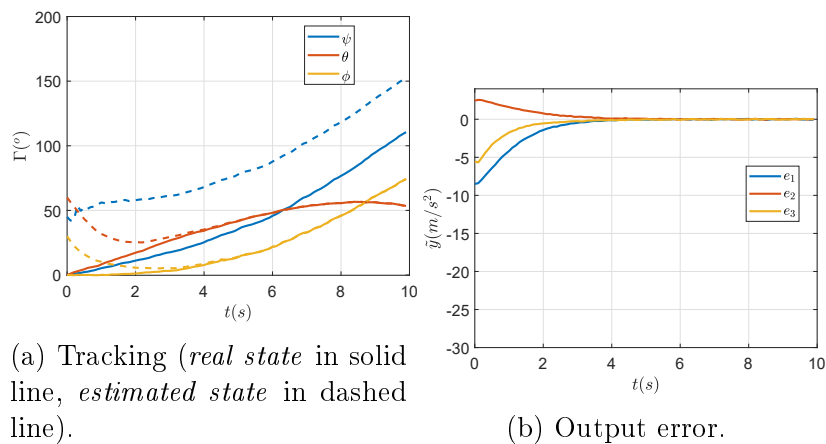


Figure 5.3: EKF numerical results [18].

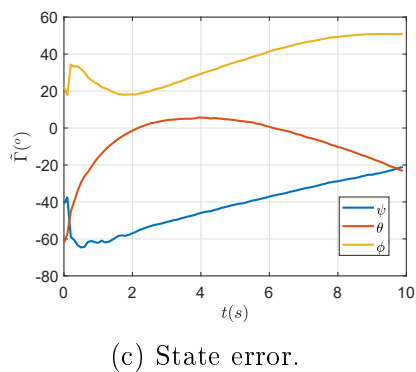
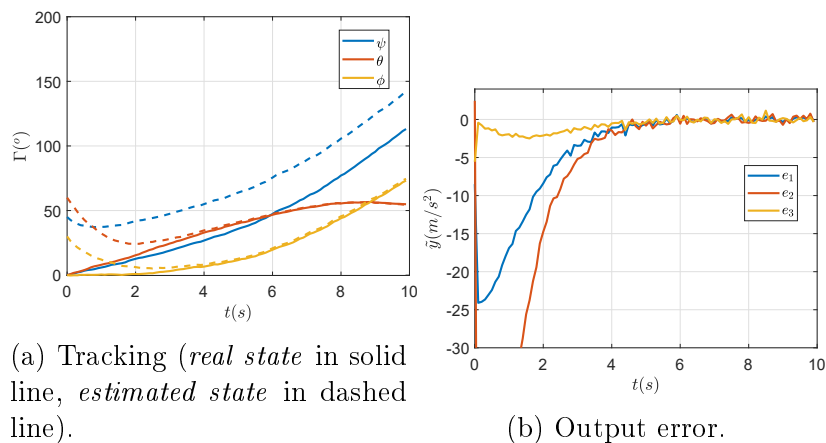


Figure 5.4: NCF numerical results [14].

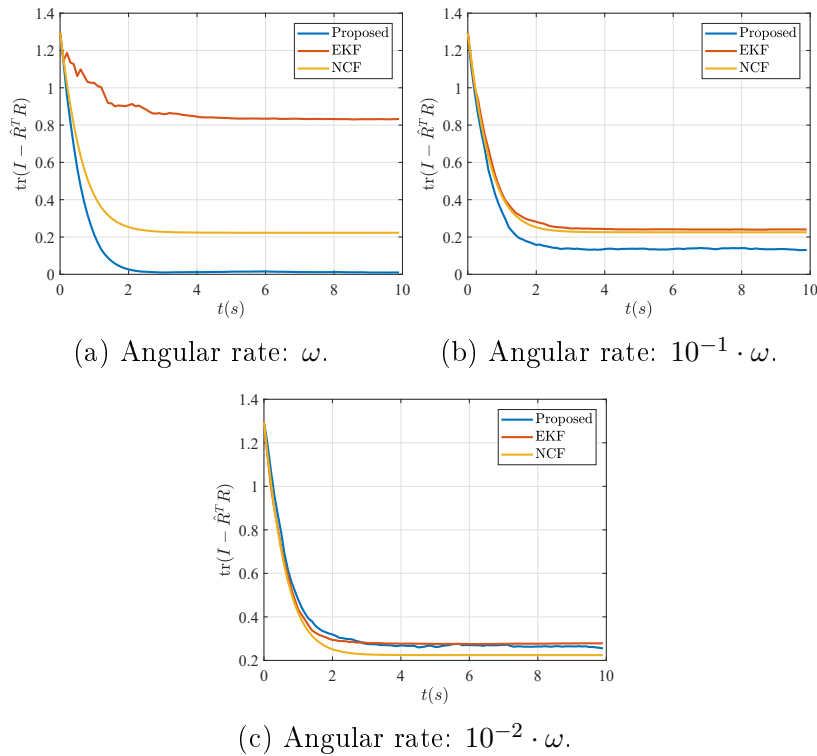


Figure 5.5: Error comparison over different input velocities.

Table 5.1: EKFs covariance matrices (simulations).

	EKF	Proposed
<b>State</b>	$P_0 = 10^{-4}I$	$P_0 = 10^{-4}I$
<b>Input</b>	$Q_n = 10^{-5}I$	$Q_n = 10^{-5}I$
<b>State</b>	$R_n = 10^{-5}I$	$R_n = \text{diag}(10^{-5}I, 10^{-7}I, 10^{-9}I)$

of the NCF was set to  $k = 10^{-1}$ , to achieve a convergence speed comparable to the other strategies.

We considered the input  $\omega = (0.09 \ 8.58 \ 6.01)^T$   $^\circ/s$ , being one of the choices for which we obtain a satisfactory observability index. Results are reported in Fig. 5.2, 5.3 and 5.4. Therein,  $\Gamma = \text{eul}(R)$  and  $\tilde{\Gamma} = \text{eul}(\tilde{R})$ , where  $\text{eul}(\cdot) : SO(3) \rightarrow \mathbb{R}^3$  maps the rotation to *Euler angles ZYX*. As underlined by the results, even if the output converges for all the applied methods (Fig. 5.2b, 5.3b and 5.4b), the only one capable of estimating the attitude is the proposed approach, as shown in Fig. 5.2c.

In Fig. 5.5 we employ  $\text{tr}(I - \hat{R}^T R) = \text{tr}(I - \tilde{R})$  as an error metric [17], by analyzing the results for different angular velocities, and underlining that only for slow movements

Table 5.2: EKFs covariance matrices (experiments).

	EKF	Proposed
<b>State</b>	$P_0 = 10^{-4}I$	$P_0 = 10^{-4}I$
<b>Input</b>	$Q_n = 1.7 \cdot 10^{-4}I$	$Q_n = 1.7 \cdot 10^{-4}I$
<b>State</b>	$R_n = 2 \cdot 10^{-3}I$	$R_n = \text{diag}(2 \cdot 10^{-3}I, 3.4 \cdot 10^{-7}I, 5.7 \cdot 10^{-11}I)$

the results of the proposed method are comparable to the ones of previously proposed approaches.

The numerical results underline that the proposed approach attains a final error of 0.004%, against the 45.5% of the EKF and 17.3% of the NCF, in the case of full observability.

## 5.7 Experimental Analysis

For experimental testing, we considered the data<sup>5</sup> related to the *EuRoC micro aerial vehicle* [4]. We used only IMU data (accelerometer and gyroscope) and compared the results with the provided ground-truth measurement from a *Leica Nova MS50 laser tracker*<sup>6</sup>. In this case  $g = (0.32 \ 0.07 \ 9.85)^T \text{ m/s}^2$  and the initial error is  $\tilde{R}_0 = \text{rot}_{e_3}(15)\text{rot}_{e_2}(-60)\text{rot}_{e_1}(-45)$ . The global gravity has been extracted from experimental data, by performing a calibration procedure: from the accelerometer and ground-truth measurement an identification of the gravity direction was performed. The misalignment between  $g$  and  $e_3$  may be due to sensor noise or small estimation errors. We also calibrated the gyroscope data using ground truth measurements, in order to remove possible bias.

The EKFs parameters, reported in Table 5.2, were obtained from the sensors information provided in the documentation of the dataset [4]. The gain of the NCF was set to  $k = 10^{-2}$ , to achieve similar convergence rate.

<sup>5</sup>Data is available at the link: <https://projects.asl.ethz.ch/datasets/doku.php?id=kmavvisualinertialdatasets>.

<sup>6</sup><https://leica-geosystems.com/en-GB/products/total-stations/multistation/leica-nova-ms60>

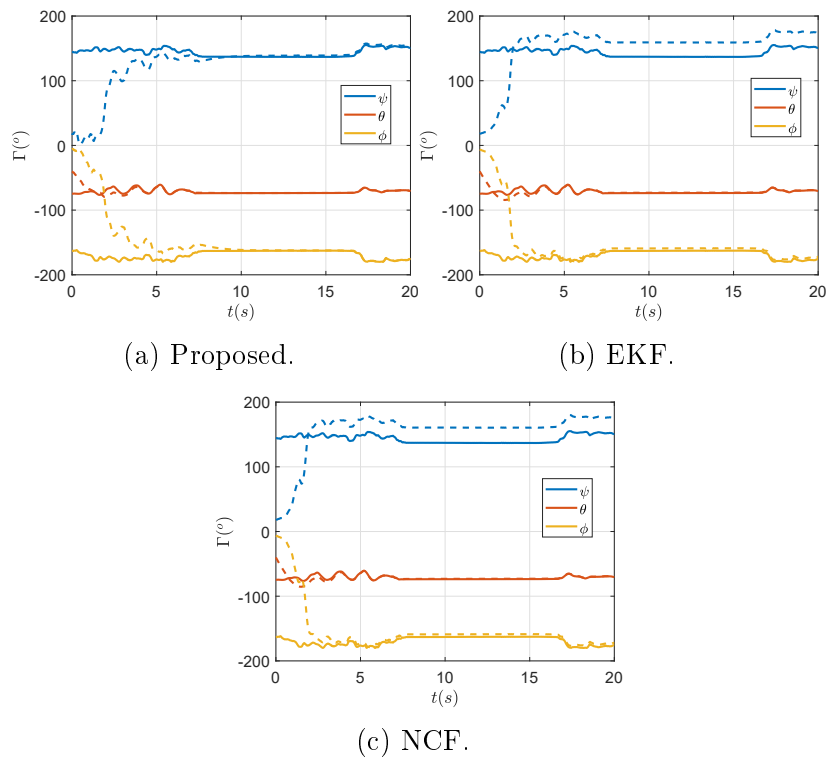


Figure 5.6: Experimental tracking comparison (*real state* in solid line, *estimated state* in dashed line).

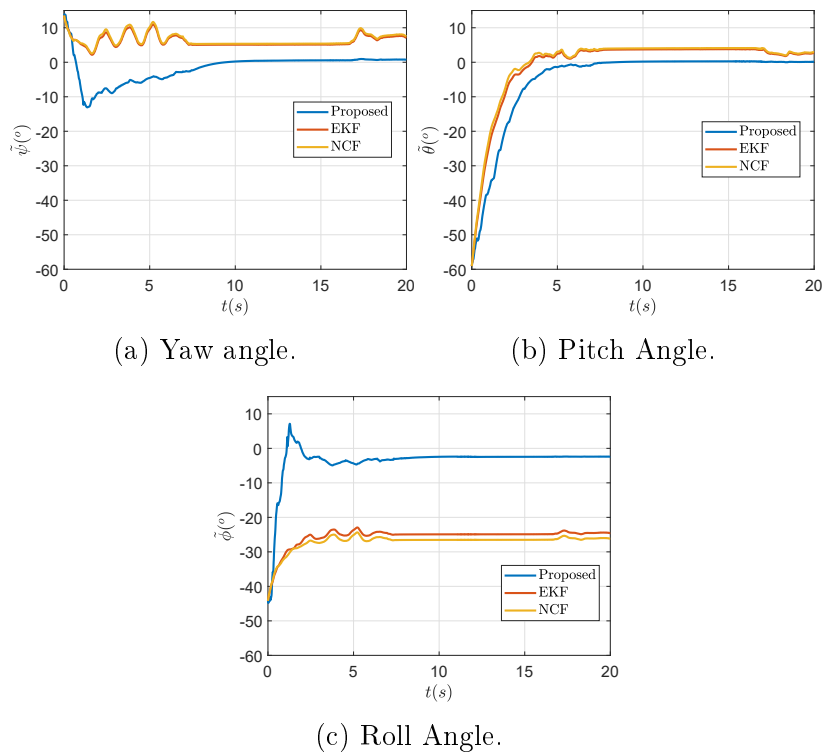
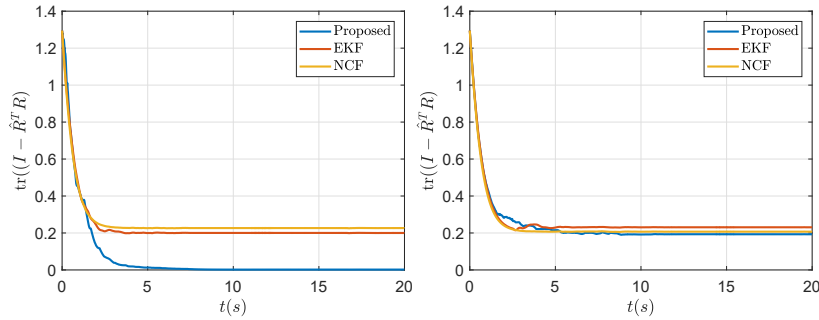
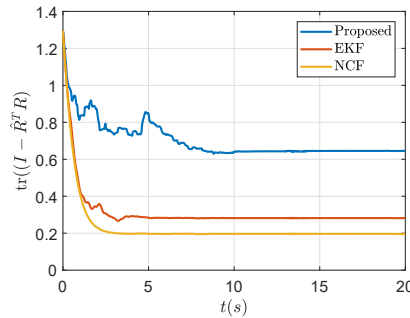


Figure 5.7: Experimental error comparison.



(a) Average Angular Rate:  $\bar{\omega} = 16.6$   $^{\circ}/s$  (Machine Hall 3). (b) Average Angular Rate:  $\bar{\omega} = 12.0$   $^{\circ}/s$  (Machine Hall 5).



(c) Average Angular Rate:  $\bar{\omega} = 13.7$   $^{\circ}/s$  (Machine Hall 4).

Figure 5.8: Experimental error comparison over different input velocities.

Fig. 5.6 and 5.7 report the tracking performance of the three techniques when dealing with a “fast movement” (EuRoC Machine Hall 3 dataset): average angular rate  $\bar{\omega} = 16.6$   $^{\circ}/s$ . We detail the respective tracking of the three Euler angles and the error. It is observed that the proposed technique leads to a significant reduction of the estimation error, compared to the other techniques, as also underlined by Fig. 5.8a. In particular we attain a final error of 0.15%, against 15.44% for the EKF and 17.49% for the NCF.

In Fig. 5.8, we report the results obtained for different velocities and underline the effect of the angular rate on the observability properties of the target dynamics and, therefore, on the performance of the methods. This is particularly evident for the proposed one, whose performance is comparable to the other strategies for lower rotation rates, as expected from the simulation. This is due to the physical properties of the system, as there is no way of avoiding observability singularities to cause deterioration of the observer convergence. Nonetheless, there exist control approaches (e.g. [6]) which attain optimal observability for weakly observable dynamics.

Fig. 5.8c also underlines that, in real-world scenarios, performance does not only depend on the observability (or angular rate). This may be due to the restrictive assumptions in applying the EKF. Possible solutions are the Unscented Kalman Filter (UKF) [12] and Particle Filters [15].

## 5.8 Conclusions

The present work dealt with the analysis of the observability and observer design for attitude estimation on the Special Orthogonal Group  $SO(3)$ , based on partial inertial sensing. In particular, we proved that we can obtain an asymptotic estimate of the attitude with the sole measurement of accelerometer and gyroscope.

We, first, show that the dynamics is *weakly locally observable*, then, reveal that, by using the output derivatives, convergences can be attained in the case of full-observability.

The proposed strategy was validated through numerical and experimental analysis and compared with an EKF which considers no derivatives and a NCF. Both the studies underline that the use of output derivatives enhances error convergence, in case of full observability, and that comparable results are obtained when close to observability singularities.

In the present work, possible bias on the gyroscope was assumed negligible and removed from experimental data by calibration. Future investigation will target scenarios when this calibration is not possible and bias can not be neglected.

## Bibliography

- [1] Baerveldt, A. J. and Klang, R. [1997]. A low-cost and low-weight attitude estimation system for an autonomous helicopter, *Proceedings of IEEE International Conference on Intelligent Engineering Systems*, pp. 391–395.
- [2] Bicchi, A., Prattichizzo, D., Marigo, A. and Balestrino, A. [1998]. On the observ-

- ability of mobile vehicles localization, *Proc. IEEE Mediterranean Conf. On Control And Systems*.
- [3] Brockett, R. [1972]. System theory on group manifolds and coset spaces, *SIAM Journal on Control* **10**(2): 265–284.  
**URL:** <https://doi.org/10.1137/0310021>
- [4] Burri, M., Nikolic, J., Gohl, P., Schneider, T., Rehder, J., Omari, S., Achtelik, M. W. and Siegwart, R. [2016]. The euroc micro aerial vehicle datasets, *The International Journal of Robotics Research* **35**(10): 1157–1163.  
**URL:** <https://doi.org/10.1177/0278364915620033>
- [5] Cheng, D., Dayawansa, W. and Martin, C. [1990]. Observability of systems on lie groups and coset spaces, *SIAM Journal on Control and Optimization* **28**(3): 570–581.  
**URL:** <https://doi.org/10.1137/0328034>
- [6] Cognetti, M., Salaris, P. and Giordano, P. R. [2018]. Optimal active sensing with process and measurement noise, *2018 IEEE International Conference on Robotics and Automation (ICRA)*, pp. 2118–2125.
- [7] do Carmo, M. [1992]. *Riemannian Geometry*, Mathematics (Boston, Mass.), Birkhäuser.  
**URL:** <https://books.google.co.uk/books?id=uXJQQgAACAAJ>
- [8] Hermann, R. and Krener, A. [1977]. Nonlinear controllability and observability, *IEEE Transactions on Automatic Control* **22**(5): 728–740.
- [9] Isidori, A. [1995]. *Nonlinear Control Systems*, 3rd edn, Springer-Verlag, Berlin, Heidelberg.
- [10] Jouan, P. [2009]. On the Existence of Observable Linear Systems on the Lie Groups, *Journal of Dynamical and Control Systems* **15**(3): 307–330.  
**URL:** <http://link.springer.com/article/10.1007/s10883-009-9071-2>

- [11] Joukov, V., Česić, J., Westermann, K., Marković, I., Kulić, D. and Petrović, I. [2017]. Human motion estimation on Lie groups using IMU measurements, *2017 IEEE/RSJ International Conference on Intelligent Robots and Systems (IROS)*, pp. 1965–1972.
- [12] Julier, S., Uhlmann, J. and Durrant-Whyte, H. F. [2000]. A new method for the nonlinear transformation of means and covariances in filters and estimators, *IEEE Transactions on Automatic Control* **45**(3): 477–482.
- [13] Khosravian, A., Trumpf, J., Mahony, R. and Lageman, C. [2013]. Bias estimation for invariant systems on Lie groups with homogeneous outputs, *Proceedings of the IEEE Conference on Decision and Control* pp. 4454–4460.
- [14] Mahony, R., Hamel, T. and Pfimlin, J.-M. [2008]. Nonlinear Complementary Filters on the Special Orthogonal Group, *IEEE Transactions on Automatic Control* **53**(5): 1203–1218.
- [15] Moral, P. D. [1996]. Nonlinear filtering: Interacting particle solution, *Markov Processes and Related Fields* **2**(4): 555–580.
- [16] Santaera, G., Luberto, E., Serio, A., Gabbicini, M. and Bicchi, A. [2015]. Low-cost, fast and accurate reconstruction of robotic and human postures via IMU measurements, *2015 IEEE International Conference on Robotics and Automation (ICRA)*, pp. 2728–2735.
- [17] Schiano, F. and Tron, R. [2018]. The Dynamic Bearing Observability Matrix Non-linear Observability and Estimation for Multi-Agent Systems, *ICRA 2018 - IEEE International Conference on Robotics and Automation*, Brisbane, Australia, pp. 1–8.  
**URL:** <https://hal.inria.fr/hal-01721774>
- [18] Sorenson, H. W. and Stubberud, A. R. [1968]. Non-linear filtering by approximation of the a posteriori density, *International Journal of Control* **8**(1): 33–51.  
**URL:** <https://doi.org/10.1080/00207176808905650>
- [19] Taddese, A. Z., Slawinski, P. R., Pirotta, M., De Momi, E., Obstein, K. L. and Valdastri, P. [2018]. Enhanced real-time pose estimation for closed-loop robotic ma-

nipulation of magnetically actuated capsule endoscopes, *The International Journal of Robotics Research* **37**(8): 890–911.

**URL:** <https://doi.org/10.1177/0278364918779132>

- [20] Zhang, Y., Song, K., Yi, J., Huang, P., Duan, Z. and Zhao, Q. [2018]. Absolute attitude estimation of rigid body on moving platform using only two gyroscopes and relative measurements, *IEEE/ASME Transactions on Mechatronics* **23**(3): 1350–1361.

# Chapter 6

## Conclusions

In the present thesis, the design, fabrication and control of novel magnetic endoluminal devices for minimally invasive diagnosis and treatment was presented. These devices have proven effective in improving the current practice in endoscopy and catheterization and have the potential of supporting the next generation in endoluminal procedures.

First, the control of a single-Internal Permanent Magnet (IPM) endoscope is discussed and a tip levitation technique, capable of controlling all its Degrees of Freedom (DOFs), introduced. The challenging problem of robustly controlling the endoscope to counteract gravitational forces was analysed. It was demonstrated that a dynamic control approach, applied to single robotically manipulated External Permanent Magnet (EPM), is able to accurately compensate for gravity. This control approach has proven effective in improving the navigation of the endoscope in colonoscopy procedures, by facilitating obstacle avoidance and mitigating continuous interaction with the anatomy.

To demonstrate the proposed controller can be applied to the medical practice, in vivo animal studies or cadaveric trials would be necessary. The former, would further prove that unexpected patient motion can be counteracted. For clinical safety, it is likely that faster localization would be necessary. In fact, a more responsive localization can better predict unknown disturbance and further improve the stability of the control loop.

A different approach to endoluminal navigation was then introduced: magnetic tentacles. In this case, a novel design of magnetic devices, with the aim of full-shape control, was discussed. Magnetic tentacles are Soft Continuum Robots (SCRs) which embed multiple magnetic elements along their length. These elements, owing their appropriate design and actuation, can be independently controlled to improve navigation in convoluted anatomical structures. However, the usage of a single robotically-manipulated EPM as main source of actuation limits the DOFs that can be controlled. For this reason, a novel actuation method which employs two EPMS was designed: the dual External Permanent Magnet (dEPM) platform.

In Chapter 3, the principles of collaborative magnetic actuation unique of the dEPM platform were presented and up to 8 independent DOFs were manipulated with this

approach; i.e. 3 more DOFs compared to single-EPM. The two EPMS were mounted at the end-effectors of two serial manipulators and synchronously actuated to generate independent fields and field gradients. The former are known to generate independent torques, the latter independent forces.

The problem of actuating 2 IPMS in close proximity was first considered, by assuming they are in the same point in the magnetic workspace. This assumption is not limiting, on the contrary, it actually represents the worst case scenario. In theory, up to 10 DOFs can be manipulated when the IPMS are far enough from each other, however, their independence depends on their separation. We cannot guarantee enough distancing between magnetic agents and handling the worst case scenario can be beneficial for the more general case. When operating on non-parallel IPMS, it was showed that 8 independent DOFs can be actuated.

The dEPM approach not only introduces more DOFs, compared to standard single-IPM actuation, but also generates higher forces and torques owing the usage of 2 EPMS. This is particularly beneficial when deeper in the anatomy and when the small scale of the endoluminal devices does not allow for large IPMS to be embedded in the endoscopes or catheters. In combination with high field density of permanent magnets, when compared to systems of coils, this actuation method has strong potential in its application to the clinical context.

The dEPM platform represents great possibility as an innovative platform for dexterous magnetic manipulation. However, its limitations are unintuitive joint to field map and low frequency control. The former problem results from the fact planning the motion in joint space leads to the generation of unexpected fields during transitions. To solve this issue, one should consider a more effective planner which can generate smooth field change. For high frequency manipulation, a possible approach is using a rotating permanent magnet at the end effector of the robots [2].

The initial work on multi-IPMS/multi-EPMS actuation, reported in Chapter 3, has lead to considering its application to the clinical practice. Specifically, it was noticed that

the magnetization profile (i.e. magnetic dipole direction along the continuum device) has a strong impact on the distribution of the magneto-mechanical DOFs. Therefore, optimization of the navigation capabilities of magnetic tentacles was investigated; this was achieved by designing their magnetic profile in a patient-specific pattern.

In Chapter 4 tip-, axially- and optimally-magnetized soft catheters were compared; the first ones are axially magnetized at their tip, the second type are catheters which are axially magnetized along their whole length. The optimal catheters were magnetized so that, with prior knowledge of the desired pathway, they would shape in a follow-the-leader manner. In Chapter 4 it was demonstrated that the optimal design guarantees improved navigation, obstacle avoidance and targeting.

When the size of the anatomy does not allow for intraluminal navigation technology, such as cameras, pre- and intra-operative imaging is often used. This is the case of e.g. bronchoscopy where pre-bent tools are manually navigated in the bronchi by using pre-operative Computed Tomography (CT) and intra-operative X-rays. Owing the lack of specific design of the rigid catheters, navigating to specific targets can be difficult and may stretch the anatomy. The latter issue may lead to failure of the pre-operative planning and pain to the patient. In this case, surgeons rely into intra-operative scanning which increases the radiation exposure of patients and healthcare providers.

In this context, the presented soft patient-specific magnetic tentacles were shown to autonomously navigate diverse anatomical structures based exclusively on CT-based pre-planning. An experimental analysis is presented in Chapter 4, performed on a phantom of the left bronchi, 3D printed from a CT scan. The 3D segmentation of the bronchi was used as information for planning the desired trajectories and design of the catheters' magnetization profile. The diameter of the fabricated catheters (2 mm) is smaller than current manual catheters (2.7 mm Medtronic superDimension) and robotic platforms (4.2 mm Auris MONARCH and 3.5 mm Intuitive Surgical Ion). The experiments were performed by actuating the magnetic tentacles with the dEPM platform discussed in Chapter 3.

The limitation of the proposed optimization technique is that it does not consider interaction with the anatomy. In a real case scenario, the interaction with the surroundings can have significant influence on navigation. To guarantee exploration in a real case scenario, closed-loop control is fundamental.

In Chapter 5, findings on the observability of sensors within strong magnetic fields are reported. The work focuses on attitude estimation with inertial sensing when the magnetometer reading is saturated by high magnetic fields. The results have a wide range of applications to the context of localization of small devices, fundamental in the case of intracorporeal magnetic actuation, where sight is lost. These results are employed in the clinical context for localization of our bronchoscopy platform; guiding actuation and navigation.

## Future Work

The present thesis has introduced various technical innovations in the context of magnetically actuated endoluminal diagnosis and treatment. The focus has been on providing solutions to the main technological challenges, which represent a gap between small-scale magnetic devices and clinical practice: design, fabrication, actuation, localization and control.

The research presented correlates to the main aim of addressing the most important problem in endoluminal procedures: navigation. The ability to reach deep anatomical structures, in a minimally invasive fashion, is a very complex problem whose challenges can be mitigated via robotics. The reported studies, concerning magnetic catheters, discussed their locomotion but their diagnostic and interventional capabilities are still being investigated.

The work here discussed has a wide range of applications and could be introduced in several surgical procedures. Both single- and multi-tentacle actuation will be further investigated; the former consists of one tentacle, as presented in Chapter 4, the latter can be used for various interventions which need multiple tools. Specifically, by mechanical

and magnetic design, two independent tools could be manipulated in the same workspace, by using the dEPM platform (see Chapter 3). This has a wide range of applications, such as e.g. ENT and abdominal surgery. The usage of soft tools can be beneficial for improved shaping, compared to standard rigid tools and can cause less post-operative pain.

The single-tentacle design and control paradigm has application to several endoscopic and catheterization procedures: intravascular catheterization, ENT, gastroscopy, colonoscopy, etc. These will be explored together with the integration of specific tools which can perform medical diagnosis and/or treatment.

The main focus is currently targeting lung cancer, which is one of the most deadly forms of cancer. In the most cases, diagnosis is performed via biopsy, and treatment comprises either surgery and therapy or directly therapy (radiotherapy and/or chemotherapy). To mitigate the invasiveness of current treatment approaches, locally targeted laser therapy [1] is currently being investigated. Specifically, patient-specific catheters, presented in Chapter 4, are designed to deliver a high-energy laser. In combination with *plasmonic gold nanoparticles*, treated to specifically bond to tumors, the platform will be able to selectively target cancerous tissue. Therefore, any anomaly visualised from pre-operative image analyses can be treated directly, without the risk of damaging healthy tissue.

This novel approach could reduce the usage of radio- and chemo-therapy, which are highly invasive for the patient. In the current stage, the delivery of this therapeutic technology can be used for tumors directly on the bronchial tree. The development of a tissue penetrating device, can generalise this approach to a wider range of tumors also deep in the lungs. In this case, analysis of the interaction between the tentacle and a real anatomy will be required.

For this reason, the performance of the magnetic tentacles in a cadaveric and, eventually, an animal model is to be investigated. These experiments will bring the proposed technology closer to clinical application.

In case of real clinical applications, sensing and closed loop control is fundamental. As discussed in Chapter 2, it is of primary importance to have highly accurate sensing to cope

unpredicted interaction with the anatomy. For this reason, closed-loop control methods, based on the results in Chapter 2, generalized to multi-IPMs SCRs, will be studied. This can guarantee more accurate targeting and, eventually, autonomous navigation [3].

The combination of accurate robust closed-loop control (Chapter 2), multi-DOF actuation (Chapter 3), optimal design (Chapter 4) and localization (Chapter 5) can facilitate a fully autonomous bronchoscopy platform. This work, combined with adjoining research into therapeutic laser delivery, may hopefully revolutionize treatment of lung and other types of cancer, and reduce the burden on affected patients.

## Bibliography

- [1] Knights, O. B., Cowell, D. M., Carpenter, T. M., Freear, S. and McLaughlan, J. R. [2018]. Plasmonic gold nanoparticles for combined photoacoustic imaging and plasmonic photothermal therapy using a pulsed laser, *2018 IEEE International Ultrasonics Symposium (IUS)*, pp. 1–4.
- [2] Mahoney, A. W. and Abbott, J. J. [2014]. Generating rotating magnetic fields with a single permanent magnet for propulsion of untethered magnetic devices in a lumen, *IEEE Transactions on Robotics* **30**(2): 411–420.
- [3] Martin, J. W., Scaglioni, B., Norton, J. C., Subramanian, V., Arezzo, A., Obstein, K. L. and Valdastri, P. [2020]. Enabling the future of colonoscopy with intelligent and autonomous magnetic manipulation, *Nature Machine Intelligence* **2**(10): 595–606.  
**URL:** <https://doi.org/10.1038/s42256-020-00231-9>